

COHERENT ANTI-STOKES RAMAN SCATTERING (CARS) OPTIMIZED
BY EXPLOITING OPTICAL INTERFERENCE

A Dissertation

by

XI WANG

Submitted to the Office of Graduate Studies of
Texas A&M University
in partial fulfillment of the requirements for the degree of

DOCTOR OF PHILOSOPHY

May 2011

Major Subject: Physics

COHERENT ANTI-STOKES RAMAN SCATTERING (CARS) OPTIMIZED
BY EXPLOITING OPTICAL INTERFERENCE

A Dissertation

by

XI WANG

Submitted to the Office of Graduate Studies of
Texas A&M University
in partial fulfillment of the requirements for the degree of

DOCTOR OF PHILOSOPHY

Approved by:

Chair of Committee,	Alexei V. Sokolov
Committee Members,	M. Suhail Zubairy
	George R. Welch
	Philip R. Hemmer
Head of Department,	Edward S. Fry

May 2011

Major Subject: Physics

ABSTRACT

Coherent Anti-Stokes Raman Scattering (CARS) Optimized

by Exploiting Optical Interference. (May 2011)

Xi Wang, B.S., Nanjing University;

M.S., Peking University

Chair of Advisory Committee: Alexei V. Sokolov

The purpose of this work is to study the interference between the coherent non-resonant four-wave-mixing (FWM) background and the Raman-resonant signal in the coherent anti-Stokes Raman spectroscopy (CARS). The nonresonant background is usually considered as a detriment to CARS. We prove that the background can be exploited in a controllable way, through the heterodyne detection due to the interference, to amplify the signal and optimize the spectral shape of the detected Raman signal, and hence enhance the measurement sensitivity.

Our work is based on an optimized CARS technique which combines instantaneous coherent excitation of multiple characteristic molecular vibrations with subsequent probing of these vibrations by an optimally shaped, time-delayed, narrowband laser pulse. This pulse configuration mitigates the nonresonant background while maximizing the resonant signal, and allows rapid and highly specific detection even in the presence of multiple scattering.

We investigate the possibility of applying this CARS technique to non-invasive monitoring of blood glucose levels. Under certain conditions we find that the measured signal is linearly proportional to the glucose concentration due to optical interference with the residual background light instead of a quadratic dependence, which allows reliable detection of spectral signatures down to medically-relevant glucose levels.

With the goal of making the fullest use of the background, we study the inter-

ference between an external local oscillator (nonresonant FWM field) and the CARS signal field by controlling their relative phase and amplitude. Our experiment shows that this control allows direct observation of the real and imaginary components of the third-order nonlinear susceptibility ($\chi^{(3)}$) of the Raman sample. In addition, this method can be used to amplify the signal significantly.

Furthermore, we develop an approach by femtosecond laser pulse shaping to precisely control the interference between the Raman-resonant signal and its intrinsic nonresonant background generated within the same sample volume. This technique is similar to the heterodyne detection with the coherent background playing the role of the local oscillator field. By making fine adjustments to the probe field shape, we vary the relative phase between the resonant signal and the nonresonant background, and observe the varying spectral interference pattern. These controlled variations of the measured pattern reveal the phase information within the Raman spectrum, akin to holographic detection revealing the phase structure of a source.

To my family

ACKNOWLEDGMENTS

The completion of a PhD study, especially in experimental science, is obviously not possible without the personal and practical support of numerous people. Thus, my sincere gratitude goes to my advisor, my committee members, my colleagues, all my friends, my parents, my husband, and my daughter for their direct or indirect support, love and patience over the last several years.

My special thanks go to my committee chair, Dr. Alexei V. Sokolov, as my mentor and friend. He has been always supportive, encouraging and patient during my PhD study. I learned a lot from his spirit in research and supervision. His ingenious ideas never cease to amaze me, and lead to many fruitful results. I would like to thank my committee member, Dr. George R. Welch, for his instruction and support throughout my study. It has been always enjoyable and inspiring to talk with him. I am also grateful to Dr. Marlan O. Scully for his guidance and support throughout my study. His sharp thinking and hard work always inspired me. I also appreciate my committee members, Dr. Philip R. Hemmer and Dr. M. Suhail Zubairy, for their helpful discussions and collaborations.

Thanks also to my collaborators, Dr. Vladislav V. Yakovlev (University of Wisconsin-Milwaukee), Dr. Jaan Laane (Department of Chemistry at TAMU), Dr. Aleksei M. Zheltikov for their valued contributions at different stages of this work. I am grateful to my TAMU co-workers, Dr. Dmitry Pestov, Dr. MiaoChan Zhi, Dr. Robert Murawski, Dr. Aihua Zhang, Dr. Yuri Rostovtsev, Dr. Vladimir Sautenkov, Dr. Gombojav Ariunbold, Kai Wang, Xia Hua, Steve Scully, Luqi Yuan, Dr. Dmitri Voronine, Wenlong Yang, Andrew Traverso, and Alexander Sinyukov. Their help was essential in many of the projects. It has been a great pleasure to discuss and learn from them.

I also want to extend my gratitude to the staff members, Kim Chapin and Clayton Holle, at the Institute for Quantum Science and Engineering, and the Physics Department for making my time at Texas A&M University a pleasant experience.

Last, but not least, I thank my friends, Dr. Jiahui Peng, Dr. Hebin Li, Dr. Juntao Chang, Dong Sun, Eyob Sete, Shuai Yang, and many more for their help in life and research. Thanks to my parents for their encouragement, and to my husband Dr. Qingqing Sun, who has been my classmate, officemate, and also collaborator, for his patience, love and lots of discussions on physics.

TABLE OF CONTENTS

CHAPTER		Page
I	INTRODUCTION	1
	A. Introduction to Raman spectroscopy	1
	B. Comparison between CARS and spontaneous Raman spectroscopy	2
	C. Coherent nonresonant FWM background in CARS	6
	D. Basic principles of CARS	9
	E. Isolating imaginary component of $\chi_R^{(3)}$	11
	F. The principles of our optimized hybrid CARS experiment	12
	G. Experimental setup	17
II	DETECTION OF BACTERIAL ENDOSPORES VIA A HYBRID OF FREQUENCY AND TIME RESOLVED CARS	21
	A. Introduction	21
	B. Theory of hybrid CARS technique	23
	C. Experimental implementation	26
	D. Experimental results	27
	1. Hybrid CARS on Na ₂ DPA powder	27
	2. Hybrid CARS on <i>B. subtilis</i> spores	30
	E. Conclusion	32
III	GLUCOSE CONCENTRATION MEASURED BY HYBRID CARS	34
	A. Introduction	34
	B. Raman cross-section of glucose	36
	C. Experimental setup	36
	D. Results and discussion	38
	1. Raman spectra	38
	2. Probe bandwidth	39
	3. Concentration dependence	41
	4. Glucose measurement in blood	45
	5. Phase changes in CARS signals	48
	E. Conclusion	50

CHAPTER	Page	
IV	HETERODYNE CARS FOR SPECTRAL PHASE RETRIEVAL AND SIGNAL AMPLIFICATION	51
	A. Introduction to interferometric CARS	51
	B. Experimental setup	53
	C. Interferometric FWM spectra from glass	55
	D. Interferometric CARS spectra from methanol	59
	1. Phase change in the CARS spectra	59
	2. Extracting the real and imaginary components of $\chi_R^{(3)}$	62
	3. Heterodyne amplification	64
	E. Conclusion	64
V	PULSE-SHAPER-ENABLED PHASE CONTROL OF NON- RESONANT BACKGROUND FOR HETERODYNE DE- TECTION OF CARS SIGNAL	66
	A. Introduction	66
	1. Development of interferometric CARS	66
	2. Intrinsic nonresonant FWM background as the LO	66
	B. Spectral asymmetry induced temporal phase shift in probe field	68
	C. “Temporal Gouy phase”	71
	D. Experimental setup	72
	E. Experimental results	73
	1. Asymmetric probe spectra	73
	2. Phase shift near the first probe node	74
	3. Extraction of the real and imaginary components of $\chi_R(\omega)$	76
	4. Controllable FWM amplitude	78
	5. Asymmetry induced phase shift for CARS spectra with multiple Raman lines	79
	F. Conclusion	81
VI	CONCLUSIONS	82
	REFERENCES	85
	VITA	97

LIST OF FIGURES

FIGURE	Page
1	Energy level diagrams for the variations of Raman scattering 2
2	Diagrams to compare spontaneous and coherent Raman processes . . . 3
3	Comparison of different Raman spectroscopy techniques 4
4	Phase-matching conditions for CARS 5
5	Coherent background of CARS 7
6	Energy level diagrams for the coherent FWM background 8
7	Diagrams of the real and imaginary components of $\chi_R^{(3)}$ 12
8	Transition from time-resolved to hybrid CSRS 13
9	Diagram of a conventional time-resolved CARS 14
10	Temporal profiles of the fields in the hybrid CARS experiment 15
11	Typical spectral profiles of the fields in the hybrid CARS experiment 16
12	Schematics of a typical hybrid CARS setup 18
13	Etaloning from back-illuminated CCD 19
14	Schematic layout of frequency-resolved and time-resolved techniques for CARS 22
15	CARS and background responses to the probe pulse duration and its delay 25
16	Na ₂ DPA spontaneous Raman spectrum excited by 532 nm light. 28
17	CARS spectra of Na ₂ DPA 29
18	CARS spectra of B. subtilis spores 31

FIGURE	Page
19 Spontaneous Raman spectra of D-glucose	37
20 Fused silica cell for the forward CARS	38
21 CARS spectra of D-glucose solution at 2680 <i>mM</i>	40
22 CARS spectra of D-glucose solution with different concentrations . .	42
23 Nearly linear dependence of CARS signal intensity on D-glucose concentration	43
24 CARS spectra of pig blood	46
25 Glucose concentration dependence in pig blood	47
26 Phase dependence of the glucose CARS spectra on probe delay . . .	49
27 Schematic of the CARS spectral interferometer	54
28 Interference spectra at different time delays τ between the local oscillator and the signal fields.	55
29 Interference spectra of nonresonant signals with different phases . . .	56
30 Interferometric spectra of aqueous methanol solution at different phases ϕ between the LO and signal arms	58
31 Dependence of the interferometric spectra at fixed frequencies on the relative phase ϕ between the LO and signal fields.	61
32 Extracted susceptibility and heterodyne signal	63
33 Probe pulse in frequency and time domains	69
34 Phase change of the nonresonant FWM (ϕ) through the probe node .	70
35 Beam radius and Gouy phase shift along the propagation direction .	71
36 Collinear hybrid CARS setup	72
37 Spectral and temporal shapes of the probe beam	74

FIGURE		Page
38	Experimental CARS spectra of the methanol aqueous solution without and with a knife-edge	75
39	CARS spectra to show the real and imaginary part of $\chi_R^{(3)}(\omega)$	77
40	CARS spectra at the first probe node without and with a knife-edge	79
41	Phase changes of the CARS signal from 500 mM glucose aqueous solution near the probe nodes	80

CHAPTER I

INTRODUCTION

A. Introduction to Raman spectroscopy

The development of Raman spectroscopy has gone through spontaneous Raman scattering (SpRS, 1928) [1], stimulated Raman scattering (SRS, 1961) [2], coherent anti-Stokes (Stokes) Raman scattering (CARS or CSRS, 1964) [3, 4], and higher-order process such as BioCARS (1995) [5], with the progress of high-intensity laser pulses which makes possible the processes involving multiple photons, as shown in Fig. 1. Considerable work has also been done to combine other techniques with Raman spectroscopy such as the delicate surface or tip enhanced Raman spectroscopy (SERS or TERS) [6–10] associated with metal surface plasmons. The usual purpose of the many variations of Raman spectroscopy is to enhance the sensitivity (e.g., SERS), to improve the spatial resolution (Raman microscopy), or to acquire very specific information (resonance Raman).

Since its discovery, CARS has attracted much attention due to its superiorities including enhanced efficiency (by orders of magnitude) over spontaneous Raman emission, frequency shift from incident photons over SRS, relatively large third-order susceptibility over higher order processes, and also remain of the simplicity to be experimentally carried out over SERS [11–17]. It may be said that beyond conventional spontaneous Raman spectroscopy, CARS probably has the most general utility. CARS technique has been widely used for combustion (plasma) diagnostics [14] and species selective microscopy [16, 17], investigations of molecular dynamics [18], species concentration measurement [19–21]. The applications and explorations of

The journal model is *Optics Express*.

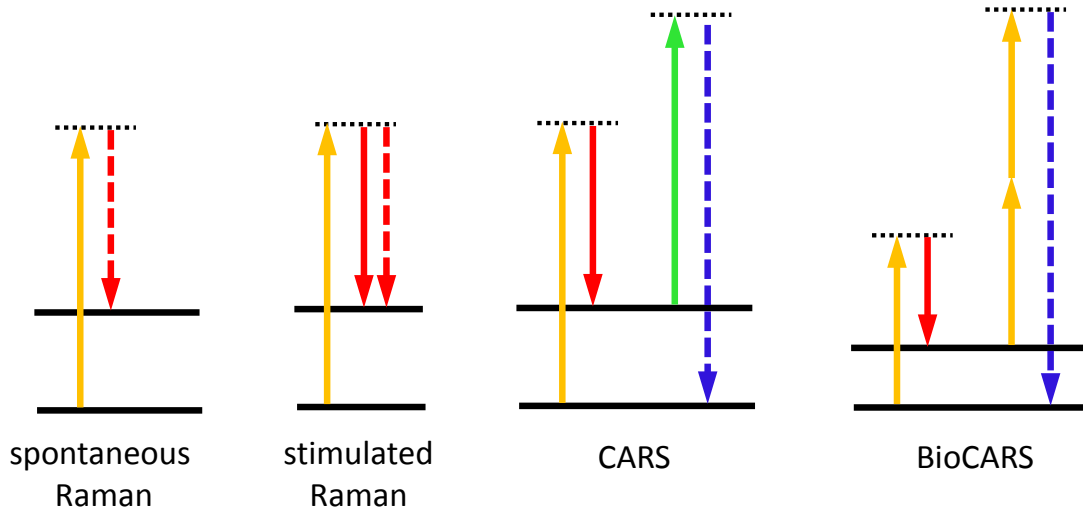


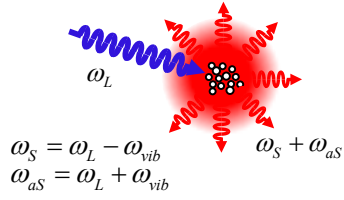
Fig. 1. Energy level diagrams for the variations of Raman scattering. From left to right: spontaneous Raman scattering, stimulated Raman scattering, coherent anti-Stokes Raman scattering (CARS), and higher order process (BioCARS). Solid arrows represent incident photons and dashed arrows represent generated signal photons.

CARS technique saw its breakthrough with the impressive progress of femtosecond lasers in the 1990s, which gives rise to new ideas and approaches to optimize CARS generation and detection, such as time-resolved CARS [18, 22–32], multiplex (broad-band) CARS [33–39], pulse-shaping assisted CARS [40–42].

B. Comparison between CARS and spontaneous Raman spectroscopy

CARS is often compared to spontaneous Raman spectroscopy as both techniques probe the same Raman active modes. Their essential difference is the coherence of molecular vibration created by the additional two preparatory pulses: the pump and Stokes in CARS, as shown in Fig. 2. Due to this coherence, the photons generated in CARS within the coherence length propagate phase-coherently relative to the incident fields and in a defined direction instead of with random phase and direction in

Spontaneous Raman scattering



Coherent anti-Stokes Raman scattering

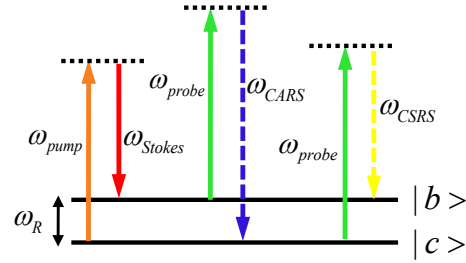
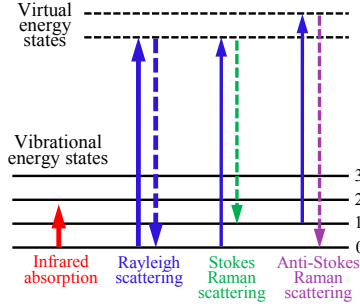
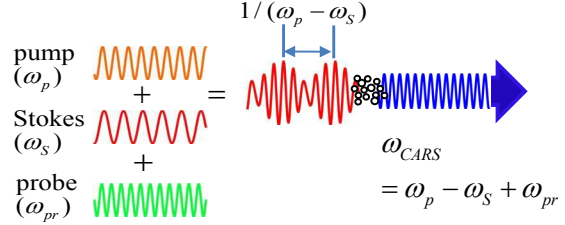


Fig. 2. Diagrams to compare spontaneous (left) and coherent (right) Raman processes.

The Raman resonance frequency is ω_R (only one is shown for simplification).

spontaneous Raman emission.

As one result of the coherence, CARS obtains significantly enhancement of the conversion efficiency reported by up to six orders over spontaneous Raman [3, 4, 12], as shown in Fig. 3. The absolute efficiency of the incident pulse could be around 10^{-3} over 10^{-8} from benzene. Generally the ratio of the number of photons generated through coherent anti-Stokes (or Stokes) scattering to the number of spontaneously scattered (Stokes) Raman photons, equal to [43, 44]

$$\frac{\langle n \rangle_{CARS/CSRS}}{\langle n \rangle_{SPRS}} = \lambda^2 \frac{N}{V} \frac{|\rho_{bc}|^2}{\rho_{cc}} \Delta L \quad (1.1)$$

λ_{pr} is the wavelength of the probe pulse, ΔL is the length of the medium, and N/V is the concentration of the target molecules; ρ_{cc} is the population of the molecular ground state $|c\rangle$; and ρ_{bc} is the coherence between the state $|c\rangle$ and excited Raman

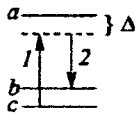
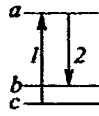

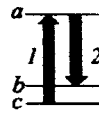
Process	Raman coherence ρ_{cb}	Dipole coherence ρ_{ab}
<p>Raman</p>  <p>(Weak drive)</p>	$i \frac{\Omega_2 \Omega_1^*}{\gamma_{bc} \Delta}$ <p style="text-align: center;">10^{-5}</p>	$-\frac{\Omega_2 \Omega_1 ^2}{\Delta \Delta \gamma_{bc}}$ <p style="text-align: right;">(incoh.)</p> <p style="text-align: right;">10^{-9}</p>
<p>Resonant Raman</p>  <p>(Weak drive)</p>	$-\frac{\Omega_2 \Omega_1^*}{\gamma_{ac} \gamma_{bc}}$ <p style="text-align: center;">10^{-2}</p>	$\frac{\Omega_2 \Omega_1 ^2}{\gamma_{ab} \gamma_{ac} \gamma_{bc}}$ <p style="text-align: right;">(incoh.)</p> <p style="text-align: right;">10^{-3}</p>
<p>Raman</p>  <p>(Strong drive)</p>	$i \frac{\sqrt{\gamma_1}}{4 \gamma_{bc}}$ <p style="text-align: center;">(max. coh.)</p> <p style="text-align: center;">10^{-3}</p>	$i \frac{1}{4} \frac{\Omega_2}{\Delta} \sqrt{\frac{\gamma_1}{\gamma_{bc}}}$ <p style="text-align: right;">(max. coh.)</p> <p style="text-align: right;">10^{-6}</p>
<p>Resonant Raman</p>  <p>(Strong drive)</p>	$\frac{1}{2}$ <p style="text-align: center;">(max. coh.)</p> <p style="text-align: center;">10^0</p>	$\frac{i \Omega_1}{2 \gamma_{ab}}$ <p style="text-align: right;">(max. coh.)</p> <p style="text-align: right;">10^{-1}</p>

Fig. 3. Comparison of different Raman spectroscopic techniques [45].

active state $|b\rangle$.

We have proven this efficiency enhancement through different experiments. For the experiment with pyridine in a $\Delta L = 200 \mu m$ cell, a ratio of 10^5 is obtained [43]; while for another case with CaDPA sample $\Delta L \approx 1 \mu m$, the enhancement is around 500 [44]. However, in both cases, we have $\rho_{bc} \approx 10^{-3}$.

From the Eq.(1.1) and our experiments where the interacting length ΔL does affect the conversion efficiency, we can see that it is the coherent addition of the CARS signal from the molecules that yields a total signal much higher than the spontaneous

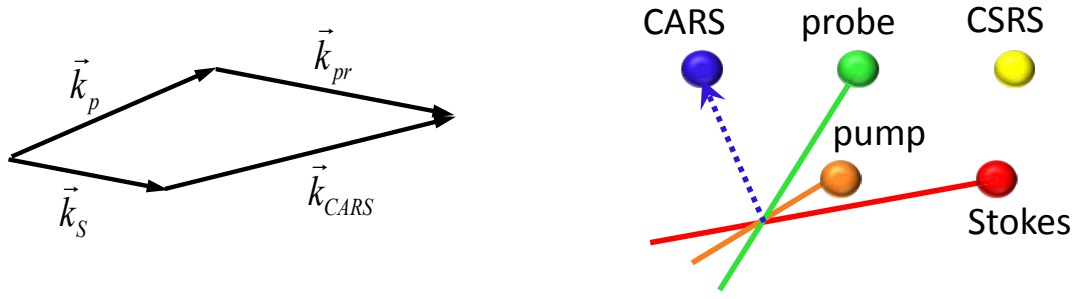


Fig. 4. Phase-matching conditions for CARS. The vector diagram (left) and general BOXCARS* geometry for CARS and CSRS generation (right).

* “Crossed-beam phase-matched CARS generation” [46].

Raman. We should be aware that the spontaneous Raman signal for a single molecule may exceed the CARS for a single molecule by more than two orders of magnitude, since CARS is a third-order nonlinear process ($\chi^{(3)}$) while spontaneous Raman is a linear process.

Another important advantage of CARS is the directionality of the generated laser-like signal so that all of the signal can be easily collected, as shown in Fig. 4. In the CARS process, the energy conservation leads to generation of photons at a new frequency, determined by the pump(ω_p), Stokes(ω_S) and probe fields(ω_{pr}),

$$\omega_{CARS} = \omega_p - \omega_S + \omega_{pr}. \quad (1.2)$$

Similarly, momentum conservation requires (see Fig. 4)

$$\vec{k}_{CARS} = \vec{k}_p - \vec{k}_S + \vec{k}_{pr}. \quad (1.3)$$

And as another result of the vibrational coherence, the generated CARS field propagates in this specific direction of \vec{k}_{CARS} . To fulfill this phase-matching condition, proper spatial configuration of the three beams (angles between them) is needed to minimize the loss of signal [47, 48]. The phase-mismatching, resulting from the dis-

persion in the linear refractive index (n) of the matter,

$$\Delta k = k_{CARS} - n_{CARS}\omega_{CARS}/c \quad (1.4)$$

needs to be taken into account when we analyze CARS generation [21, 49, 50], where n_{CARS} is the refractive index of the medium at frequency ω_{CARS} .

CARS is free from fluorescence background since the CARS signal is blue-shifted while the fluorescence is red-shifted. This property offers CARS promising applications in chemical, biological and biomedical imaging [17, 40, 51]. However, CARS is not background free. The presence of the inherent coherent nonresonant background and the complexity involved in suppressing the background restrict the applications of CARS, and sometimes are fatal so that people give up and seek other background-free approaches such as stimulated Raman [52, 53].

C. Coherent nonresonant FWM background in CARS

As it is stated above, CARS spectroscopy is a powerful technique for molecular detection which combines high sensitivity with inherent chemical selectivity. CARS occurs when molecules of interest, coherently excited by light pulses, scatter laser light to produce spectral components shifted by the molecular oscillation frequencies. It directly utilizes the vibrational response of the detected molecules themselves as a contrast mechanism. Chemical selectivity is afforded by the species-specific molecular vibrational spectra, and sensitivity is enhanced due to the coherent nature of the scattering process [43, 44]. Briefly, CARS is a third order nonlinear process which involves three laser beams: two preparatory pulses of pump and Stokes with respective frequencies ω_p and ω_S to create coherent molecular vibration when the frequency difference $\omega_p - \omega_S$ matches a vibrational transition of the sample, and a third probe pulse

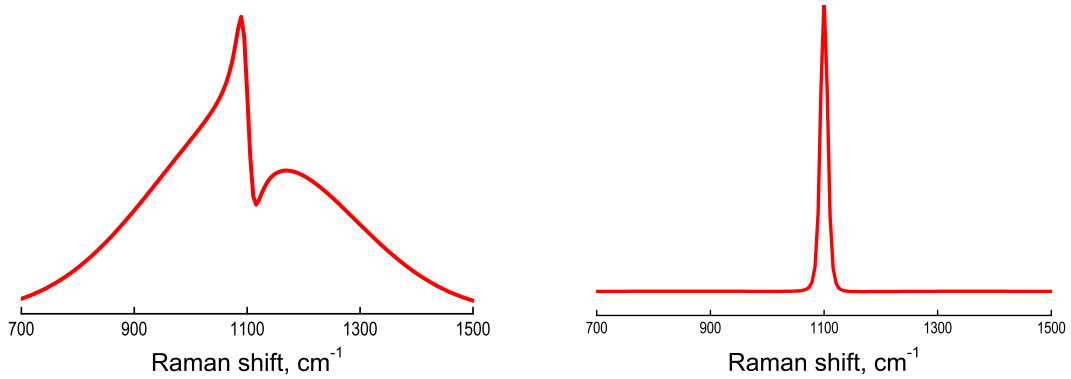


Fig. 5. Coherent background of CARS. Calculated CARS spectra with (left) and without (right) the coherent background, with pump($\lambda \approx 1290 \text{ nm}$, FWHM $\approx 50 \text{ nm}$), Stokes($\lambda \approx 1510 \text{ nm}$, FWHM $\approx 70 \text{ nm}$), and probe($\lambda \approx 806 \text{ nm}$, top-hat spectral shape, FWHM $\approx 1.1 \text{ nm}$).

at ω_{pr} to generate a blue-shifted fingerprint CARS signal at $\omega_{CARS} = \omega_p - \omega_S + \omega_{pr}$.

However, CARS from the molecules of interest is frequently masked by a broad-band featureless nonresonant coherent four-wave mixing (FWM) background which is independent of the Raman shift and often is much stronger [4, 12, 44]. Even when CARS lines are clearly discernable, the interference with this coherent background results in a strong distortion of the measured spectrum hence limits the detection sensitivity. In particular, while the phase of the background is constant, the CARS phase varies with frequency between 0 and π when tuning through the molecular line. As a result, at some frequencies the interference between signal and background is constructive or destructive, while at others the signal and background fields are in quadrature, as seen in Fig. 5.

The nonresonant FWM contribution is inherently included in the third order process $\chi^{(3)} = \chi_{NR}^{(3)} + \chi_R^{(3)}$ [3, 12] and thus unavoidable in CARS. It results from a few virtual electronic transition processes, as shown in Fig. 6, involving remote Raman modes, one- and two-photon absorptions. It always contributes to the signal field even

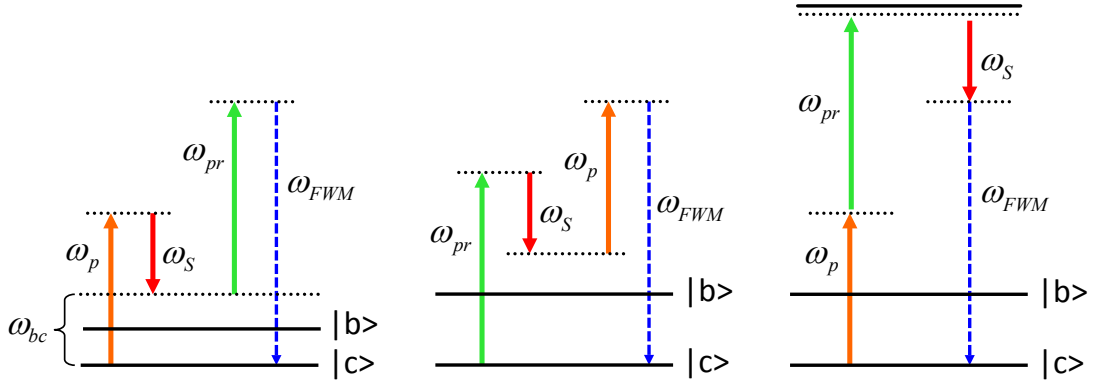


Fig. 6. Energy level diagrams for the coherent FWM background.

far from resonances, and fluctuations in this signal due to laser-intensity fluctuations seriously limit the sensitivity of most coherent Raman techniques. This limitation was first predicted by Yajima in 1965 [54] and “is in fact a major stumbling block in the present day application of four-wave mixing to Raman spectroscopy” [12, 55].

The FWM background is usually considered as a detriment to CARS. When this background is large, its inevitable random fluctuations obscure the CARS signal. Many methods have been developed to suppress the nonresonant background, such as the polarization sensitive detection [50, 56–58], time-resolved CARS [18, 22, 24, 26, 28–32], and pulse shaping [40, 42, 59–61]. Nonlinear interferometry is another approach to suppress the nonresonant background, i.e., to extract the resonant field component of the CARS signal by means of a phase-sensitive measurement [62–72]. This technique can be made to detect the imaginary part of the nonlinear susceptibility $\text{Im}[\chi^{(3)}]$ of the CARS signal, which then can be directly compared to the spontaneous Raman spectrum.

D. Basic principles of CARS

The theory of CARS is well known. A detailed description of the theoretical background of CARS can be found in many books [12, 13]. Briefly, the analysis of the amplitude, phase and polarization of the CARS signal involves the solution of Maxwell equations for the field of the anti-Stokes wave and the calculation of the cubic polarization of a nonlinear medium with either classical [12] or quantum mechanical [13] model of the non-linear response.

Assuming that the CARS process involves plane and monochromatic waves, the macroscopic polarization density amplitude can be generally expressed as

$$P_i(\omega_{CARS}) = \frac{3}{4} \chi_{ijkl}^{(3)}(-\omega_{CARS}, \omega_p, -\omega_S, \omega_{pr}) E_j(\omega_p) E_k^*(\omega_S) E_l(\omega_{pr}) Lsinc\left(\frac{\Delta k L}{2}\right) \quad (1.5)$$

This expression includes three parts: the third-order nonlinear susceptibility tensor $\chi_{ijkl}^{(3)}$, the real incident fields $E_\alpha(\omega_\beta)$ of frequency ω_β and polarization axis α , and the phase-matching term $Lsinc(\Delta k L/2)$, where Δk can be calculated from Eq. (1.3). Certainly it is important to fulfill the phase-matching conditions with $\Delta k = 0$ or proper coherent length so that $\Delta k L/2 = \pi/2$ to optimize the CARS generation. Also the electric fields $E_\alpha(\omega_\beta)$ should be high enough to excite this third-order process so high peak-power pulsed lasers are required. Nevertheless, of particular importance is the term $\chi_{ijkl}^{(3)}$, which contain resonant Raman contribution as well as nonresonant FWM background contribution and can be expressed as

$$\chi_{ijkl}^{(3)} = \chi_{NR}^{(3)} + \chi_R^{(3)} = \chi_{NR}^{(3)} + \frac{N\alpha_R}{\omega_R - (\omega_p - \omega_S) - i\Gamma_R} \frac{d\sigma}{d\Omega} \quad (1.6)$$

where α_R , ω_R , and Γ_R are respectively the amplitude, frequency, and spectral half

width (HWHM, not FWHM) of the resonance vibrational mode, N is the density (concentration for mixture) of Raman active molecule, and $\frac{d\sigma}{d\Omega}$ is the differential spontaneous Raman scattering cross section.

In the case of broadband excitation fields, multiple vibrational modes may be excited. CARS signal generation is through the third-order polarization which can be written as the sum of the background and resonant contributions [59,60]:

$$\begin{aligned} P_{\text{CARS}}^{(3)}(\omega) &= P_B^{(3)}(\omega) + P_R^{(3)}(\omega) \\ &= \int_0^\infty d\Omega \left(\chi_B^{(3)}(\Omega) + N\chi_R^{(3)}(\Omega) \right) E_{pr}(\omega - \Omega) R(\Omega), \end{aligned} \quad (1.7)$$

$$R(\Omega) = \int_0^\infty E_p(\omega') E_S(\omega' - \Omega) d\omega', \quad (1.8)$$

where $E_{pr}(\omega)$ is the probe field; $S(\Omega)$ is the convolution of the pump field $E_p(\omega)$ and Stokes field $E_S(\omega)$. Here the subscript ‘‘NR’’ is replaced by ‘‘B’’ which means background for more general use since for some sample, especially aqueous solution, the solvent may have a broadband resonant contribution instead purely nonresonant contribution as usually treated. This is an important discovery from our experiment [72] and it should be considered for low concentration measurement and biological imaging. Most often although not always, $\chi_B^{(3)}$ corresponds to nonresonant response and is purely real while the resonant susceptibility $\chi_R^{(3)}$ is complex and, for the case of Lorentzian lineshape, can be written as:

$$\chi_R^{(3)}(\omega) = \sum_j \frac{A_j}{\Omega_j - \omega - i\Gamma_j} \frac{d\sigma}{d\Omega}, \quad (1.9)$$

where $\omega = \omega_{\text{pump}} - \omega_{\text{Stokes}}$; A_j , Ω_j and Γ_j are the amplitude, frequency and spectral half width of the j -th vibrational mode, respectively. The total CARS signal is given

by

$$S_{\text{CARS}}(\omega) = \left| P_B^{(3)} + P_R^{(3)} \right|^2 = \left| P_B^{(3)} \right|^2 + \left| P_R^{(3)}(\omega) \right|^2 + 2\text{Re} \left[P_B^{(3)} P_R^{(3)*}(\omega) \right]. \quad (1.10)$$

The background component $\left| P_B^{(3)} \right|^2$ limits the sensitivity of CARS measurements. For FWM nonresonant background and some broadband resonant background (e.g. from water) $P_B^{(3)}$ is insensitive to frequency, the interference term (the third one on the right) actually is $P_B^{(3)} * \text{Re} \left[P_R^{(3)*}(\omega) \right]$.

However, quite often the resonant signal $\left| P_R^{(3)}(\omega) \right|^2$ is very weak; then a proper residual of nonresonant background $P_B^{(3)}$ can improve the detection by amplifying the signal; this will be covered in Chapter III “Glucose concentration measured by hybrid CARS”. Also, we figure out ways to obtain the imaginary component of resonant susceptibility $\text{Im} \left[P_R^{(3)*}(\omega) \right]$, by introducing an external nonresonant interfering field in Chapter IV “Heterodyne CARS for spectral phase retrieval and signal amplification”, or by controlling the interference between the resonant Raman signal and the intrinsic nonresonant background in Chapter V “Pulse-shaper-enabled phase control of nonresonant background for heterodyne detection of CARS signal”.

E. Isolating imaginary component of $\chi_R^{(3)}$

Nonlinear interferometry [62–72] is a method to extract the imaginary component of $\chi_R^{(3)}$, and certainly avoiding the real component, without the effort to suppress the nonresonant background but exploiting it. This idea comes from the fact that the $\text{Im} \left[\chi_R^{(3)} \right]$ resembles the spontaneous Raman spectra [64, 66].

$$\text{Im} \left[\chi_R^{(3)}(\omega) \right] = \sum_j \frac{A_j \Gamma_j}{(\Omega_j - \omega)^2 + \Gamma_j^2}, \quad (1.11)$$

It is the real component $\text{Re} \left[\chi_R^{(3)} \right]$ that distorts the CARS spectra, as shown in

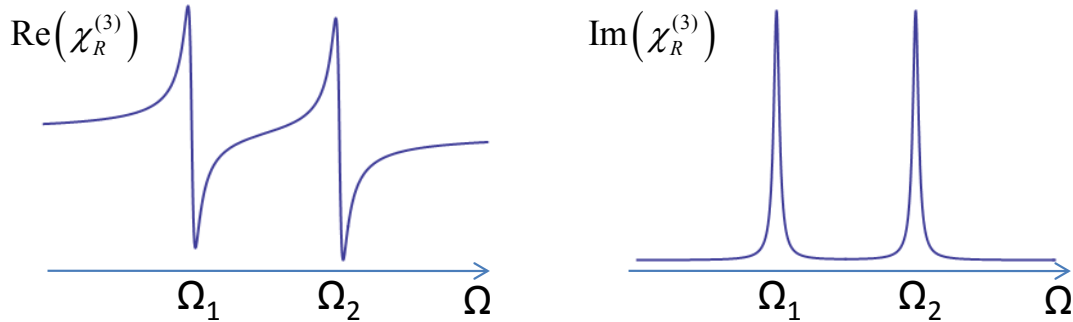


Fig. 7. Diagrams of the real and imaginary components of $\chi_R^{(3)}$.

Fig. 7. This distortion shifts the peak frequency and changes the spectral shape, which make spectral recognition difficult, especially for close Raman lines.

F. The principles of our optimized hybrid CARS experiment

Our optimized CARS scheme is a combination of multiplex CARS and time-resolved CARS, where background suppression is accomplished by shaping and delaying the probe laser pulse such that it has zero temporal overlap with the pump and Stokes pulses [20, 32, 35, 42, 43, 72]. Our work on hybrid CARS has been based on our earlier experience with IR, visible, and UV coherent Raman spectroscopy [73]. It is an extension of the precious work: FAST CARS “femtosecond adaptive spectroscopic techniques for coherent anti-Stokes Raman spectroscopy” [21, 45, 73]. While FAST CARS emphasizes clever pulse shaping for maximal coherence preparation, the hybrid CARS stresses optimum shaping of the probe laser pulse.

For multiplex CARS [33–39, 66], e.g. frequency-resolved CARS, at least one of the pump and Stokes pulses is required to be spectrally broadband to excite multiple vibrational frequencies simultaneously, and the probe is required to be spectrally narrowband. The employed hybrid technique can be best understood through its

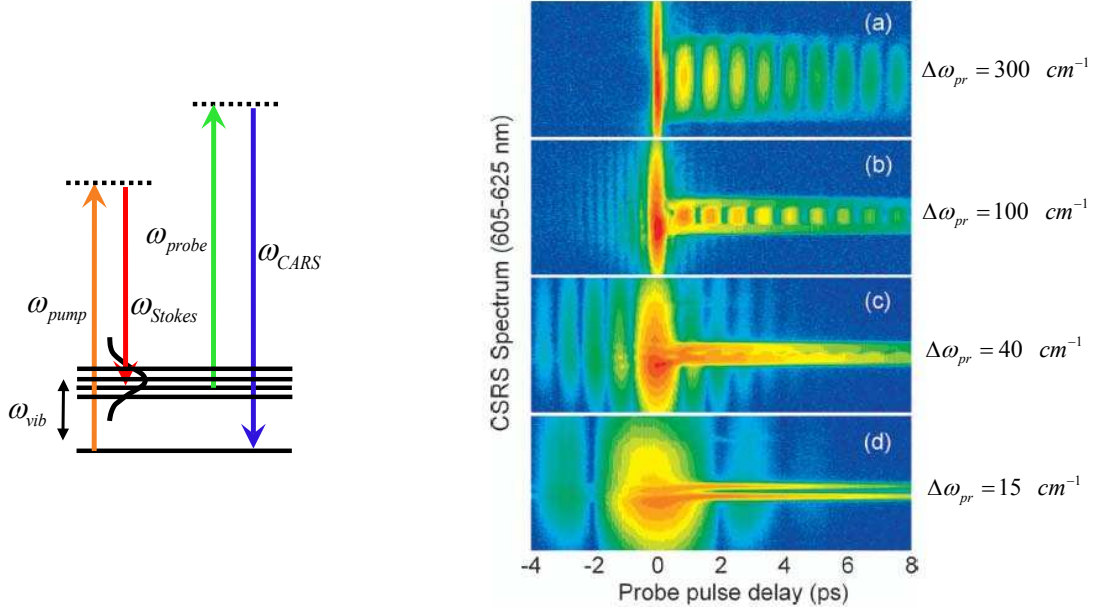


Fig. 8. Transition from time-resolved to hybrid CSRS. CSRS spectrograms for different spectral bandwidths of the probe pulse: (a) 300 cm^{-1} , (b) 100 cm^{-1} , (c) 40 cm^{-1} , (d) 15 cm^{-1} . Two Raman lines of pyridine, 992 and 1031 cm^{-1} , are excited via a pair of ultrashort laser pulses. Pump: $\lambda_p = 737 \text{ nm}$, $\text{FWHM} \approx 260 \text{ cm}^{-1}$, $0.5 \mu\text{J}/\text{pulse}$. Stokes: $\lambda_S = 801 \text{ nm}$, $\text{FWHM} \approx 480 \text{ cm}^{-1}$, $0.9 \mu\text{J}/\text{pulse}$. Probe: $\lambda_{pr} = 577.9 \text{ nm}$, $0.15 \mu\text{J}/\text{pulse}$.

comparison with time-resolved CARS (CSRS). From Eqs. (1.7) and (1.9), we can see that the CARS spectrum is the convolution of the probe field and the third order susceptibility $\chi_R^{(3)}$. The detected Raman linewidth is determined by the probe bandwidth and the bandwidth of the vibrational mode, whichever is larger. Therefore, to obtain the actual Raman spectrum, the probe bandwidth should be less than or equal to the Raman linewidth.

Figure 8 illustrates the transition from the traditional time-resolved measurement of free-induction decay in pyridine to the frequency-resolved one while the bandwidth of the probe pulse is reduced from 300 cm^{-1} to 15 cm^{-1} . The beating pattern between two excited Raman modes, 992 and 1031 cm^{-1} , gradually transforms into a couple

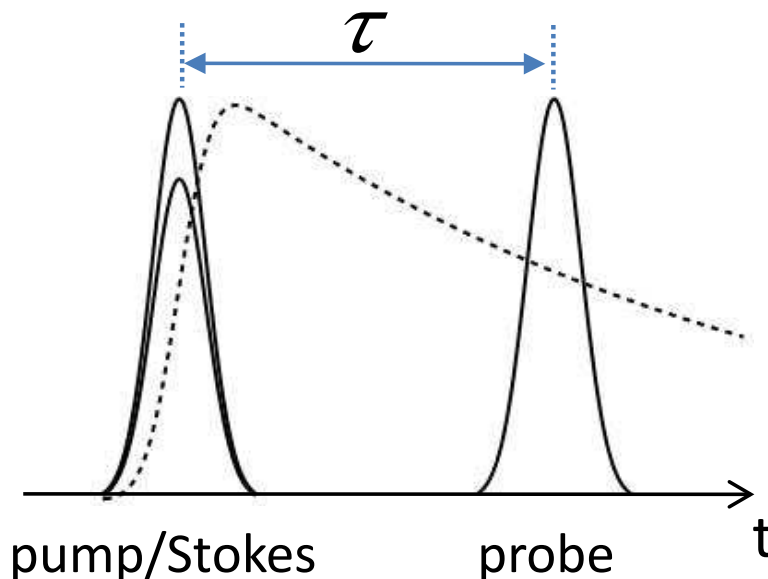


Fig. 9. Diagram of a conventional time-resolved CARS. Solid curves, incident pulses; dashed curve, decay of coherent vibrations ; τ , the delay time between the pump/Stokes and probe pulses.

of spectrally isolated streak lines. The smooth fourwave- mixing (FWM) profile due to multiple offresonant vibrational modes and the instantaneous electronic response stretches along the time axis (indicating the expected lengthening of the probe pulse) and gain side-fringes due to the rectangularlike spectral amplitude transmission mask we used. A cross section of the spectrograms for the narrowband probe at some fixed positive delay gives a CSRS spectrum.

The idea of time-resolved CARS [18,22–32] is that a pair of pulses with a duration shorter than the characteristic transverse relaxation time induces coherent molecular vibrations, and the decay kinetics of these vibrations are analyzed with the use of another, probe pulse, which is delayed in time with respect to the pump and Stokes pulses, as shown in Fig. 9. The method of time-resolved CARS implies that the information on the parameters of atomic or molecular systems is extracted from an impulse

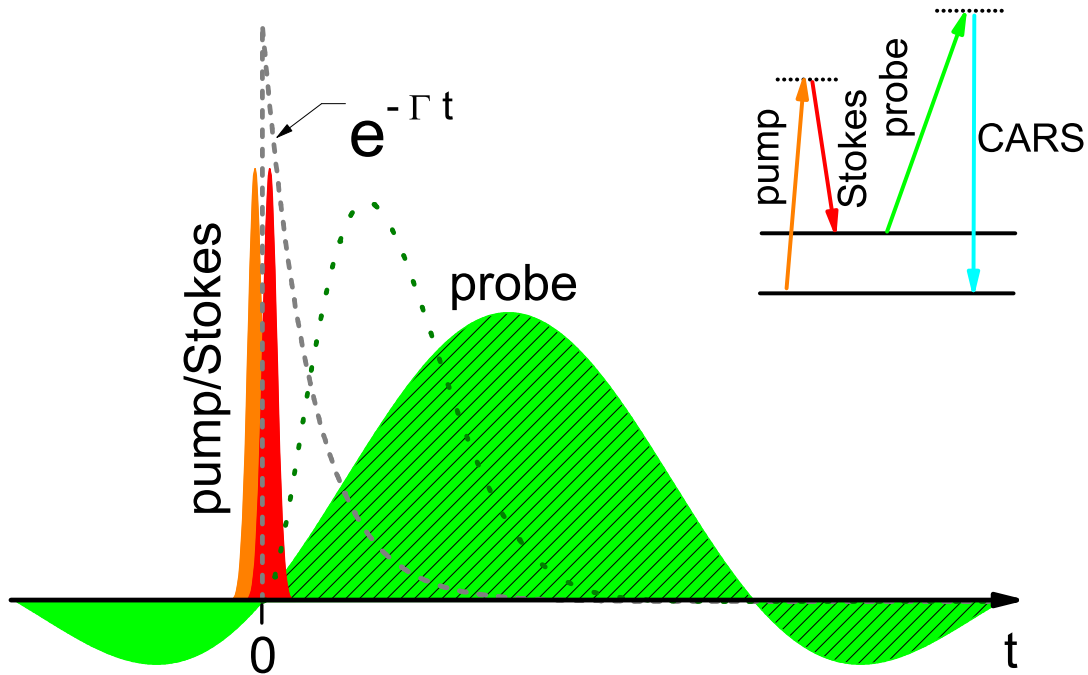


Fig. 10. Temporal profiles of the fields in the hybrid CARS experiment. The Gaussian pump and Stokes fields are in orange and red, and delayed sinc-like probe field is in green. The dashed curve shows the decay of molecular vibration $e^{-\gamma t}$. The dotted curve shows the contribution of the probe to the resonant signal at different time. Inset, energy level schematic diagram of CARS.

response of a coherently excited system rather than from the frequency dispersion of non-linear susceptibilities, as it is done in frequency-domain spectroscopy.

The time-resolved CARS not only provides molecular vibration dynamics by recording the Raman free induction decay information in the time domain [25–28], but also is an alternative approach to separate the nonresonant contribution, which is instantaneous, from the resonant contribution, which usually decays on a scale of picoseconds [29–32]. This method has been shown to enhance the contrast ratio considerably in CARS microscopy imaging [30]. However, as the background is suppressed, the resonant signal is attenuated too.

Our CARS scheme can be described in the time domain in Fig. 10 and in the

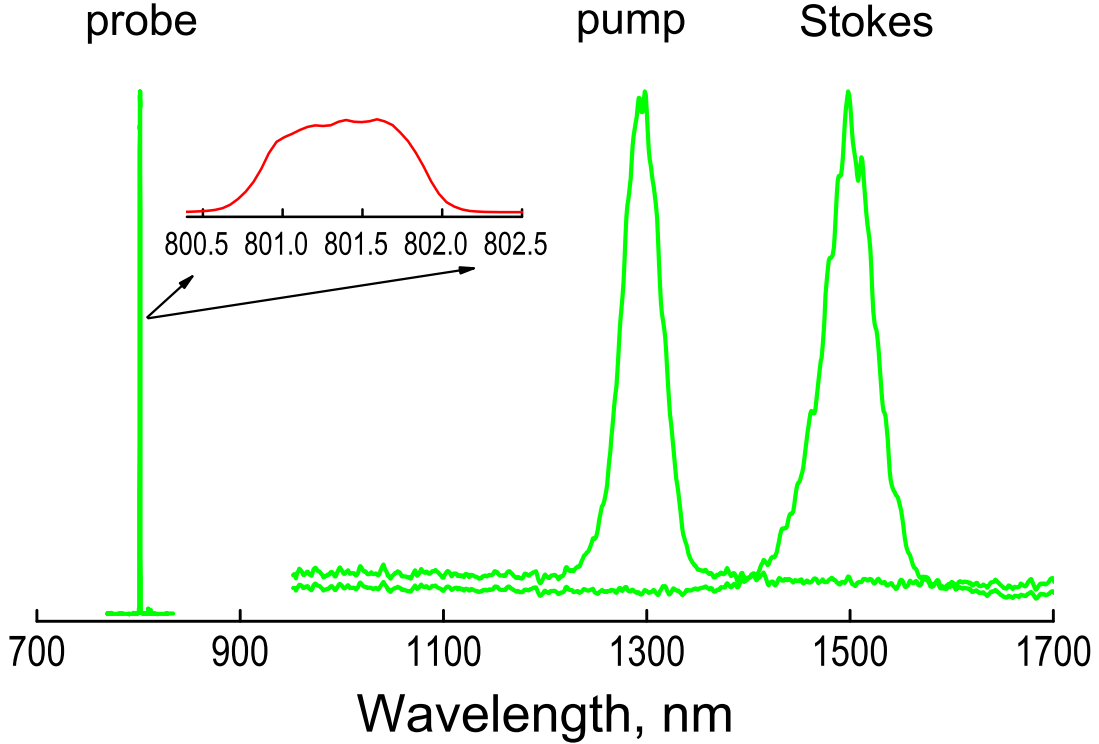


Fig. 11. Typical spectral profiles of the fields in the hybrid CARS experiment. Inset, enlarged probe spectrum with top-hat shape. The pump and Stokes spectra have a resolution of 1 *nm* from a near IR spectrometer (Stellar-Net, EPP2000-InGaAs-1024); the probe spectrum has a resolution of around 0.048 *nm* from a spectrograph (Chromex Spectrograph 250is) attached with a CCD (Princeton Instruments, Spec-10), which is used in the CARS measurement.

frequency domain in Fig. 11. It is realized by taking advantage of the fact that the nonresonant FWM is an instantaneous process so only the part of the probe pulse overlapping with the preparatory pulses at $t = 0$ contributes, while the resonant Raman signal is an accumulation process due to the vibrational coherence so all the parts of the probe when $t \geq 0$ (patterned in Fig. 10) contribute. In our experiment, as shown schematically in Fig. 10, we choose the pump and Stokes fields (orange and red shades) to be short and Gaussian, and the probe field (green shade) to be

much longer and a sinc-like function in the time domain corresponding to the top-hat spectrum as shown by the inset of Fig. 11. By placing the pump and Stokes pulses at the first node of probe, the nonresonant FWM background can be suppressed. In this configuration, the maximum of the instantaneous contribution from probe to the resonant Raman signal, described by the dotted curve, happens after the pump and Stokes with a fairly large time difference (at around half of the probe delay here), as a result of long-lasting vibrational coherence (dashed) and this specific probe shape. The collected resonant Raman field is an integration of the whole area under the dotted curve. When we delay the probe pulse to make the pump and Stokes pulses overlap with the node of the sinc function, the nonresonant background will be greatly reduced while the resonant signal will remain. However, in practice the background suppression is never perfect, and especially at low concentration of the target molecules the residual background often interferes with the CARS signal.

The same method of short-pulse excitation and time-delayed narrowband probing was developed as early as 1980 by Zinth and coworkers, with the aim of improving the spectral resolution of CARS beyond the limit of the homogeneous linewidth [74]. Similar mixed time-frequency methods have recently been realized by other groups [31].

G. Experimental setup

Figure 12 shows our typical experimental setup. This is just an example, i.e., incident beams are in a BOXCARS configuration and signal is collected in the forward direction. The incident beams could be arranged in a collinear configuration, the signal could be collected in other directions for scattering materials. We employ a Ti:sapphire regenerative amplifier (Coherent, Legend, 1 kHz rep. rate, 1 mJ/pulse)

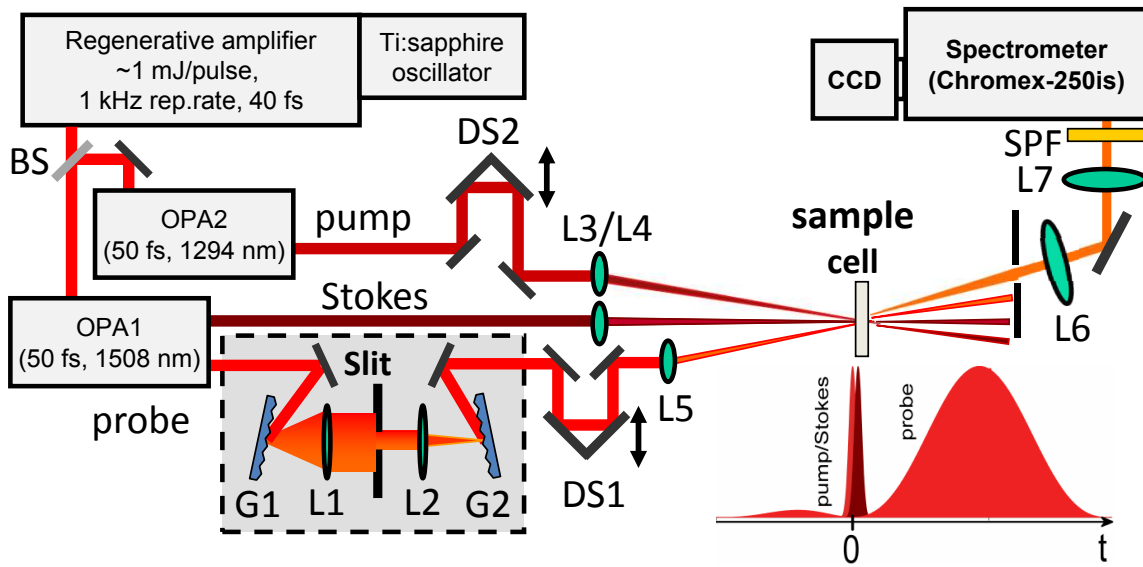


Fig. 12. Schematics of a typical hybrid CARS setup. The incident beams are in a BOXCARs configuration and signal is collected in the forward direction. BS: beam splitter; G1/G2, grating; L1-L7: lens; DS1/DS2: delay stage; SPF: short-pass filter.

with two evenly pumped optical parametric amplifiers (OPAs), (Coherent, OPerA-VIS/UV and OPerA-SFG/UV). These two OPAs with attached frequency conversion Extension Unit provide the pump and Stokes pulses with wavelengths vary from UV to near infrared. The frequency difference between the pump and Stokes beams is tuned to the vibrational levels, which optimizes the excitation of the Raman lines. The probe pulse is obtained when the residual fundamental pulse from the second OPA passes through a home-made 4-f pulse shaper consisting of a pair of gratings to expand the spectrum in space and a slit to pick a narrow spectral band. The probe beam then has a top-hat-like spectrum with width a few nm to match the linewidths of the vibrational modes. The probe width is chosen to be comparable with the spectral width of the vibrational modes (e.g. around 20 cm^{-1} for glucose) for the purpose of multiplex CARS detection as described in Ref. [35].

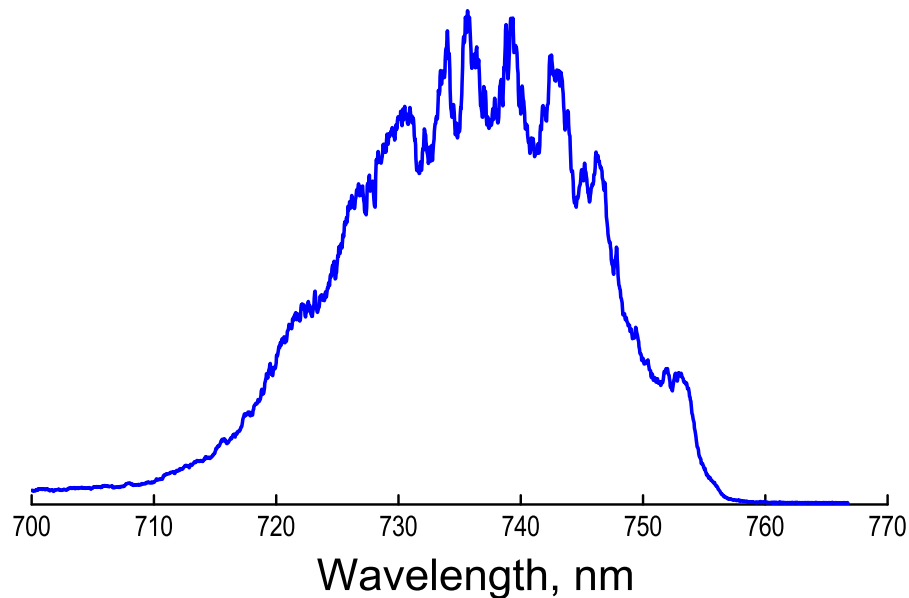


Fig. 13. Etaloning from back-illuminated CCD. This is a FWM spectrum from water collected with a back-illuminated CCD (Princeton Instruments, Spec-10, 2KBUV/LN). The fringes look like Raman lines but are not real. Here the sharp slope at the longer wavelength side of the spectrum is due to the cutoff by a short-pass filter.

These three pulses have parallel polarization and their time overlap is controlled by two translation stages (DS1 and DS2 in Fig. 12). They overlap at their focuses either in a crossing-beam configuration or in a collinear configuration. In our case, these two configurations produce similar results and detection sensitivity. The generated CARS signal is collected in a forward geometry and focused onto the entrance slit of the spectrograph (Chromex Spectrograph 250is) with a liquid nitrogen cooled charge-coupled device (CCD: Princeton Instruments, Spec-10) attached. Typical pulse energy is around a few hundred nanojoules to a few microjoules under different focusing conditions. A CCD exposure time of a few hundred ms to a few tens of seconds is used to adapt the signal intensity to the dynamic range of the CCD.

In Chapters IV and V, we used a UV-enhanced back-illuminated CCD (model: 2KBUV/LN). For the wavelength of the CARS signal at the range between 700 and 750 nm, because multiple reflections from the front and back of the active layer of the CCD interfere, these surfaces effectively form an etalon which produces a modulation in the recorded spectrum (etaloning), as shown by the CARS spectrum from water in Fig. 13. We eliminate this modulation by recording a reference spectrum from the broadband signal generated from a cell with water, and dividing the signal spectrum by this reference. This procedure introduces additional noise. In Chapter V, we use a Deep Depletion back-illuminated CCD (model: 400BR/LN) to solve this problem and eliminate the fringes in near IR range.

CHAPTER II

DETECTION OF BACTERIAL ENDOSPORES VIA A HYBRID OF
FREQUENCY AND TIME RESOLVED CARS*

A. Introduction

The purpose of this chapter is to briefly show how hybrid CARS works to suppress nonresonant FWM background for real-time detection of bacterial endospores.

In this chapter, we give a detailed description of a technique that we have recently used, which combines a generalized multiplex CARS scheme with the background reduction by using an optimally-shaped time-delayed probe pulse [35]. Similar schemes were also used by other groups for different purposes [31, 34]. This way of background suppression is reminiscent of the time-resolved femtosecond CARS technique [18, 22–32] (Fig. 14E). We diverge from the conventional multiplex CARS scheme [33–39, 66] and deal with the probe and two preparation pulses, pump and Stokes, separately (Figs. 14C,D). We demonstrate the efficacy of the ultrafast broadband excitation and time-variable narrowband probing (Fig. 14F). In particular, we show that adjusting the probe delay, one can suppress the NR background, as in time-resolved CARS, but keep the advantages of the multiplex CARS spectroscopy. We refer to this hybrid of frequency and time-resolved coherent Raman spectroscopy as hybrid CARS and demonstrate its utility by applying the technique to backscattered CARS on sodium dipicolinate (Na_2DPA) powder and bacterial spores. When we im-

*Part of the data reported in this chapter is reprinted with permission from “Optimizing the Laser-Pulse Configuration for Coherent Raman Spectroscopy” by D. Pestov et al., 2007. *Science*, 316, 265-268. Copyright 2007 by American Association for the Advancement of Science (AAAS).

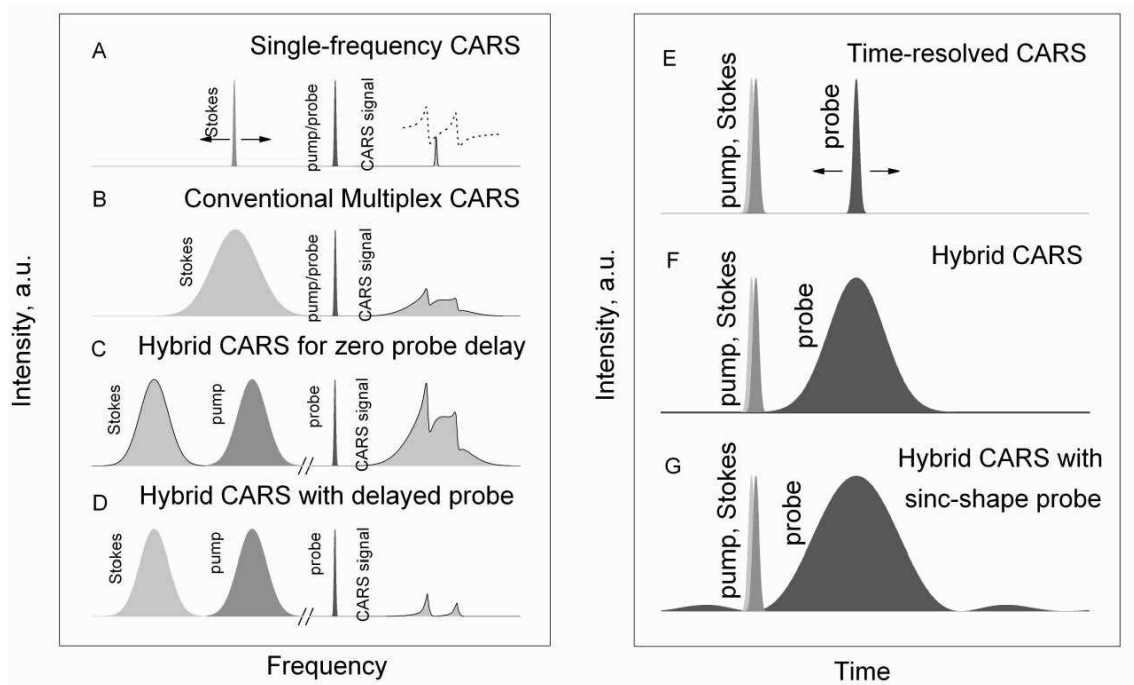


Fig. 14. Schematic layout of frequency-resolved and time-resolved techniques for CARS. The presence of two Raman lines within the considered band is implied: (A) “Single-frequency” CARS with two narrowband lasers, one of those is tuned; (B) Multiplex CARS with a combination of narrowband and broadband laser sources; (C) Hybrid CARS at zero probe delay, which is equivalent to non-degenerate multiplex CARS; (D) Hybrid CARS with the probe delayed. The presence of two Raman lines within the excitation band is implied. The nonresonant background suppression by proper timing of the probe pulse: (E) Time-resolved CARS, which implies the use of ultrashort pulses with the variable probe delay; (F) Hybrid CARS with the time-delayed probe, assuming it has Gaussian profile; (G) Hybrid CARS with the time-delayed probe, which has a rectangular-like spectrum and, therefore, sinc-shape.

proved the setup by shifting the wavelengths of the pump, Stokes, and probe beams into the near-IR domain, where the photo-damage threshold for the spores is higher as compared to the visible-range wavelengths, we obtained clean and strong CARS lines from endospores in the real time, i.e. fraction of a second. This result exhibits its potential application in detection of biohazards, such as *Bacillus anthracis*.

B. Theory of hybrid CARS technique

From Eqs. (1.7), we can see that the convolution of the pump and Stokes spectra, $R(\Omega)$, enters the two parts of the third-order polarization on equal grounds. It defines a Raman frequency band covered by the preparation pulses and is maximized for transform limited ones. The difference between the two contributions comes from the susceptibility and can be enhanced by the use of a properly-shaped probe. One way to proceed is to modify the spectral phase of the probe pulse, as it was demonstrated by Oron *et al.* [60]. The other is to shape its spectral profile, $|E_{pr}(\omega)|$, as we do here. If a narrowband probe is applied together with the broadband preparation pulses, the nonresonant contribution would have the spectral width of $R(\Omega)$, $\Delta\omega_{p-s}$, whereas the resonant part would result in a set of narrow peaks, one for each excited vibrational mode, whose width is determined either by the Raman line width or the probe spectral width, $\Delta\omega_{pr}$, whichever is greater.

The amplitude ratio between the resonant signal and the NR background at a Raman shifted frequency is also affected by the spectral width of the probe pulse. Under the simplest assumptions of Gaussian profiles of the three pulses with the convolution function $S(\Omega)$ centered on a single Raman line Ω_0 of the width 2Γ , at the zero probe delay, one can get

$$\begin{aligned} \frac{I_R(\omega_3 + \Omega_0)}{I_{NR}(\omega_3 + \Omega_0)} &= \left| \frac{P_R(\omega_3 + \Omega_0)}{P_{NR}(\omega_3 + \Omega_0)} \right|^2 \\ &= 2\pi Ln2 \left| \frac{A}{\chi_{NR}^{(3)}} \right|^2 \frac{\exp(4Ln2\Gamma^2/W^2)}{W^2} (1 - \text{erf}(\sqrt{2Ln2}\Gamma/W))^2 \end{aligned} \quad (2.1)$$

where $W = \Delta\omega_3\Delta\omega_{12}/\sqrt{\Delta\omega_3^2 + \Delta\omega_{12}^2}$, $\Delta\omega_3$ is the FWHM of the probe spectrum, and $\Delta\omega_{12}$ is the FWHM of $|S(\Omega)|^2$.

In the limit of a broadband probe, $\Delta\omega_3 \sim \Delta\omega_{12} \gg \Gamma$,

$$\frac{I_R(\omega_3 + \Omega_0)}{I_{NR}(\omega_3 + \Omega_0)} = \left| \frac{P_R(\omega_3 + \Omega_0)}{P_{NR}(\omega_3 + \Omega_0)} \right|^2 = \frac{2\pi Ln2}{W^2} \left| \frac{A}{\chi_{NR}^{(3)}} \right|^2. \quad (2.2)$$

For the narrowband probe, $\Delta\omega_3 \ll \Delta\omega_{12}$ and Γ

$$\frac{I_R(\omega_3 + \Omega_0)}{I_{NR}(\omega_3 + \Omega_0)} = \frac{1}{\Gamma^2} \left| \frac{A}{\chi_{NR}^{(3)}} \right|^2. \quad (2.3)$$

When the probe spectral width is between the Raman line width and the width of the pump-Stokes convolution profile, i.e. $\Gamma \ll \Delta\omega_3 \ll \Delta\omega_{12}$, as one has for multiplex CARS, this ratio is inversely proportional to the square of the probe spectral

$$\frac{I_R(\omega_3 + \Omega_0)}{I_{NR}(\omega_3 + \Omega_0)} = \frac{2\pi Ln2}{\Delta\omega_3^2} \left| \frac{A}{\chi_{NR}^{(3)}} \right|^2. \quad (2.4)$$

This ratio saturates at the limits and one gets a superior but finite signal-to-background ratio for the optimum probe width on the order of the Raman line width.

If the probe delay is adjustable, as it is in the scheme that we propose (see Figs. 14C,D,F), further optimization is possible. It can be shown that in the plane of two parameters (see Fig. 15A), the probe pulse duration and its delay, the resonant response peaks for the two on the order of inverse Raman line width. On the other hand, the NR background at the Raman shifted frequency is maximized for zero probe delay and its duration matched to the time span of the pump-Stokes convolu-

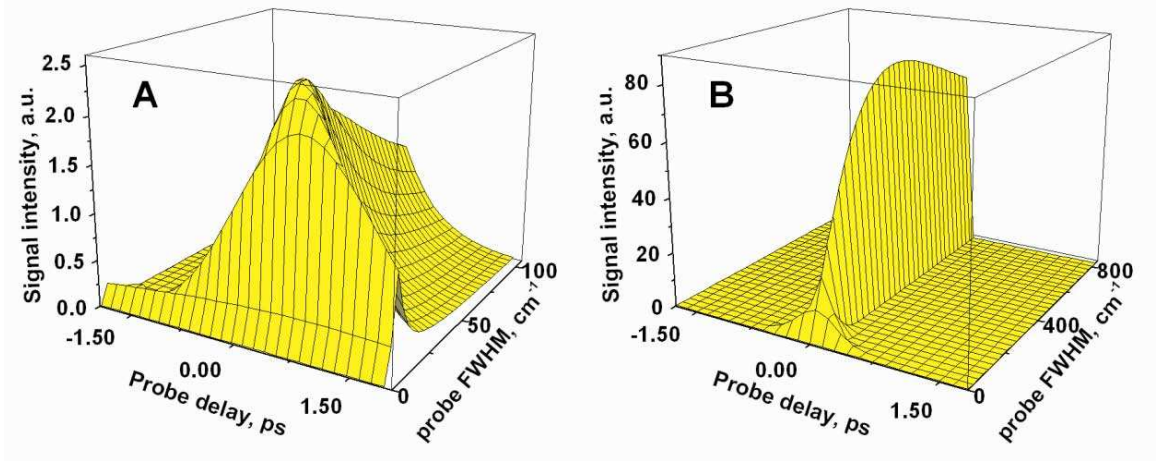


Fig. 15. CARS and background responses to the probe pulse duration and its delay. (A) Nonresonant background at the expected CARS peak frequency; (B) the resonant contribution at the expected CARS peak frequency ($\omega_{\text{CARS}} = \omega_{\text{Raman}} + \omega_{\text{probe}}$). The FWHM of the probe pulse is normalized on HWHM of the Raman transition. The probe pulse is normalized on its spectral width so that the same energy is delivered for different probe FWHM. The pulses used here are transform limited ones. The parameters used: the vibrational frequency $\Omega_j = 1402 \text{ cm}^{-1}$, the Raman line half-width $\Gamma_j = 5.3 \text{ cm}^{-1}$; $\lambda_{\text{pump}} = 1290 \text{ nm}$, $\lambda_{\text{Stokes}} = 1575 \text{ nm}$, $\lambda_{\text{probe}} = 806 \text{ nm}$ and $\text{FWHM}_{\text{pump}} = \text{FWHM}_{\text{Stokes}} = 50 \text{ fs}$; $\text{FWHM}_{\text{pump-Stokes convolution}} = 416 \text{ cm}^{-1}$; $\chi_{NR}^{(3)} = A_j$.

tion profile (see Fig. 15B). Obviously, one can eliminate the NR background by just delaying the probe pulse, as it is done in time-resolved CARS, and get theoretically unlimited signal-to-background ratio. Unfortunately, this approach does not properly optimize the resonant contribution, and one might end up with no detectable signal at all. We suggest the use of the two parameters (the probe pulse duration and its delay) simultaneously to achieve close-to-optimal resonant response with reasonable suppression of the NR background. The actual optimal values of the parameters depend on the Raman line width, the sensitivity of a setup employed, and the relative strength of the resonant and NR susceptibilities. Proper tailoring of the probe pulse can help to reduce the contribution of the NR background for probe delays comparable to its length. For example, rectangular-like spectrum gives a sinc-squared temporal profile, $\sim [\text{Sin}(\Delta\omega t/2)/(\Delta\omega t/2)]^2$, of the probe pulse intensity. Putting the preparation pulses in one of its nodes, as it is shown in Fig. 14G, would result in effective suppression of the NR background.

From the preceding discussion it might be inferred that in order to optimize the acquisition of the CARS signal, one has to compromise between the resolution, signal strength, and the extent of the NR background suppression. On a single-pulse basis, the spectral resolution is usually determined by the probe bandwidth. However, this is not an intrinsic limit. Much better resolution can be achieved by recording the anti-Stokes spectrum while varying the probe pulse delay, granted that the measurements are not overwhelmed by the fluctuations.

C. Experimental implementation

Femtosecond pulses are a natural source of broadband laser radiation. For our experiment we utilize a Ti:Sapphire regenerative amplifier with two evenly pumped

optical parametric amplifiers (OPAs). The output of the first OPA ($\lambda_1 = 712\text{-}742$ nm, tunable; FWHM \sim 12 nm) and a small fraction of the amplifier output ($\lambda_2 = 803$ nm, FWHM \sim 32 nm) are used as pump and Stokes beams, respectively. The output of the second OPA, the probe beam ($\lambda_3 = 578$ nm), is sent through a home-made pulshaper with an adjustable slit (see Fig. 10) that cuts the bandwidth of the pulse. As follows, the Stokes and probe pulses pass through delay stages (DS1, 2) and then all the three beams are focused by a convex 2-inch lens (with the focal length $f = 20$ cm) on the rotated sample. The scattered light is collected with a 2-inch achromatic lens ($f = 10$ cm) and focused onto the entrance slit of the spectrometer with CCD.

In the improved hybrid CARS setup, the three beams from the OPAs are shifted into near-IR region ($\lambda_{\text{pump}} = 1279$ nm, $\lambda_{\text{Stokes}} = 1560$ nm and $\lambda_{\text{Probe}} = 806$ nm) and looser focused, while keeping the other things same. This improvement not only obtains more power output of the OPAs, but also higher threshold for the spores as compared to the visible-range wavelengths. The three beams are focused separately (with the focal lengths for pump, Stokes and pump $f_{\text{pump}}=50$ cm, $f_{\text{Stokes}}=50$ cm and $f_{\text{probe}}=20$ cm respectively) to make them overlapped at the focuses.

D. Experimental results

1. Hybrid CARS on Na_2DPA powder

Na_2DPA powder is an easy-to-make substitute for CaDPA , a marker molecule for bacterial spores accounting for 10% to 17% of their dry weight [45]. The spontaneous Raman spectrum for Na_2DPA [Fig. 16] exhibits a similar set of strong Raman lines as CaDPA and differs from what one would find for dipicolinic acid (DPA) itself [75].

The CARS traces taken on Na_2DPA powder for different pump wavelengths show that the pump wavelength affects the NR background and resonant Raman lines in

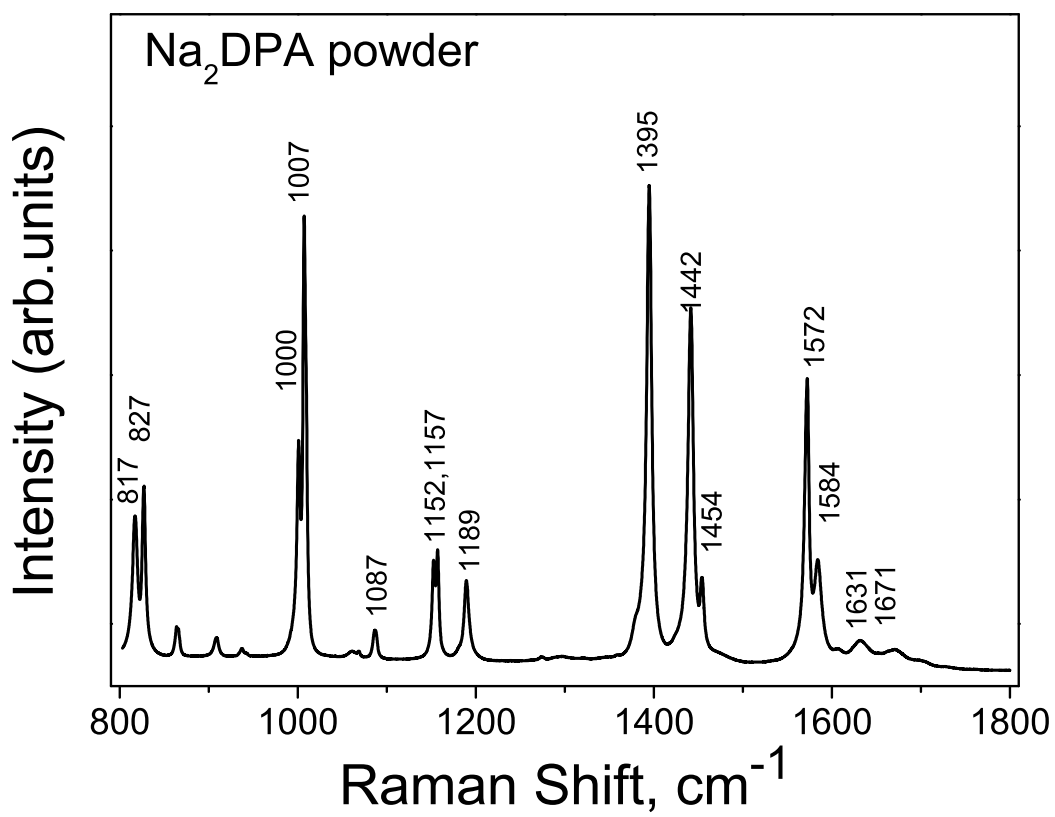


Fig. 16. Na₂DPA spontaneous Raman spectrum excited by 532 nm light.

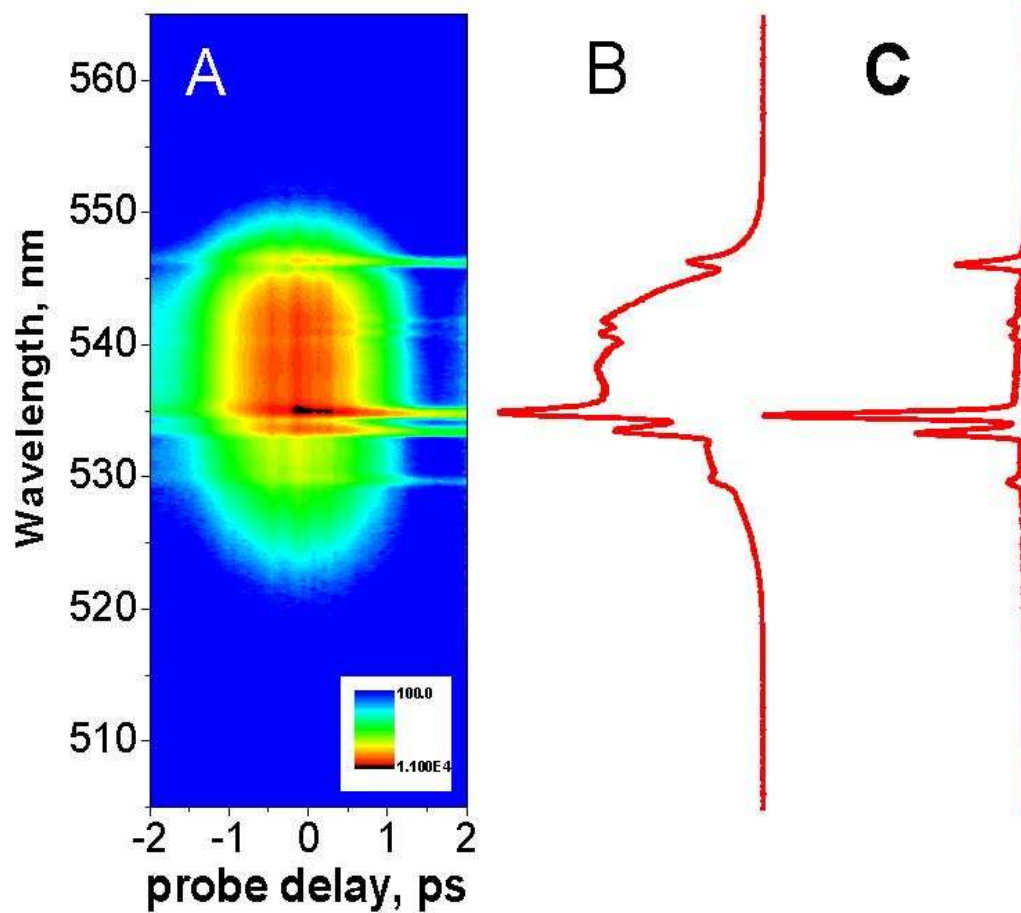


Fig. 17. CARS spectra of Na_2DPA . (A) The CARS trace taken on Na_2DPA powder for pump wavelength 732 nm; (B) the cross-section spectrum of the trace when the probe is not delayed; (C) the cross-section spectrum of the trace when the probe is delayed by 1.5 ps relative to the pump and Stokes pulses. The other parameters are: pump - FWHM ~ 12 nm, 2μ J/pulse; Stokes - 803 nm, FWHM ~ 32 nm, 3.9μ J/pulse; probe - 577.9 nm, FWHM ~ 0.7 nm, 0.5μ J/pulse; Integration time is 1 sec per probe delay step.

different ways [see Ref. [35]]. Streak-like horizontal lines are the signature of excited Na₂DPA Raman transitions while the broadband pedestal is the NR background [Fig. 17]. As expected, the tuning of the pump wavelength spectrally shifts the NR background leaving the position of the resonant lines untouched. Note also that the two contributions exhibit different dependence on the probe delay. The magnitude of the NR background determined by the overlap of the three laser pulses and therefore follows the probe pulse profile. Relatively long decay time of the Raman transitions under consideration favors their long-lasting presence and makes them stand out when the probe is delayed.

The cross-sections of the spectrograms at two different probe delays are given in Figs. 17B, C. One can see that when the three pulses are overlapped, the resonant contribution is severely distorted by the interference with the NR background. Delaying the probe by 1.5 ps, which is close to the node of the probe pulse as in Fig. 14D, improves the signal-to-background ratio by at least an order of magnitude. We infer that the limitation is imposed by multiple scattering. Comparison with the data from spontaneous Raman measurements shows a remarkably good match.

2. Hybrid CARS on *B. subtilis* spores

Extracted CARS contributions from our first measurements on *Bacillus subtilis* spores (a surrogate for anthrax) were taken from the same configuration as that for the Na₂DPA measurement [see Ref. [35]]. However it took minutes to get a strong Raman lines standing out from the background, which is too long for real-time detection. Our recent improvement on the setup by near IR pulses shortens the detection to the order of milliseconds. The longer wavelengths far from the electric transition reduce the possibility of multiplex scattering from organic materials, so make the vibrational Raman signal stand out. Fig. 18A1, shows the CARS trace from the

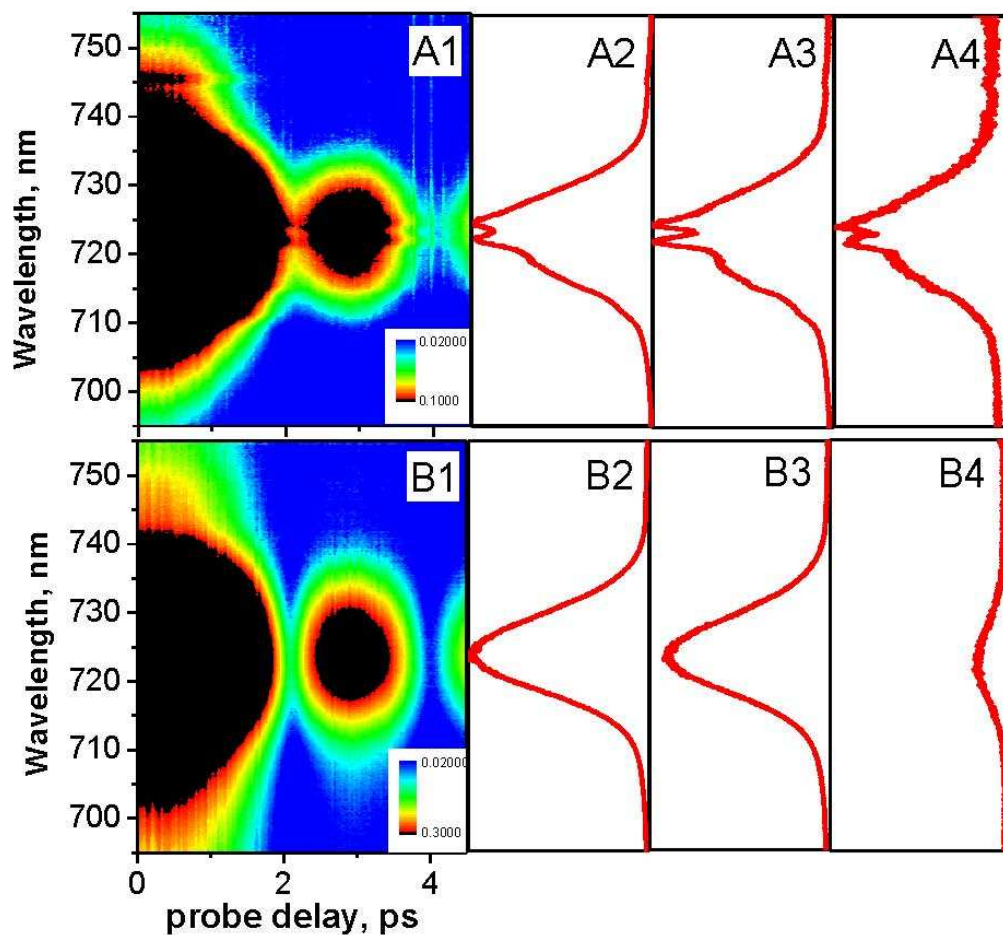


Fig. 18. CARS spectra of *B. subtilis* spores. (A1) The CARS trace taken on *B. subtilis* spores from the near-IR setup; (A2-4) the cross-section spectra of the trace A1 when the probe is not delayed (A2), the probe is delayed by 1.5 ps (A3), and the probe is delayed by 2.1 ps at the node of the probe temporal profile (A4) relative to the pump and Stokes pulses. (B1-4) are similar to (A1-4) on glass sample. The cross-section spectra of glass are rescaled to the spectra of spores at the same probe delay. The other parameters are: pump - 1279 nm, FWHM \sim 12 nm, 10 μ J/pulse; Stokes - 1560 nm, FWHM \sim 24 nm, 10 μ J/pulse; probe - 806 nm, FWHM \sim 1.0 nm, 1.4 μ J/pulse; Integration time is 0.2 sec per probe delay step.

sample of *Bacillus subtilis*. The spectrum is recorded in 0.2 s per probe step. From Fig. 18A2-4, the cross-section spectra at 0 probe delay (A2), 1.5 ps probe delay (A3) and 2.1 ps probe delay (A4, at the node of the probe temporal profile), one can see the sharp Raman lines at 1398 cm^{-1} and 1445 cm^{-1} . The delay of probe improves the signal-to-background ratio of the spores spectra but cannot remove the nonresonant background completely due to the stronger multiplex scattering from organic molecule (Fig. 18A3 and A4). As comparison to confirm this method really works, we also measure the spectra from the glass powder. Fig. 18B1-4 shows only the smooth nonresonant FWM. Near the probe node, the FWM of glass can be suppressed almost completely compared to that of spores.

E. Conclusion

We have demonstrated a hybrid CARS technique that optimizes the probing and acquisition of the generated CARS signal. We reduce the NR background contribution by using a delayed optimally-shaped probe pulse. Furthermore, we employ multi-channel detection and record the full CARS spectrum on a single pulse basis, thereby alleviating the problem of background suppression.

Hybrid CARS measurements on dry Na_2DPA powder demonstrate the utility of the technique. An order of magnitude improvement in signal-to-background ratio, as compared to non-degenerate multiplex CARS arrangement, is readily achieved even in the presence of multiple scattering. The absolute frequencies of the Raman transitions observed in the CARS experiment match to those from spontaneous Raman.

The technique is well suited for detection applications. We show that CARS can be used for bacterial spore detection in the backscattering configuration. From our improved Near-IR experimental setup, strong major Raman lines of *B. subtilis*

in the fingerprint region can be obtained in the order of millisecond, which makes the real-time detection possible. Although these measurements have been done with abundance of spores, further improvements of the detection characteristics are expected.

We note that the present implementation of hybrid CARS is highly versatile. It allows for a compromise between frequency- and time-resolved CARS by simply changing the width of the pulshaper slit. The use of a single femtosecond system with two OPAs obviates the need for synchronization, common to two-laser systems. We have to sacrifice pulse energy in order to obtain a narrowband probe but this sacrifice has a remedy. The use of thicker nonlinear crystals in the OPAs for the frequency conversion process that produces the probe pulse would result in a narrower probe spectrum to start with and therefore higher throughput for the pulshaper.

CHAPTER III

GLUCOSE CONCENTRATION MEASURED BY HYBRID CARS*

A. Introduction

Glucose, usually called blood sugar, is the primary source of energy for the body's cells. Normally, the blood glucose level in human body is maintained below 5.6 mM and higher level causes diabetes disease. Nowadays diabetes is a rapidly growing disease related to failure of blood sugar (glucose) regulation. However the current medical glucose measurement process requires painful fingerpricks and therefore cannot be performed more than a few times a day. Therefore noninvasive glucose diagnosis has received considerable attention. Various techniques such as electrochemical assays [76], optical methods including scattering [77], notably near-infrared absorption [78] and Raman spectroscopy [79], have shown substantial promise. CARS, as a superior technique to conventional Raman spectroscopy, has the capability of selective imaging of glucose with an enhanced signal efficiency and therefore has attracted much interest in biological and biomedical applications, including glucose diagnosis [80]. Our goal is to develop an optical technology for the accurate, non-invasive (painless) and continuous monitoring of blood glucose concentration.

Inelastic scattering of photons by vibrating molecules constitutes the Raman effect, which has become an indispensable tool for analyzing the composition of liquids, gases, and solids [12,81]. Both ordinary Raman spectroscopy and CARS spectroscopy

*Reprinted with permission from "Glucose concentration measured by the hybrid coherent anti-Stokes Raman-scattering technique" by Xi Wang, Aihua Zhang, Miaochan Zhi, Alexei V. Sokolov, and George R. Welch, 2010. *Phys. Rev. A*, vol. 81, pp. 013813, Copyright [2010] by The American Physical Society.

find widespread use in medical diagnostics [17, 82]. While the probability of spontaneous Raman scattering depends on the molecular concentration linearly, for its coherent counterpart - CARS - the signal is known to scale quadratically with the concentration of scatterers due to constructive interference of the resultant coherent photons [12, 81]. In recent work, Dogariu et al. have measured a clear quadratic dependence of the CARS signal in a variety of samples, including highly scattering powders such as dipicolinic acid, calcite, and gypsum [83].

Even though CARS may be far superior to spontaneous Raman when the number of scattering molecules is large, at low concentrations the quadratic dependence of CARS is considered to be a disadvantage. In this chapter we show that under certain conditions the CARS signal can scale linearly with concentration. Motivated by the possibility of non-invasive monitoring of blood glucose levels, we study aqueous glucose solutions and solutions of glucose dissolved in blood. We use a recently developed variant of CARS, termed hybrid CARS [35], which combines broadband pulsed preparation of molecular coherence with frequency-resolved detection via a time-delayed probe, thereby combining the advantages of frequency- and time-resolved spectroscopic techniques [32, 35, 83, 84]. In the way hybrid CARS mitigates the four-wave-mixing background, it shows potential for spectroscopy of highly-scattering media such as human tissue.

Although it is known that a resonant signal interfering with a nonresonant background can produce a linear scaling with concentration [4, 11], we believe this is the first time this effect has been seen with the “hybrid CARS” setup described above. This is important because not only does the setup provide background discrimination, but also signal amplification, and it does so in a way that provides robust detection of several vibrational modes simultaneously. Furthermore, even though numerous background suppression techniques exist, to the best of our knowledge, in the past

the ability to precisely adjust the amplitude and phase of coherent nonresonant background was not used for signal manipulation and amplification. This chapter shows how this can be done in a system of current practical interest.

B. Raman cross-section of glucose

High laser powers and long acquisition times are required due to the inherently small normal Raman scattering cross section of glucose, $5.6 \times 10^{-30} \text{ cm}^2 \text{ molecule}^{-1} \text{ sr}^{-1}$ for the 518 cm^{-1} line according to McCreery and co-workers. As comparison, benzene, a strong Raman scatterer, has a cross section of $2.8 \times 10^{-29} \text{ cm}^2 \text{ molecule}^{-1} \text{ sr}^{-1}$ for the 992 cm^{-1} line and water, a weak Raman scatterer, has a cross section of $1.1 \times 10^{-31} \text{ cm}^2 \text{ molecule}^{-1} \text{ sr}^{-1}$. The reported Raman cross section for glucose is only five times smaller than that of benzene and 50 times larger than that of water. However, their peak Raman cross sections are quite different: $6 \times 10^{-32} \text{ cm}^3 \text{ molecule}^{-1} \text{ sr}^{-1}$ for the glucose 518 cm^{-1} line and $1 \times 10^{-29} \text{ cm}^3 \text{ molecule}^{-1} \text{ sr}^{-1}$ for the benzene 992 cm^{-1} line. The detected signal of benzene as the square of susceptibility will be around five orders stronger than the glucose signal [85, 86].

C. Experimental setup

Figure 12 shows our experimental setup. The pump and Stokes pulses are from the two OPAs and have wavelengths 1290 nm (FWHM 50 nm) and 1510 nm (FWHM 70 nm) respectively. The frequency difference between the pump and Stokes beams is approximately 1100 cm^{-1} , which optimizes the excitation of the strong Raman lines in the glucose solution (see Fig. 19). The probe beam then has a top-hat-like spectrum at 806 nm with width approximately 1.2 nm (15 cm^{-1}). The probe width is chosen to be comparable with the spectral width of the vibrational modes (around

20 cm^{-1} for glucose) for the purpose of multiplex CARS detection as described in Ref. [35].

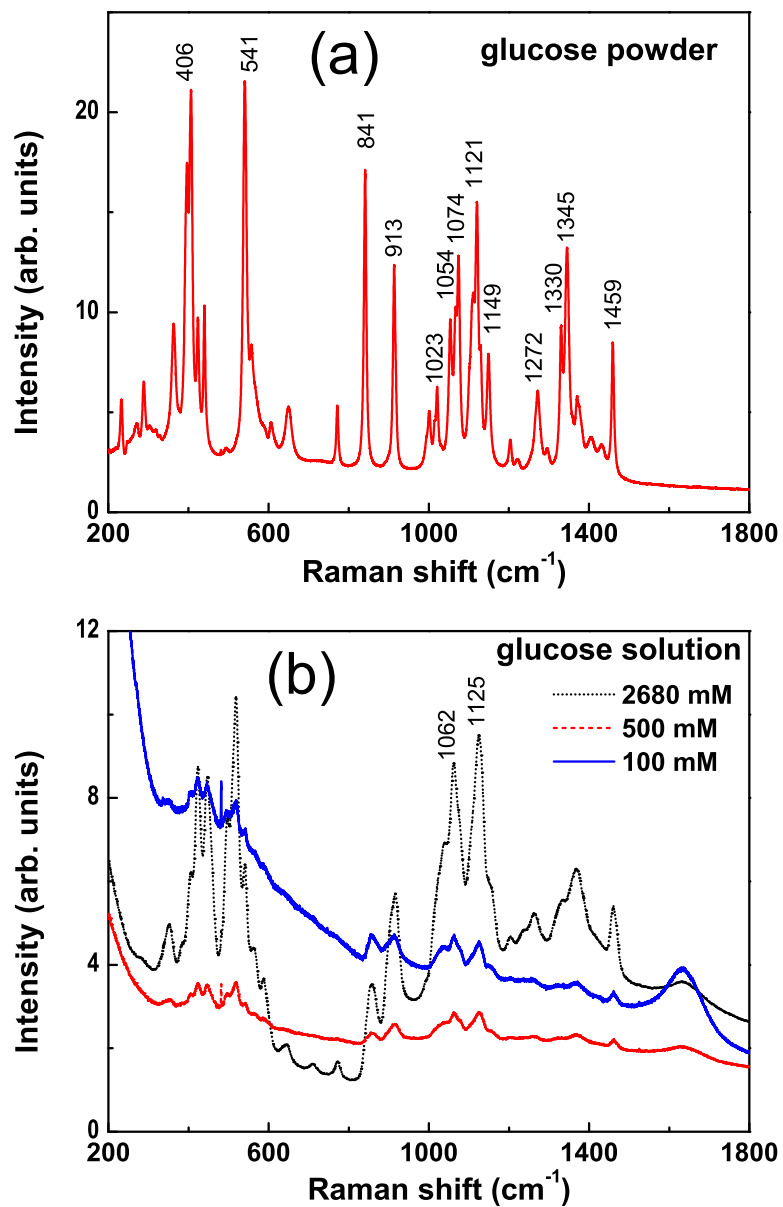


Fig. 19. Spontaneous Raman spectra of D-glucose. (a) is for powder and (b) is for aqueous solutions. Data were taken with a 532 nm laser and different experimental parameters.



Fig. 20. Fused silica cell for the forward CARS (Starna Cells, 21-I-2).

These three pulses have parallel polarization and their time overlap is controlled by two translation stages (DS1 and DS2 in Fig. 12). D-Glucose solution samples are held in a 2 *mm* thick fused silica cell (Fig. 20, Starna Cells, 21-I-2). For the blood samples we use a thinner cell with thickness 1 *mm* for better transmission. The generated CARS signal is collected in a forward geometry and focused onto the CCD. Typical pulse energy is around a few hundred nanojoules to a few microjoules under different focusing conditions. A CCD exposure time of a few hundred ms to a few tens of seconds is used to adapt the signal intensity to the dynamic range of the CCD.

D. Results and discussion

1. Raman spectra

D-glucose was obtained from Sigma-Aldrich with purity greater than 99.5%. It was dissolved in distilled water, producing solutions with concentrations varying from 0.02 *mM* to 2680 *mM* (which is slightly below saturation). The D-glucose solutions

were prepared a few days before the measurements, in order to reach the anomeric equilibrium. Fig. 19 shows Raman spectra from glucose powder and solutions. Due to changes of the anomeric effect and the intramolecular hydrogen bonds [87], the Raman spectra of the D-glucose aqueous solution in Fig. 19(b) are different from that of glucose powder in Fig. 19(a). The D-glucose solution shows two strong and broad Raman lines near 1100 cm^{-1} with spectral FWHM around 20 cm^{-1} , while the other Raman lines at around 850 cm^{-1} and 1350 cm^{-1} are suppressed. We also observe the Raman peaks from water [88]: a narrow line at 1630 cm^{-1} , a strong line below 200 cm^{-1} and a broad line at 500 cm^{-1} , all of which are comparable with those from glucose. This leads us to choose a frequency difference (pump-Stokes) for our CARS measurements of approximately 1100 cm^{-1} to coherently excite the stronger Raman lines of glucose while avoiding the background from water.

2. Probe bandwidth

Figure 21 shows how our setup works for the glucose aqueous solution with a concentration of 2680 mM . Figure 21(a) demonstrates the effect of probe bandwidth at zero probe delay - that is, when the pump and Stokes pulses overlap the peak of the probe pulse. When the probe bandwidth is narrower than that of the glucose modes (around 20 cm^{-1}), we can see the fine features of multiple Raman peaks. This is seen in the dashed and solid (black and red in the color version online) curves for probe

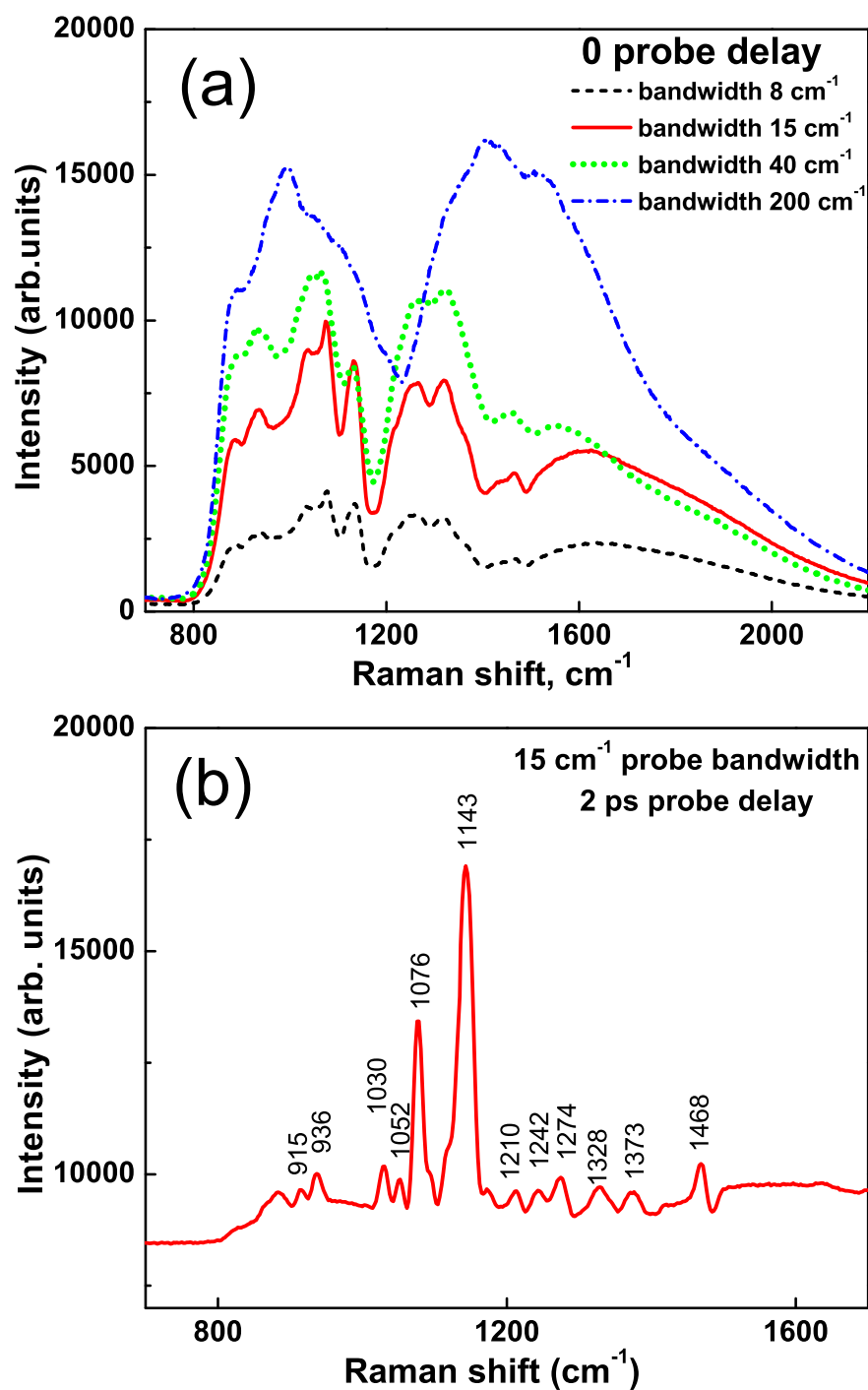


Fig. 21. CARS spectra of D-glucose solution at 2680 mM . (a) Spectra at 0 probe delay with different probe bandwidths and the same power; (b) background suppression when probe is delayed to the node; note that the background level is still around 9000 units. Here the integration time is 0.2 second.

band-width of 8 and 15 cm^{-1} respectively. The resolutions of the Raman lines in these two curves are almost the same. If the probe spectrum is broader, the details of the peaks are obscured, as seen in the dotted and dash-dotted (green and blue) curves with probe bandwidth of 40 and 200 cm^{-1} respectively. In Fig. 21(b), when the probe is delayed so that its first node overlaps the Stokes and pump pulses, multiple Raman lines stand out against a weak background, in contrast to the solid (red) curve in Fig. 21(a) where the background dominates. However the background suppression is only partial. Even for the strongest peaks in Fig. 21b, the background is still greater than the signal. The CCD integration time for these spectra is 0.2 s, and the recorded spectral range was approximately 1000 cm^{-1} .

Experimentally we find that the measurement is optimized when the probe bandwidth is comparable to the spectral width of the vibrational modes. Under these conditions, the first node of probe pulse shape (for 15 cm^{-1} bandwidth) is at 2 ps , while the decay time of glucose modes derived from the spontaneous spectrum in Fig. 19(b) is around 1 ps .

3. Concentration dependence

We have measured CARS signal as a function of glucose concentration in aqueous solution in Fig. 22. In these measurements, we delay the probe pulse until its first temporal node overlaps the pump and Stokes pulses. We calculate the intensity of a CARS peak by area integration. In Fig. 23(a), Raman lines at 1143 cm^{-1} and 1076 cm^{-1} both show a linear dependence of the signal intensity on the glucose concentration below 1000 mM , with a slope around 1.02 in the log-log scale. In Fig. 23(b) at another probe delay (1.83 ps) the linear fits with slope 0.98 and 0.95 confirm the linear dependence. This dependence is in sharp contrast to the quadratic dependence obtained by other groups [5].

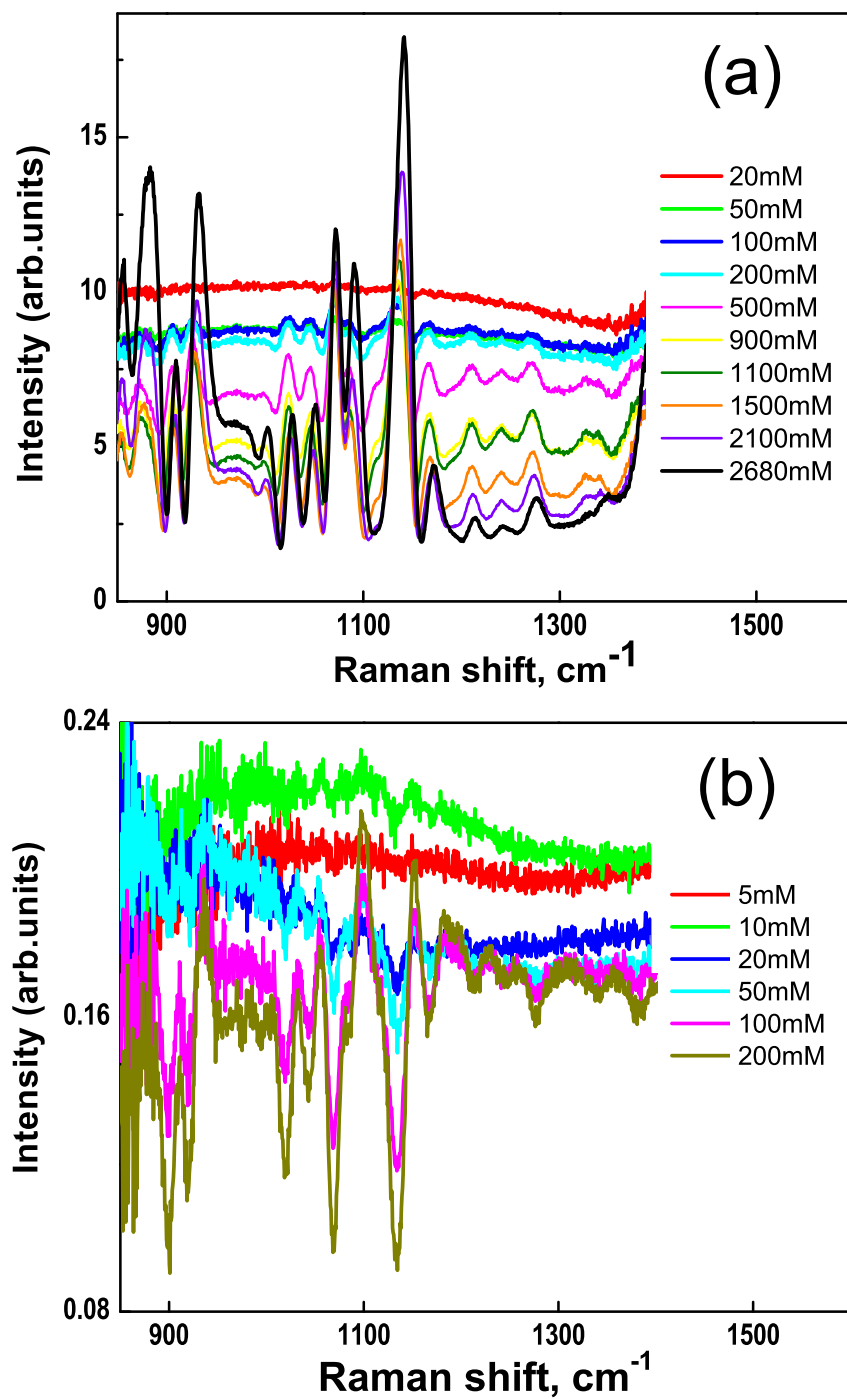


Fig. 22. CARS spectra of D-glucose solution with different concentrations. (a) is at 2.00 ps and (b) is at 1.87 ps probe delay.

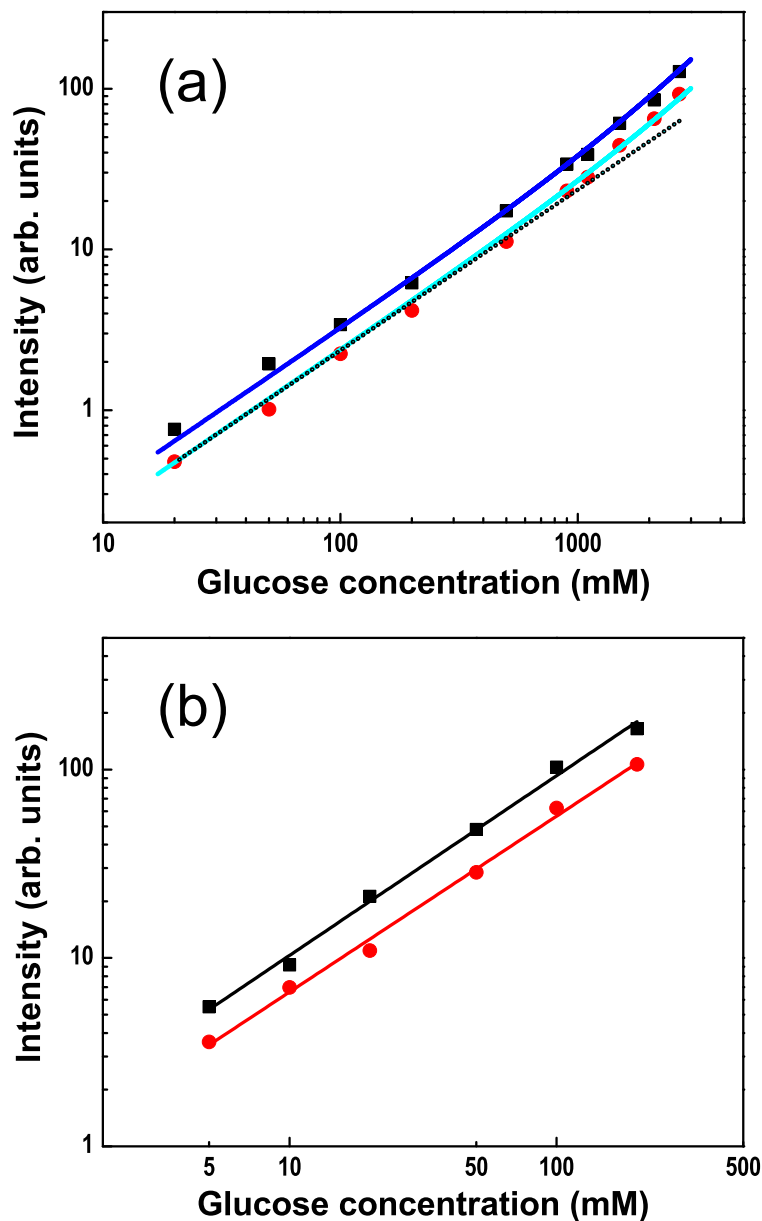


Fig. 23. Nearly linear dependence of CARS signal intensity on D-glucose concentration. (a) is at 2.00 ps probe delay; (b) at is 1.87 ps probe delay. Square and round dots are experimental data of the Raman lines at 1143 cm^{-1} and 1076 cm^{-1} respectively. In (a), the solid curves are second-order polynomial fits, and the dotted line has a slope 1. In (b), the best power-law fits have slopes of 0.98 (± 0.03) and 0.95 (± 0.03) for the square and round dots respectively.

As we can see from Eqs.(1.7 and 1.10), when the background is suppressed with $P_B^{(3)} = 0$, then we have $I_{CARS}(\omega) \propto |P_R^{(3)}(\omega)|^2 \propto N^2$. The linear dependence on N observed here thus indicates incomplete suppression of the background. If the residual background is comparable to or larger than the signal of interest ($P_B^{(3)} \geq P_R^{(3)}$), then a heterodyne-like product $I_{CARS}(\omega) \propto 2Re(P_B^{(3)}P_R^{(3)}(\omega)) \propto N$ dominates the weaker resonant signal from glucose. (In our case, this background may be due to a far-detuned CARS signal from water. This is supported by noting that the spontaneous Raman spectrum of glucose solutions in Fig. 19 show that the wing of the broad Raman line from water at 500 cm^{-1} crosses the spectral region studied here around 1100 cm^{-1} .) To be more precise, when both contributions are taken into account, we can use a second-order polynomial function $I_{CARS} = 2E_BE_R(N = 1\text{ mM})N + (E_R(N = 1\text{ mM})N)^2$ to fit the experimental data, where E_B is the background electric field magnitude, $E_R(N = 1\text{ mM})$ is the Raman-resonant electric field contribution per 1 mM of glucose, and N is the glucose concentration measured in mM. For the two curves (corresponding to the two Raman lines at 1143 cm^{-1} and 1076 cm^{-1}) the fitting parameter E_B is taken to be the same, thus constricting the fit. For the two fitting curves, the ratio of the two best-fitting parameters $E_R(N = 1\text{ mM})$ is found to be equal to 1.36, which is consistent with the observed spectra (Fig. 21(b)). We can see that the two curves deviate from the dotted line with a slope of 1 at high glucose concentrations (above 1000 mM). Here we would like to mention that in a different experiment with an all-collinear beam configuration, using the same sample cell and the same set of wavelengths, we also obtain a linear dependence of the CARS signal on glucose concentration. We conclude that it is the heterodyne effect mentioned above that gives rise to the linear concentration dependence of the measured signal, and not some sort of loss of optical field coherence. This effect may be beneficial for detection of species at low concentration.

Quite remarkably, when we reduce the probe pulse delay such that the background is somewhat increased (and CARS is stronger too), we obtain an overall better performance and are able to reliably detect glucose at lower concentrations. This is demonstrated in Fig. 23(b), which shows the CARS signal from the 1067 cm^{-1} and 1143 cm^{-1} lines (similar to those seen in Fig. 23(a)) for a somewhat optimized probe pulse delay and a lower range of concentration. These data show that the hybrid CARS technique is useful for optimizing (and not only maximizing) the signal-to-background ratio, and allows us to take full advantage of the aforementioned heterodyne amplification. Although increasing the background even more would introduce extra noise, we can detect glucose signals down to 5 mM concentration, which is medically relevant and demonstrates the power of this technique.

4. Glucose measurement in blood

We have also measured CARS signals from glucose dissolved in pig blood. Fig. 24 shows several spectra in the region of interest for different concentrations of glucose. It is apparent that the strong glucose lines seen in aqueous solution are still present, but that other features are also present that were not seen in aqueous solution. For the data shown in Fig. 24, the samples of pig blood were prepared by adding different volumes of highly concentrated glucose solution into a fixed volume of pig blood. In Fig. 24(a), the signal intensity at 1015 cm^{-1} decreases as more glucose solution is added, while the glucose lines previously observed increase. Furthermore, this line disappears in a pure glucose solution. This shows that the constituent corresponding to the Raman line at 1015 cm^{-1} is diluted more when more glucose solution is added, and the linear decrease of the intensity of this Raman line on the volume of glucose solution (see Fig. 24(b)) shows that this constituent corresponds to a component in blood, not water or glucose. This allows us to use this Raman line as a reference.

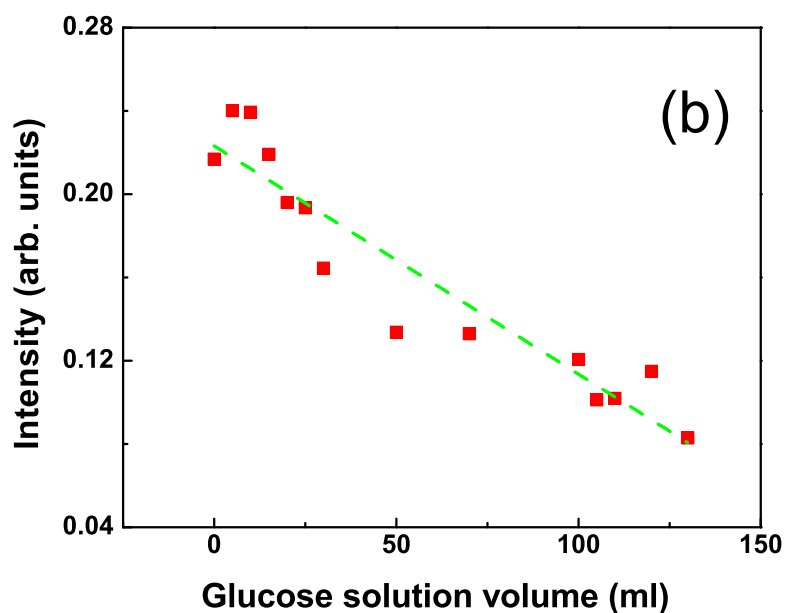
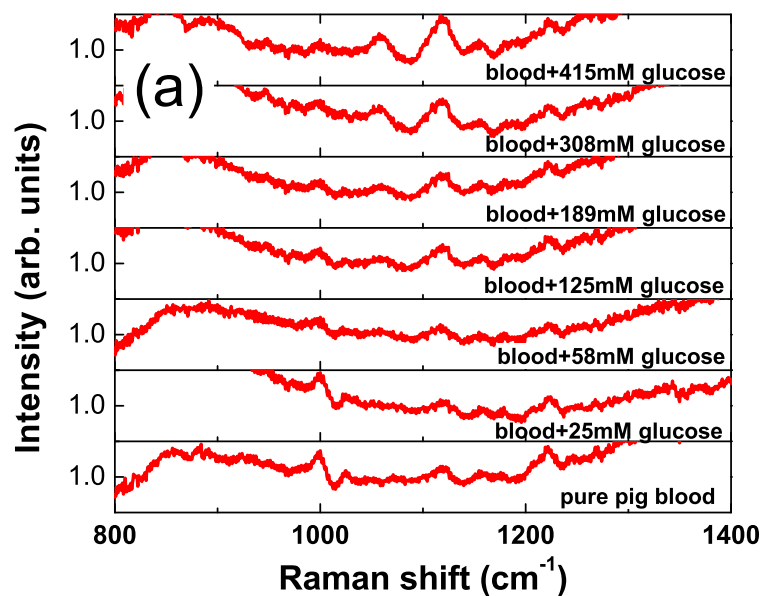


Fig. 24. CARS spectra of pig blood. (a) The mixtures were obtained by adding different volumes of glucose solution into blood with fixed volume. In each case, the ordinate scale is from 0.8 to 1.2. (b) Linear decrease of the reference signal at 1015 cm^{-1} on the glucose volumes added into blood in (a).

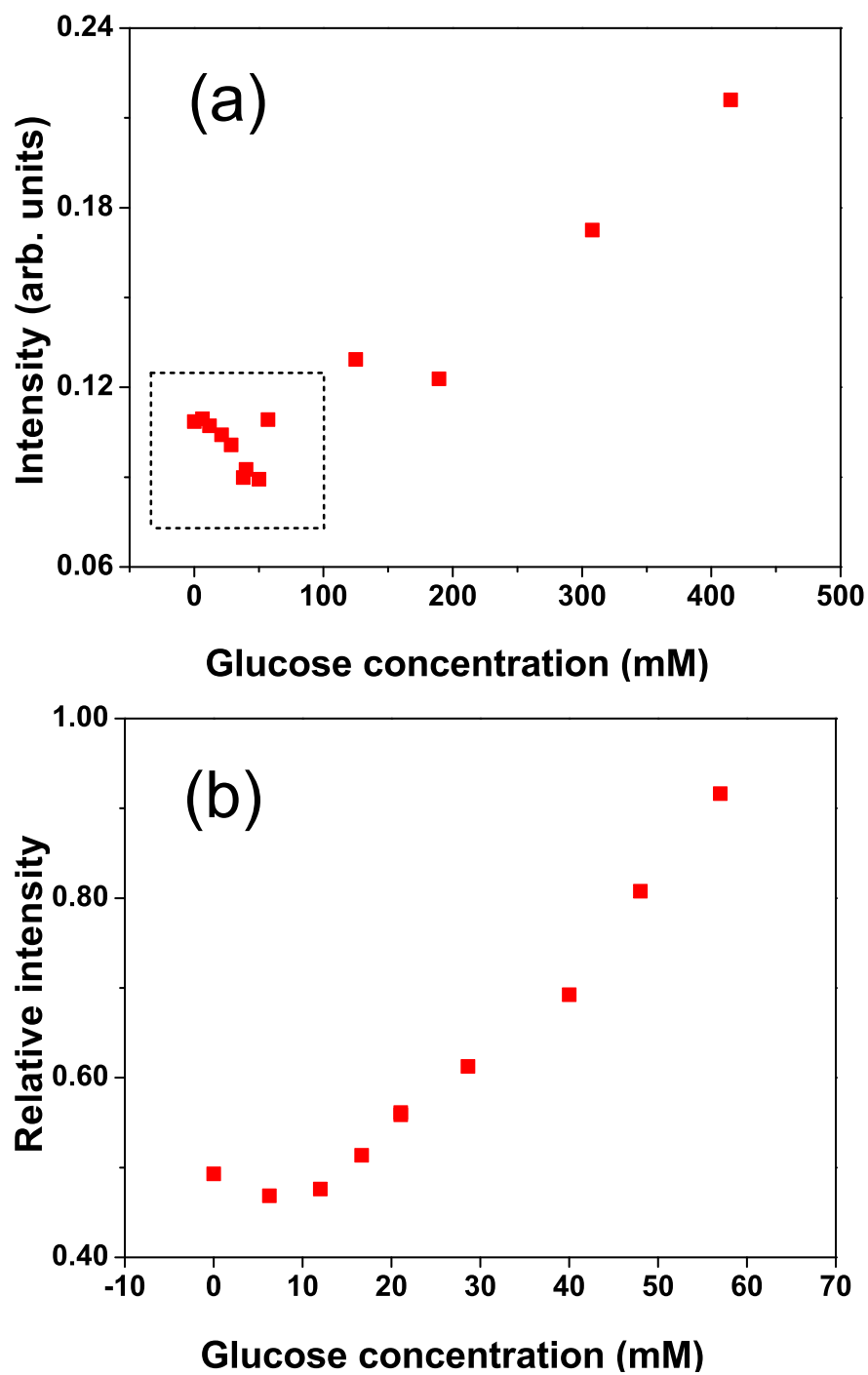


Fig. 25. Glucose concentration dependence in pig blood. (a) CARS signal from 1143 cm^{-1} . We observe an approximately linear dependence with concentration. The noise at low concentration is due to laser intensity fluctuation. (b) Ratio of glucose CARS signal at 1143 cm^{-1} to reference line from blood for the boxed area in (a).

That is, we can measure the ratio of the height of a glucose line to this peak, in order to help eliminate distortion arising from laser intensity fluctuations. Furthermore, we note that we can see the reference signal and the weak CARS signals from glucose even in pure blood.

Figure 25 shows the CARS signal from 1143 cm^{-1} glucose line in blood. In Fig. 25(a), the intensity is nearly linearly dependent on the glucose concentration, but fluctuations are seen at low concentration. Fig. 25(b) shows the ratio of this glucose peak to the reference peak. This ratio increases along a smooth curve (nearly a line) when the glucose concentration goes up. We can clearly distinguish the glucose concentrations over 10 mM . The flattening of this curve at low concentration may be due to the naturally occurring glucose in the pig blood that was used. Thus with the aid from the reference signal, the measurement sensitivity is highly enhanced. Although better sensitivity is still needed for practical applications, our method shows promise for low concentration detection.

5. Phase changes in CARS signals

We have observed an interesting phenomenon: the phase of the generated CARS field changes when we delay the probe pulse, as shown in Fig. 26. Figure 26(a) shows the temporal profile of the probe pulse, as measured through four-wave mixing (FWM) in water with pump and Stokes pulses. For these data, the first node occurs 2.0 ps after the peak of the probe pulse. When this node coincides with the arrival of the pump and Stokes pulses, the resultant anti-Stokes spectrum is dominated by the Raman lines of glucose and is nearly background-free (for high glucose concentrations), as shown in Fig. 21(b). When the first node of the probe pulse comes before the pump and Stokes pulses, the spectrum shows Raman lines with dip structures, as seen in the dotted (blue in color) curve in Fig. 26(b). When the delay is greater than 2.0 ps ,

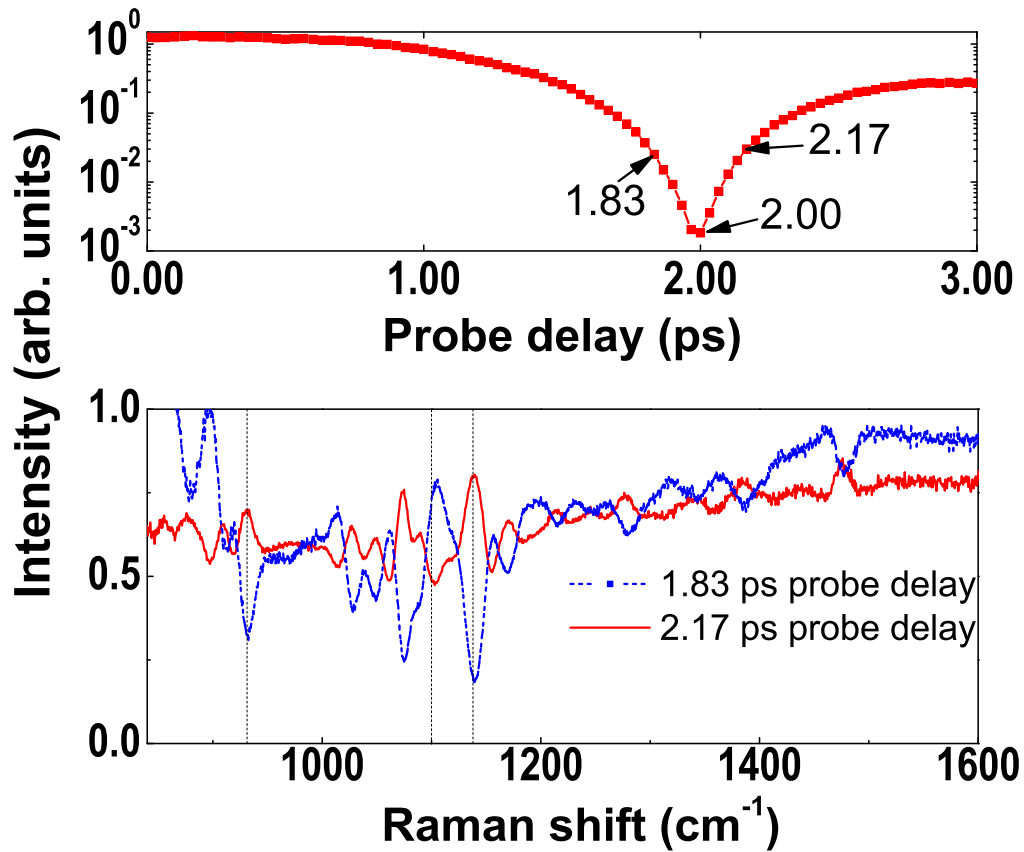


Fig. 26. Phase dependence of the glucose CARS spectra on probe delay. (a) Temporal profile of the probe beam, as measured through FWM in water with pump and Stokes pulses; (b) CARS spectra of 500 *mM* glucose solution at 1.83 *ps* and 2.17 *ps* probe delays.

peaks are seen, as in the solid (red) curve in Fig. 26(b). We attribute this phase change to fact that the probe field changes phase as it goes through a node, similar to the Gouy phase shift of an electro-magnetic field propagating through a focus. Real world applications based on this type of delayed pulse scheme will have to accurately account for this effect in order to model the CARS lineshapes.

we need to mention that for the pure glucose solution measurement, the three incident laser beams overlap at their focuses in a crossing-beam configuration (for Figs. 21-23, and 26) as in Fig. 12; while for the blood measurement, the beams overlap

in a collinear configuration (for Figs. 24-25). In our case, these two configurations produce similar results and detection sensitivity.

E. Conclusion

In this chapter, we demonstrate the application of a hybrid CARS technique to highly-precise, non-invasive glucose detection. We obtained CARS spectra from both pure glucose solutions and from blood samples. We find a linear dependence of the CARS signal on the glucose concentrations due to interference between the resonant signal and the broad off-resonant background from water. Our method is reliably capable of measuring glucose samples with concentration as low as 5 *mM*. Furthermore, our method is also optimized for multiplex CARS and thus allows chemical specifications. We have demonstrated how interference between signal and background gives rise to a linear dependence of signal on concentration, and we have shown how the phase of the probe field affects this. In our experiment the background amplitude was adjusted by variable probe pulse delay and the background phase is varied due to the Gouy-like phase change around the temporal node of the probe field. Even though in this experiment the amplitude and phase were not varied independently, in principle their independent control is possible, though slightly more elaborate probe pulse shaping. Therefore, this work shows how essentially the full range of heterodyne CARS capabilities can be achieved in a simple configuration (not involving an interferometer) where the fully-controllable local oscillator (background) field is obtained from the same sample.

CHAPTER IV

HETERODYNE CARS FOR SPECTRAL PHASE RETRIEVAL AND SIGNAL
AMPLIFICATION*

A. Introduction to interferometric CARS

In this chapter we describe an experiment which allows us to investigate interference in CARS with most flexibility. We have built a simple and effective CARS interferometer reminiscent of previous heterodyne schemes [63–65, 69, 70], where the relative phase of the signal and local oscillator fields is adjusted to achieve constructive interference with either the real (in-phase) or imaginary (out of phase) part of the sample’s response. We can therefore directly observe the real and imaginary components of the third-order nonlinear susceptibility ($\chi^{(3)}$) of the sample. Unlike previous heterodyne schemes, we use broad-band femtosecond preparatory pulses and a narrow-band probe pulse to coherently excite multiple Raman lines simultaneously [35]. In addition, we demonstrate that this heterodyne method can be used to amplify the signal. We also show that the combination of the spectral interferometry and phase scan reveals how the background resonance affects the detected susceptibility $\chi^{(3)}(\omega)$ in aqueous methanol solution. Our work has important applications to Raman microscopy and spectroscopy. It also connects with the field of multidimensional spectroscopy in the infrared and visible where heterodyne detected four wave mixing and phase cycling are heavily used [89, 90].

*Reprinted with permission from “Heterodyne coherent anti-Stokes Raman scattering for spectral phase retrieval and signal amplification” by Xi Wang, Aihua Zhang, Miaochan Zhi, Alexei V. Sokolov, George R. Welch, and Marlan O. Scully, 2006. *Opt. Lett.*, vol. 35, pp. 721, Copyright [2010] by The Optical Society of America.

Recently, spectral interferometry [63–65, 69, 70] has been proposed where the CARS field is mixed with an external nonresonant reference field we refer to as the local oscillator (LO). The cases where the nonresonant background is present have also been discussed [63–65, 69, 70]. Following Eqs. 1.7 and 1.10, more generally, without assuming that the background is purely nonresonant, the signal would be expressed as

$$\begin{aligned} S(\omega) &\propto \left| P_{\text{CARS}}^{(3)} + e^{i\phi} P_{\text{LO}}^{(3)} \right|^2 \\ &\propto \left| P_{\text{LO}}^{(3)} \right|^2 + \left| P_{\text{CARS}}^{(3)} \right|^2 + 2\text{Re} \left[e^{i\phi} P_{\text{LO}}^{(3)}(\omega) P_{\text{CARS}}^{(3)*}(\omega) \right] \end{aligned} \quad (4.1)$$

Since

$$\begin{aligned} P_{\text{CARS}}^{(3)} &= P_{\text{B}}^{(3)}(\omega) + P_{\text{R}}^{(3)}(\omega) \\ &= \text{Re} \left(P_{\text{B}}^{(3)} \right) + \text{Re} \left(P_{\text{R}}^{(3)} \right) + i \left[\text{Im} \left(P_{\text{B}}^{(3)} \right) + \text{Im} \left(P_{\text{R}}^{(3)} \right) \right], \end{aligned} \quad (4.2)$$

the heterodyne term becomes

$$\begin{aligned} 2\text{Re} \left[e^{i\phi} P_{\text{LO}}^{(3)} P_{\text{CARS}}^{(3)*} \right] &= 2P_{\text{LO}}^{(3)} \text{Re} \left[e^{i\phi} P_{\text{CARS}}^{(3)*} \right] \\ &= 2P_{\text{LO}}^{(3)} \text{Re} \left\{ (\cos\phi + i\sin\phi) \left[\text{Re}(P_{\text{B}}^{(3)}) + \text{Re}(P_{\text{R}}^{(3)}) - i \left(\text{Im}(P_{\text{B}}^{(3)}) + \text{Im}(P_{\text{R}}^{(3)}) \right) \right] \right\} \\ &= 2P_{\text{LO}}^{(3)} \left[\left(\text{Re}(P_{\text{B}}^{(3)}) + \text{Re}(P_{\text{R}}^{(3)}) \right) \cos\phi + \left(\text{Im}(P_{\text{B}}^{(3)}) + \text{Im}(P_{\text{R}}^{(3)}) \right) \sin\phi \right] \end{aligned} \quad (4.3)$$

and the interference is then:

$$\begin{aligned} S(\omega) &\propto \left| P_{\text{LO}}^{(3)} \right|^2 + \left| P_{\text{CARS}}^{(3)} \right|^2 \\ &+ 2P_{\text{LO}}^{(3)}(\omega) \left[\text{Re} \left(P_{\text{B}}^{(3)}(\omega) + P_{\text{R}}^{(3)}(\omega) \right) \cos\phi + \text{Im} \left(P_{\text{B}}^{(3)}(\omega) + P_{\text{R}}^{(3)}(\omega) \right) \sin\phi \right], \end{aligned} \quad (4.4)$$

When the probe linewidth is not greater than the Raman linewidth, we can write

$P_B^{(3)} \propto \chi_B^{(3)} E_p E_S E_{p^*} \propto \chi_B^{(3)} E_{EX}$ and $P_R^{(3)} \propto \chi_R^{(3)} E_{EX}$. Eq. (4.4) can be written as

$$\begin{aligned}
 S(\omega) \propto & \left| P_{LO}^{(3)} \right|^2 + \left| P_{CARS}^{(3)} \right|^2 \\
 & + 2P_{LO}^{(3)}(\omega) E_{EX} \left[\text{Re} \left(\chi_B^{(3)}(\omega) + \chi_R^{(3)}(\omega) \right) \cos \phi + \text{Im} \left(\chi_B^{(3)}(\omega) + \chi_R^{(3)}(\omega) \right) \sin \phi \right],
 \end{aligned}
 \tag{4.5}$$

where ϕ is the phase difference between the LO and CARS fields. The first two terms are the homodyne intensities and can be subtracted from the signal. The third term is the heterodyne signal which is sensitive to ϕ . Since the background level is often nearly constant, choosing $\phi = \pm\pi/2$ allows the extraction of the imaginary part of the Raman susceptibility, which can be directly compared with spontaneous Raman spectra. Clearly, the heterodyne signal depends on the concentration linearly and the imaginary part can be amplified significantly by the LO field.

B. Experimental setup

The experimental setup is shown in Fig. 27. The pump, Stokes and probe are femtosecond pulses from two optical parametric amplifiers pumped at 1 kHz repetition rate. The pump beam is at 1250 nm (FWHM 50 nm) and the Stokes is at 1435 nm (FWHM 70 nm). For the purpose of multiplex CARS detection, the probe is narrow-band with a top-hat spectrum at 798 nm (width 2 nm) as in [35]. With all-parallel polarization and overlap in time, the three beams are collinearly combined and sent into the interferometer. The beams in both the signal and LO branches are focused with 10 cm lenses and collected with 5 cm focusing lenses. The LO sample is a 100 μm thick glass slide, which provides a clean and broad nonresonant spectrum in the range of interest. A 50% by volume methanol solution is held in a 2 mm thick fused silica

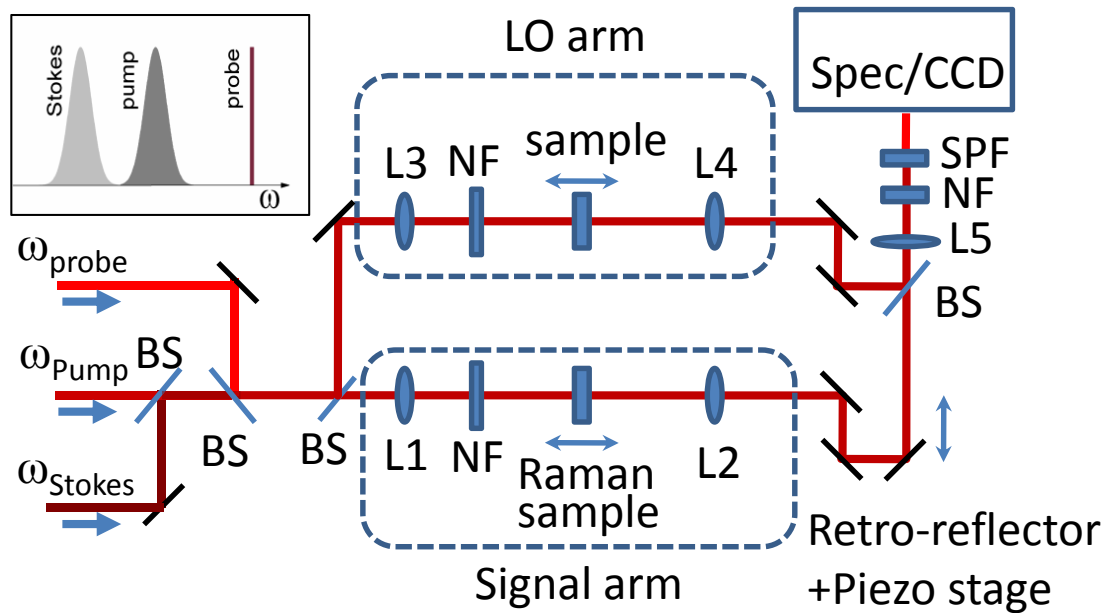


Fig. 27. Schematic of the CARS spectral interferometer. BS, beam splitter; L1-5, lenses; NF, neutral density filter; SPF, shortwave-pass filter; Spec, grating spectrometer. Inset, the spectral ranges and profiles of the pump, Stokes and probe beams in the experiment.

cell. Typical pulse energy in each pulse is a few hundred micro-joules. The generated CARS and LO fields are collinearly sent to a spectrometer with a charge-coupled device (CCD) detector. A piezo stage with 20 nm resolution is employed in the signal branch to change the time-delay and phase difference between the LO and CARS signal. A CCD exposure time of 200 ms is used for all spectra.

C. Interferometric FWM spectra from glass

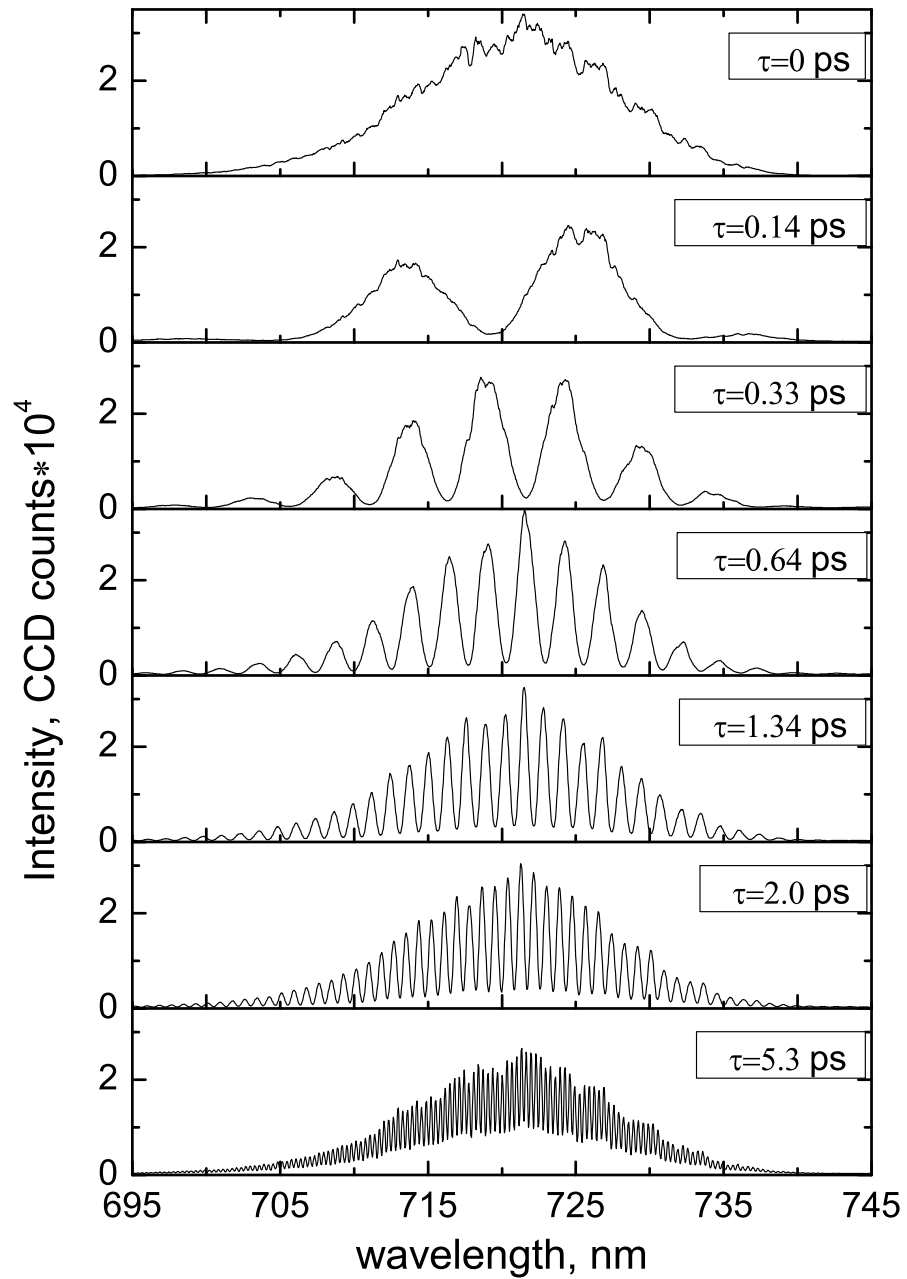


Fig. 28. Interference spectra at different time delays τ between the local oscillator and the signal fields. Both fields are FWM generated through glass slides.

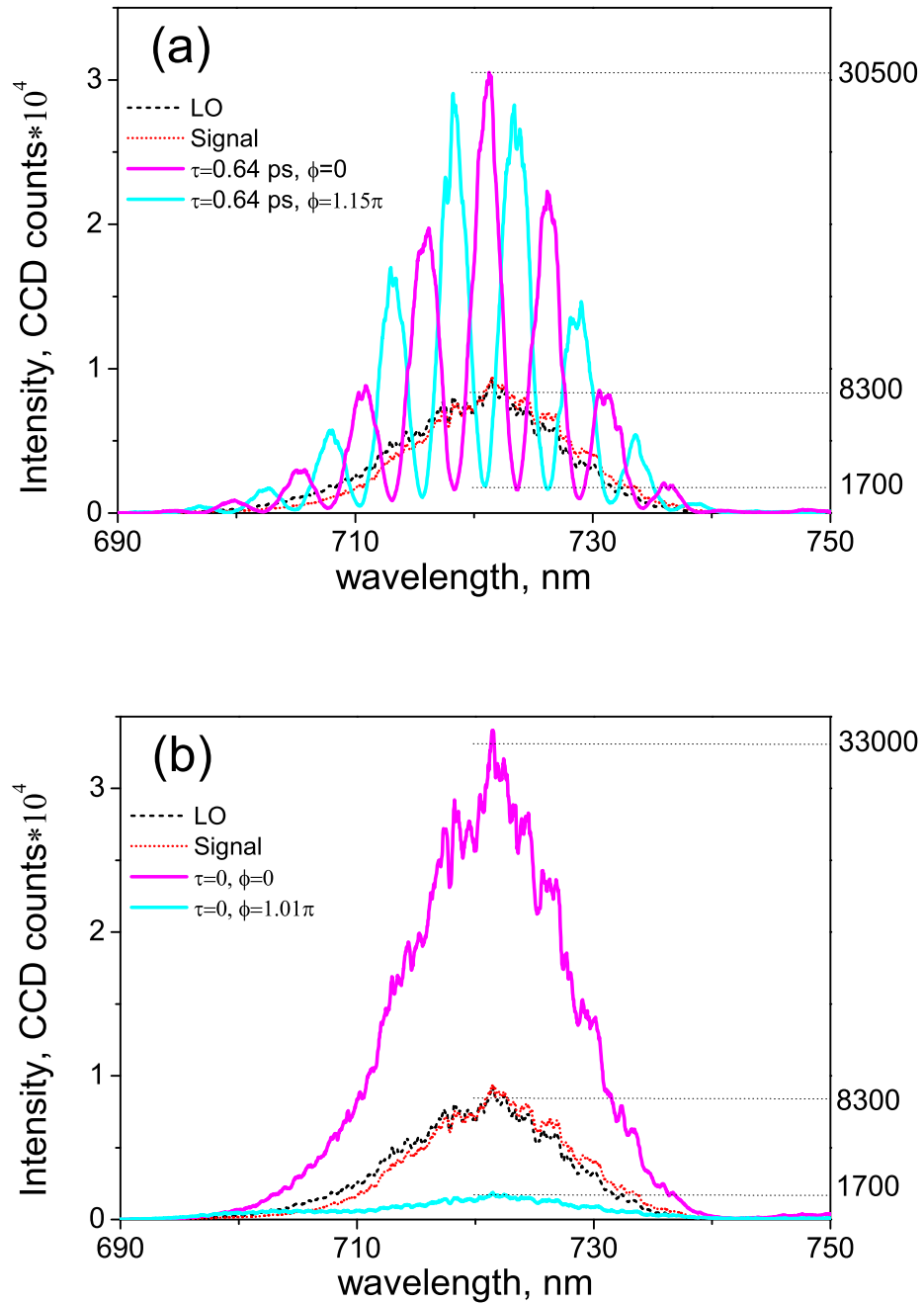


Fig. 29. Interference spectra of nonresonant signals with different phases. Continued from Fig. 28. (a) Interference spectra at $\tau = 0.64$ ps. The interference fringes shift when the relative phase ϕ between the LO and signal fields changes. (b) Constructive ($\phi = 0$ ps, magenta) and destructive ($\phi = 0.52$ ps, cyan) interference at $\tau = 0$ ps.

First we would like to demonstrate how the interferometer works through the interference spectra while both of the LO and signal fields are generated from 100 μm thick glass slides. The glass provides a clean and broad nonresonant spectrum in the range of interest (700 – 2000 cm^{-2}). In Fig. 28, we record the interference spectra at different time delay τ between the LO and signal fields, which are actually two pulses. Here the pump and Stokes wavelengths are around 1240 nm and 1490 nm, respectively. When the two pulses are getting closer in time domain, the interference fringes in spectral domain become sparser and we can estimate the time difference τ from the fringe period. When $\tau = 0$, the fringes merge into one broad spectrum (the top figure).

By adjusting the piezo stage, we can control the precise phase difference ϕ between the LO and signal fields and obtain the spectra in Fig. 29. In Fig. 29(a), the LO and signal fields are apart, the fringes shift when ϕ changes from 0 (magenta) to 1.15π (cyan). Note that we only measure relative phase, and here we just roughly define the origin of the phase scale. In Fig. 29(b), constructive (magenta) and destructive (cyan) interference happens when ϕ changes from 0 (magenta) to 1.01π (cyan). In both cases, the maximum intensity is almost 20 times the minimum one (33000 vs. 1700) and 4 times the LO or signal. These results are close to expectation, which proves the phase adjustment in this interferometer is fairly precise. Please also note that the spectra shown in Figs. 28, 29 are original signals from CCD. The irregular fringes are due to etaloning generated by the CCD itself (see [20]). The spectra in the following parts have been processed to remove the etaloning.

To achieve heterodyne amplification, we choose the LO field to be much stronger than the CARS field from the signal arm within our CCD saturation limit, with intensities of 40000 and 1000 counts, respectively. Figures. 30a and 30b show the measured and calculated interferometric spectra for the methanol solution. In the

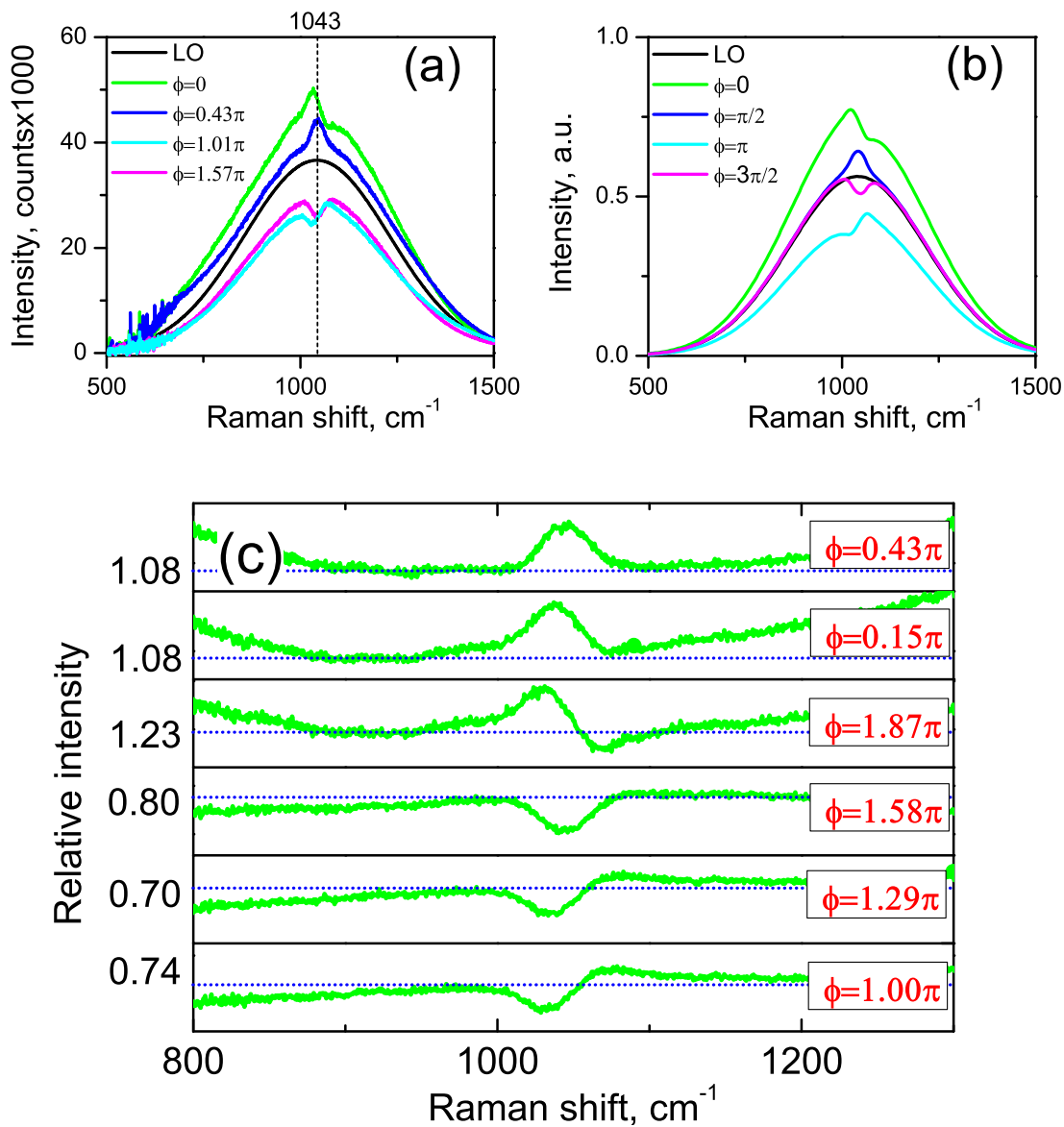


Fig. 30. Interferometric spectra of aqueous methanol solution at different phases ϕ between the LO and signal arms. (a) is experimental and (b) is calculated interferometric spectra. In (c), spectra are rescaled as $S(\omega)/S_{\text{LO}}(\omega)$; the values at left sides correspond to the dotted horizontal lines in each case.

calculation, we use Eq.(4.4) and assume a (complex) Lorentzian lineshape for $\chi_R^{(3)}$ and, for the sake of our argument below, we take $\text{Im}(\chi_B^{(3)}) = 0$. The broad structure results from the broad linewidth of the pump and Stokes pulses, and the narrow feature results from the narrowband probe beam. Although we excite a single vibrational mode in methanol, this technique allows multiplex CARS detection in an FWHM range over 400 cm^{-1} .

D. Interferometric CARS spectra from methanol

1. Phase change in the CARS spectra

In Fig. 30c, the interferometric spectra recorded as $S(\omega)/S_{\text{LO}}(\omega)$ show how the Raman line of methanol at 1038 cm^{-1} depends on the phase ϕ . Since water does not produce any narrow features in this part of the Raman spectrum [88, 91], $\chi_B^{(3)}$ is insensitive to frequency. Therefore here the background from water will not affect the Raman line shape of methanol even if we assume water has an imaginary component of susceptibility in this range. When ϕ is nominally equal to 0.5π (measured as $\phi = 0.43\pi$, within the uncertainty of the piezo stage), the symmetric peak represents an example of extracted $\text{Im}(\chi_B^{(3)}(\omega))$. At $\phi = 1.5\pi$ (measured as $\phi = 1.58\pi$), the Raman line is reversed into a dip structure, which is as expected from the theory. At other phase differences such as $\phi = 0.15\pi$ and $\phi = 1.29\pi$, $\text{Re}(\chi_R^{(3)}(\omega))$ makes a substantial contribution and results in distorted line shapes. At $\phi = 1.0\pi$ and $\phi = 2.0\pi$ (measured as $\phi = 1.87\pi$) where $\text{Im}(\chi_B^{(3)}(\omega) + \chi_R^{(3)}(\omega))$ disappears, we could isolate $\text{Re}(\chi_R^{(3)}(\omega))$. These data are consistent and repeatable during our measurements. Note that we only measure relative phase, and the origin of our phase scale has been properly adjusted.

At the positions which are far from the resonant line of methanol, such as

900.6 and 1200.8 cm^{-1} (roughly the half-maximum points of $S_{\text{LO}}(\omega)$), the effect of $P_R^{(3)}(\omega)$ in Eq.(4.4) can be neglected. The dependence of the signal on the phase ϕ is then expected insensitive to frequency. As we show in Fig. 31(a), there is no phase difference between the two dependences of $RI(\omega)$ on ϕ at Raman shifts 900.6 (red square dots) and 1200.8 cm^{-1} (green round dots). Using a sine fitting $[y_0 + A\sin(x + xc)]$ on the data at 900.6 cm^{-1} (blue curve), we find $xc = 0.16\pi$ instead of $\pi/2$ for a pure real background polarization $P_B^{(3)}(\omega)$. In our experiment, the definition of $\phi = 1.50\pi$ is limited by the resolution of the piezo stage. This definition can be derived within an error 0.14π , since the lineshapes at $\phi = 1.36\pi$ and 1.64π are easily distinguished from the one at $\phi = 1.50\pi$. Therefore, we obtain $\text{Im}(P_B^{(3)}(\omega))/\text{Re}(P_B^{(3)}(\omega)) = \cos(0.16\pi)/\sin(0.16\pi) = 1.8$ and in a range between 0.7 and 15.9. Here we confirm that constant (broadband) CARS background from water in the spectral region from 700 to 1400 cm^{-1} (the chemical fingerprint region) is not purely real. We attribute the existence of the imaginary part $\text{Im}(P_B^{(3)}(\omega))$ from water to the fact that water has some broad Raman lines crossing through the interested region [88,91]. Compared with that $P_B^{(3)}(\omega)$ would be expected a purely non-resonant background, it should be written here $P_B^{(3)}(\omega) = |P_B^{(3)}(\omega)|e^{0.34\pi}$ and Raman background due to water is almost purely imaginary.

Meanwhile, as shown in Fig. 31(b), there are very distinct phase differences between the dependences of the $RI(\omega)$ on ϕ at the positions within the resonant line, such as 1042.6, 1025.6 and 1059.6 cm^{-1} , which are roughly the resonant line's center frequency and half-maximum frequencies, respectively. In Fig. 31(b), we use a relative intensity $2 \times RI(\omega)/[RI(900.6) + RI(1200.8)]$ as signal since the absolute resonant contribution is easily overwhelmed by the fluctuation of the much stronger LO. The sine fitting (solid curves) to these three sets of experimental data (dots) gives $xc = 0.21\pi$, 0.09π and -0.22π at 1025.6, 1042.6 and 1059.6 cm^{-1} (from top

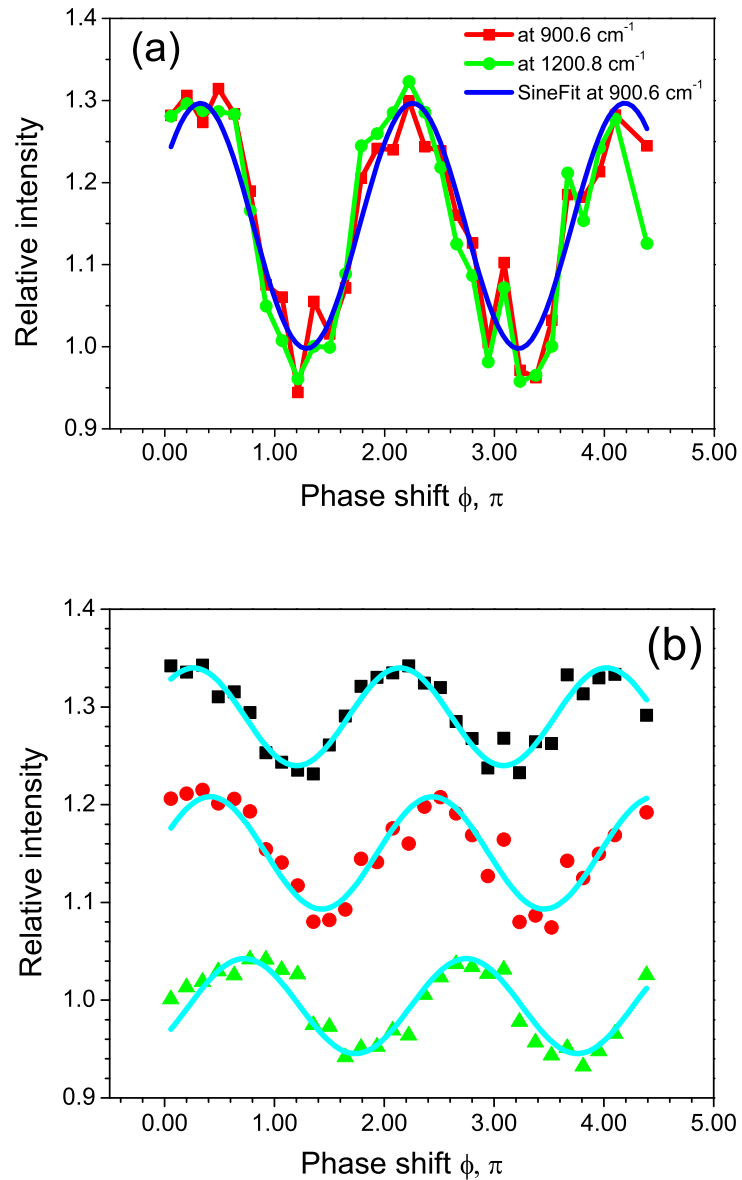


Fig. 31. Dependence of the interferometric spectra at fixed frequencies on the relative phase ϕ between the LO and signal fields. (a) Relative intensities $RI(\omega) = S(\omega)/S_{LO}(\omega)$ at nonresonant Raman shifts 900.6 cm^{-1} and 1200.8 cm^{-1} . (b) Rescaled as $2 \times RI(\omega)/[RI(900.6) + RI(1200.8)]$ at resonant Raman shifts of methanol $1025.6, 1042.6,$ and 1059.6 cm^{-1} , with offset $0.3, 0.15$ and 0 , respectively. Dots are experimental data and solid curves are sine fitting.

to bottom), respectively. Since $\text{Re}(P_R^{(3)}(\omega)) \approx 0$ at the center frequency of Raman line, $\text{Im}(P_R^{(3)}(\omega))/\text{Im}(P_B^{(3)}(\omega))$ is estimated to be 1.6 at 1042.6 cm^{-1} . Here we can see that water has a comparable contribution on the CARS signal with methanol. The contribution from water may result in incomplete background suppression, especially when the interested Raman signal is weak, as we discussed in Chapter III about glucose detection [20].

2. Extracting the real and imaginary components of $\chi_R^{(3)}$

Equation(4.4) shows that we can obtain the real or imaginary part of the susceptibility by subtracting the signal at two opposite phases:

$$\begin{aligned} \frac{S(\omega)_{\phi=\frac{\pi}{2}} - S(\omega)_{\phi=\frac{3\pi}{2}}}{P_{\text{LO}}^{(3)}(\omega)} &= 4\text{Im} \left(P_B^{(3)}(\omega) + P_R^{(3)}(\omega) \right) \\ &= 4E_{\text{EX}} \left[\text{Im} \left(\chi_B^{(3)}(\omega) \right) + \text{Im} \left(\chi_R^{(3)}(\omega) \right) \right], \end{aligned} \quad (4.6)$$

where E_{EX} denotes the excitation field. Similarly

$$\frac{S(\omega)_{\phi=0} - S(\omega)_{\phi=\pi}}{P_{\text{LO}}^{(3)}(\omega)} = 4E_{\text{EX}} \left[\text{Re} \left(\chi_B^{(3)}(\omega) \right) + \text{Re} \left(\chi_R^{(3)}(\omega) \right) \right]. \quad (4.7)$$

These are shown in Fig. 32a. The base of the real curve is offset from zero, which is consistent with the fact that in Figs. 30a and 30b the interferometric signals taken nominally at $\phi = 0$ and $\phi = \pi$ have opposite offsets from the LO signal, even for Raman shifts outside the narrow Raman resonance of methanol. This is expected from the background contribution $\chi_{\text{NR}}^{(3)}$.

We also note that the imaginary curve in Fig. 32a is offset from zero. Our calculation (the dotted curve in Fig. 32a) shows that the base of the imaginary curve would be zero if the background was nonresonant, such that $\text{Im}(\chi_B^{(3)}(\omega)) = 0$. However our measurement shows that the constant (broadband) CARS background from water

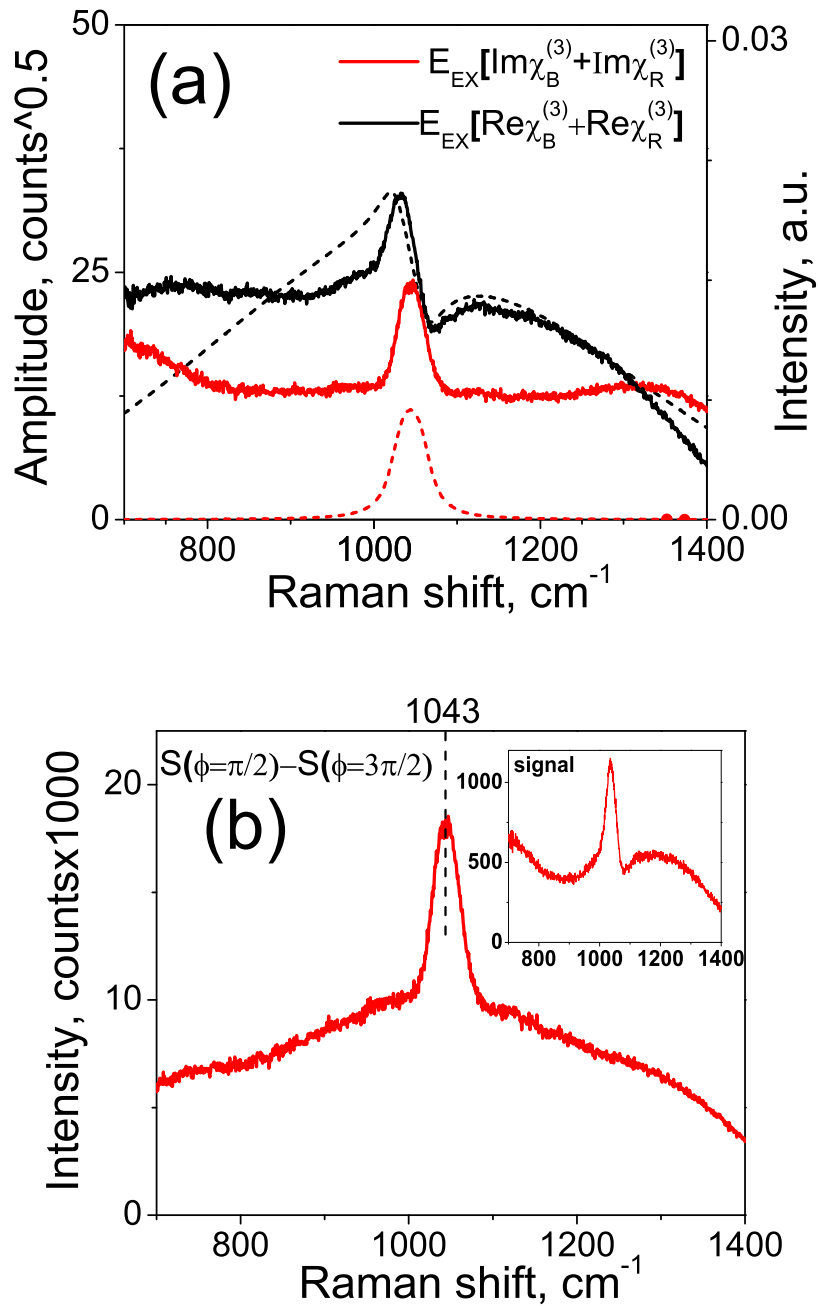


Fig. 32. Extracted susceptibility and heterodyne signal. (a) Extracted third order polarization hence the susceptibility from experiment (solid curves, scaled to left) and calculation (dashed and dotted curves, scaled to right). (b) Heterodyne signal including only the imaginary part of CARS field; inset: CARS field from the signal arm.

in the spectral region from 700 to 1400 cm^{-1} (the chemical fingerprint region) is not purely real (as would be expected from a purely non-resonant background). From Fig. 32a, the measured ratio between the imaginary and real background components is 0.6.

3. Heterodyne amplification

Fig. 32b and its inset show the heterodyne amplification. The original CARS signal is around 1000 counts, of which the resonant contribution $|P_R^{(3)}(\omega)|^2$ is estimated to be around 170 counts from Eq.(1.10). The net amplified resonant signal is around 8000 counts in Fig. 32b. An amplification factor around 50 is achieved, close to the calculated value of 70 in Fig. 30b. However, the contrast ratio is not significantly enhanced due to the imaginary contribution from water, while an infinite contrast ratio is expected in the ideal case (the dotted curve in Fig. 32a). In Fig. 32b, the measured Raman line of methanol has a FWHM of 35 cm^{-1} , which is the bandwidth of the probe beam and is slightly larger than the line width of methanol (FWHM 27 cm^{-1}). This is consistent with our expectation since the detected CARS signal is the convolution of the susceptibility and the applied fields.

E. Conclusion

In conclusion, we have demonstrated a heterodyne CARS method which combines broadband excitation with narrowband probing, and applied it to methanol solution to isolate the real and imaginary components of the molecular resonant susceptibility $\chi_R^{(3)}$. Since our scheme is optimized for multiplex CARS, we can readily obtain spectra resembling spontaneous Raman spectra over a sufficiently broad vibrational band, through the extraction of $\text{Im}(\chi_R^{(3)}(\omega))$. Heterodyne signal amplification factor of 50 is

achieved, which shows the potential for increased detection sensitivity. In addition, we show the utility of the heterodyne method to determine the phase of a broadband background, and find that the Raman background due to water is almost purely imaginary.

CHAPTER V

PULSE-SHAPER-ENABLED PHASE CONTROL OF NONRESONANT
BACKGROUND FOR HETERODYNE DETECTION OF CARS SIGNAL

A. Introduction

1. Development of interferometric CARS

As shown in Chapter IV, nonlinear interferometry is promising approach to suppress the nonresonant background in CARS, i.e. to extract the resonant field component of the CARS signal by means of a phase-sensitive measurement [62–65, 68–71]. This technique can be made to detect the imaginary part of the nonlinear susceptibility $\text{Im}\chi^{(3)}$ of the CARS signal, which then can be directly compared to the spontaneous Raman spectrum. Among these methods, the interferometer design, which introduces an external nonresonant reference field as the local oscillator (LO), relies on the stability of the interferometer itself; this approach was proposed 30 years ago [62] and widely applied, e.g. in our precious work [72], by Xie’s group [63, 64], and other groups [65, 68]. Single-pulse heterodyne detection scheme was then proposed (by Motzkus’s group), where the “blue” part of the laser spectrum acts as a LO [69]. Furthermore, Leone et al. have demonstrated a scheme to enhance the resonant signal intensity using the nonresonant signal as a LO, by a phase- and polarization-controlled pulse shaping technique [70, 71].

2. Intrinsic nonresonant FWM background as the LO

In this chapter, we present here a simple and effective heterodyne CARS scheme that uses the intrinsic nonresonant FWM background as the LO instead of applying an external one. Our approach is based on our hybrid CARS [20, 35, 72]. It is

implemented by controlling spectral properties of the probe pulse and its temporal overlap with the pump and Stokes pulses, and relies on the fact that the FWM is an instantaneous process and hence is directly related to the instantaneous probe field, while the resonant Raman signal is an accumulation process due to the vibrational coherence and hence is somewhat insensitive to the probe delay [12,92], as illuminated in Fig. 10. In our previous work, we tried to eliminate the FWM background [35] by introducing a top-hat probe spectrum. Here, on the contrary, we show that an asymmetry of the top-hat probe spectrum results in an imaginary contribution of the probe field in the time domain at the node of its real part. Consequently, the probe field gradually changes its phase by π when crossing the node, creating a temporal “Gouy phase” [93]. We also show that more asymmetry of the probe spectrum produces stronger probe field at the node, by comparing the experimental results from two different probe spectra. Therefore, we have the flexibility to control both the relative phase (by adjusting the probe delay) and the relative amplitude (by choosing desired probe spectrum) between the resonant Raman and FWM fields. As a result, we can for example directly extract the imaginary part of the third order susceptibility $\chi^{(3)}$ in aqueous methanol solution when the relative phase $\phi = \pi/2$ and the resonant signal can also be amplified by the heterodyne-like interference with the coherent background field.

The present experimental configuration shows additional advantages, compared to our previous work [20,35]. One is that the resonant background from aqueous solution can be removed due to its faster decay versus the probe delay. CARS with collinear beams, similar to the single-beam CARS [40,58,60], improves the spatial overlap compared to traditional cross-beam geometry. Meanwhile, the separate pump and Stokes frequency bands preserve the capacity to detect different Raman-shift regions.

The total CARS signal is proportional to the square of the polarization as in Eq.(1.10). In the current work, we create a complex FWM background $P_B^{(3)}(\omega, \tau)$ instead of a purely real one. In this case, we define ϕ as the phase of the background and Eq.(1.10) can be written as

$$S_{\text{CARS}} = |P_B^{(3)}|^2 + |P_R^{(3)}|^2 + 2\text{Re} \left[e^{i\phi} |P_B^{(3)}(\omega, \tau)| P_R^{(3)*}(\omega, \tau) \right]. \quad (5.1)$$

As an example, since the background level is often nearly constant, choosing $\phi = \pm\pi/2$ allows the extraction of the imaginary part of the Raman susceptibility, which can be directly compared with spontaneous Raman spectra. Clearly, the heterodyne signal depends on the concentration linearly and the imaginary part can be amplified significantly by the LO field.

B. Spectral asymmetry induced temporal phase shift in probe field

For an ideal sinc probe, its phase will jump by π through the node and it is what we would avoid for the heterodyne effect. Once the probe spectrum is slightly asymmetric (Fig. 33(a)), it is straightforward that the probe field in the time domain has a non-zero imaginary part (Fig. 33(d)) at the node of the real function (Fig. 33(c)). In Fig. 33, we show an example (black) that a top-hat probe spectrum with a Gaussian shoulder $e^{-(\omega+1)^2}$ on low-frequency side and hyper-Gaussian shoulder $e^{-(\omega-1)^4}$ on high-frequency side. However exact shapes are not so important, for example, simple Gaussian shoulders of different widths on the two sides of the spectrum also work, since asymmetry is essential during the Fourier transformation. The temporal functions in black in Fig. 33(b) to (f) correspond to the spectrum in black in Fig. 33(a). As comparison, we also show the spectrum with inverse shoulders and the corresponding temporal functions in magenta and dashed. Their absolute value and

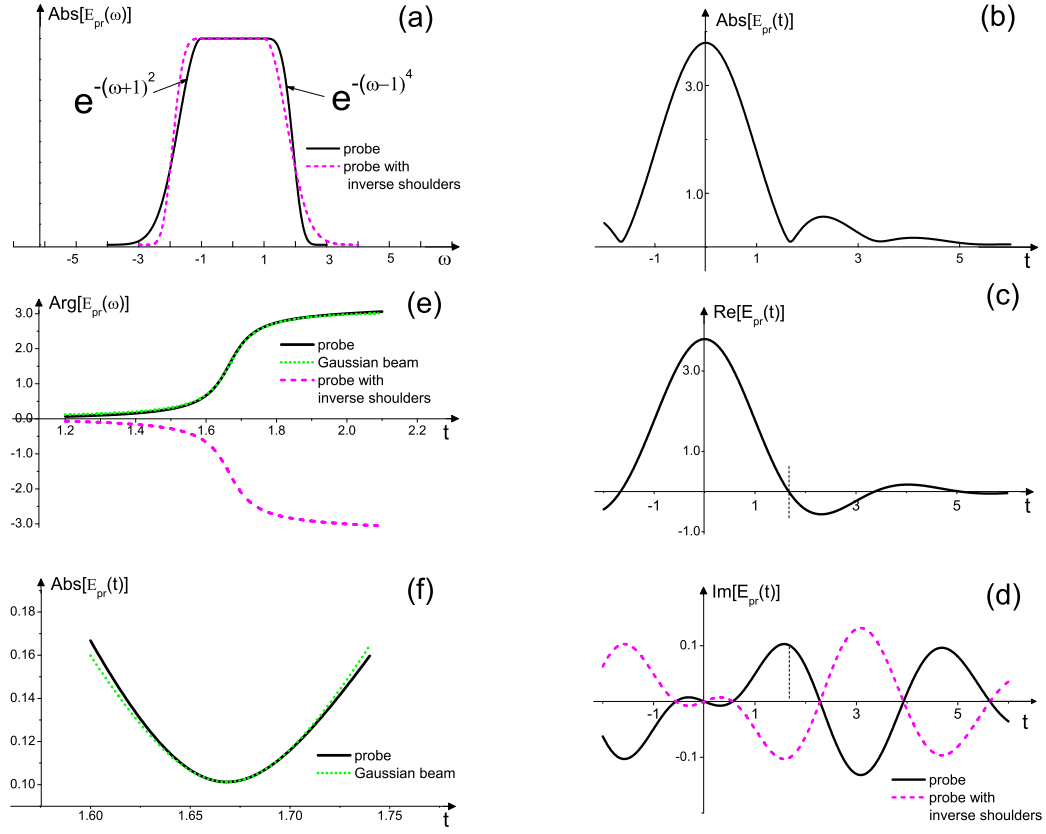


Fig. 33. Probe pulse in frequency and time domains. (a) A slightly asymmetric top-hat probe field $E_p(\omega)$ (black) and its inverse one (magenta and dashed), with Gaussian and hyper-Gaussian functions on the shoulders. The corresponding time-domain functions (black, magenta and dashed for the inverse one): (b) the absolute value $Abs[E_{pr}(t)]$, (c) the real part $Re[E_{pr}(t)]$, (d) the imaginary part $Im[E_{pr}(t)]$, and (e) the argument $Arg[E_{pr}(t)]$ of the probe field in (a). In (e) and (f), the black solid curves are for the probe beam and the green dotted curves are for a Gaussian beam $q(z) = -1.80977*(z - 1.668332) + 0.101261*I$.

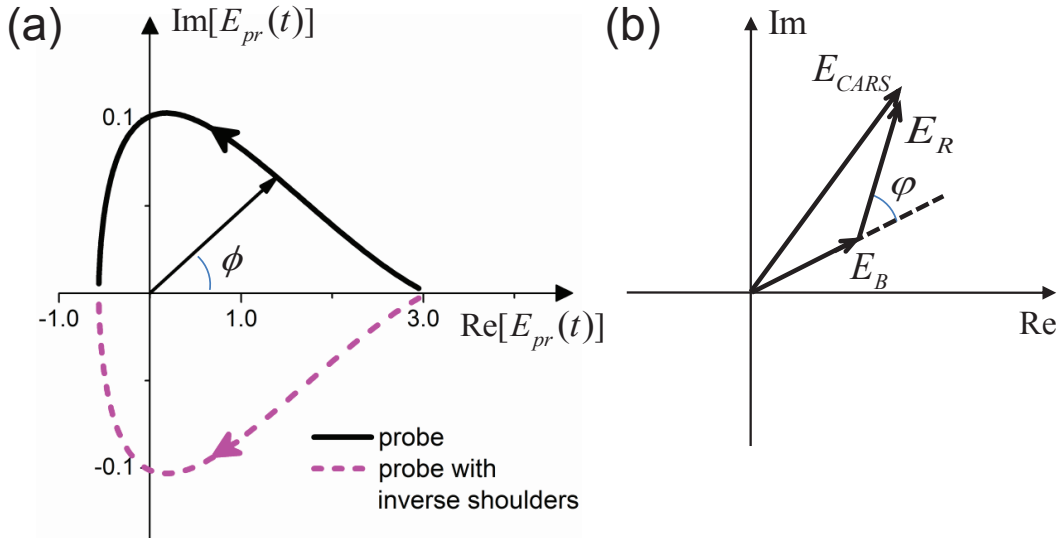


Fig. 34. Phase change of the nonresonant FWM (ϕ) through the probe node. (a) shows the absolute phase, and (b) shows the relative phase (φ) between the resonant signal and FWM. The arrows denote the change from less to larger probe delay. In (a), the black and magenta curves correspond to the spectra in black and magenta in Fig. 33(a), respectively.

real part are same in Fig. 33(b), (c) and (f), however the their imaginary parts are opposite in Fig. 33(d). As a result of the asymmetry, the argument of the complex probe field (black in Fig. 33(e)) will gradually shift from 0 to π crossing the node, and for the inverse one (magenta and dashed), from 0 to $-\pi$. Furthermore, we also have the flexibility to modify the asymmetry to change the proportion of the imaginary to the real components of the probe field. Thus we can control both the relative phase (Fig. 34) and relative amplitude between the FWM and resonant signal and therefore the FWM itself acts as the LO.

The study of the probe asymmetry is of practical interest, not only due to the self-implemented heterodyne effect discussed above. We have succeeded in eliminating the FWM background in our previous work [35]. However, properly introducing background benefits the detection sensitivity [20]. Moreover, it is impractical to

produce an perfect symmetric spectrum in the laboratory. This study will provide us a deeper understanding of CARS, especially for samples with low concentration where a small amount of FWM may contribute dominantly.

C. “Temporal Gouy phase”

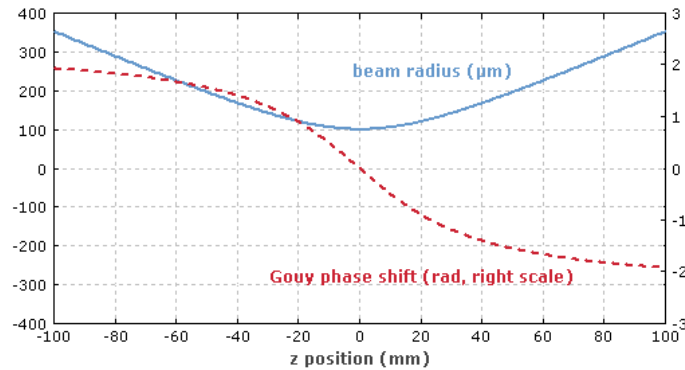


Fig. 35. Beam radius and Gouy phase shift along the propagation direction. This is a example for a beam in air with 1064 nm wavelength and 100 μm radius at the waist. The positions at plus and minus the Rayleigh length are marked. From “Encyclopedia for Photonics and Laser Technology” <http://www.rp-photonics.com>.

The asymmetry also leads to an interesting phenomenon - a “temporal” Gouy phase. (Spatial) Gouy phase, a phase shift by π , happens when a Gaussian beam evolves from $-\infty$ to $+\infty$ through a point focus, as shown in Fig. 35. When the real part of a function crosses zero, and the imaginary part is non-zero, the function can be approximated by the formula for Gaussian beam propagation which is described by a complex $q(z) = z + iz_R$ [93]. The important difference is that we have a function of time, and Gaussian beam propagates in space, so we will observe an analogous “Gouy phase”. As an example, we show in Fig. 33(e) and (f) (black) the argument $\text{Arg}[E_{pr}(t)]$ and absolute value $\text{Abs}[E_{pr}(t)]$ for the spec-

trum in Fig. 33(a) match those of the Gaussian beam propagation parameter $q(z) = -1.80977*(z-1.668332) + 0.101261*I$ (green, dotted), where z is replaced by t .

D. Experimental setup

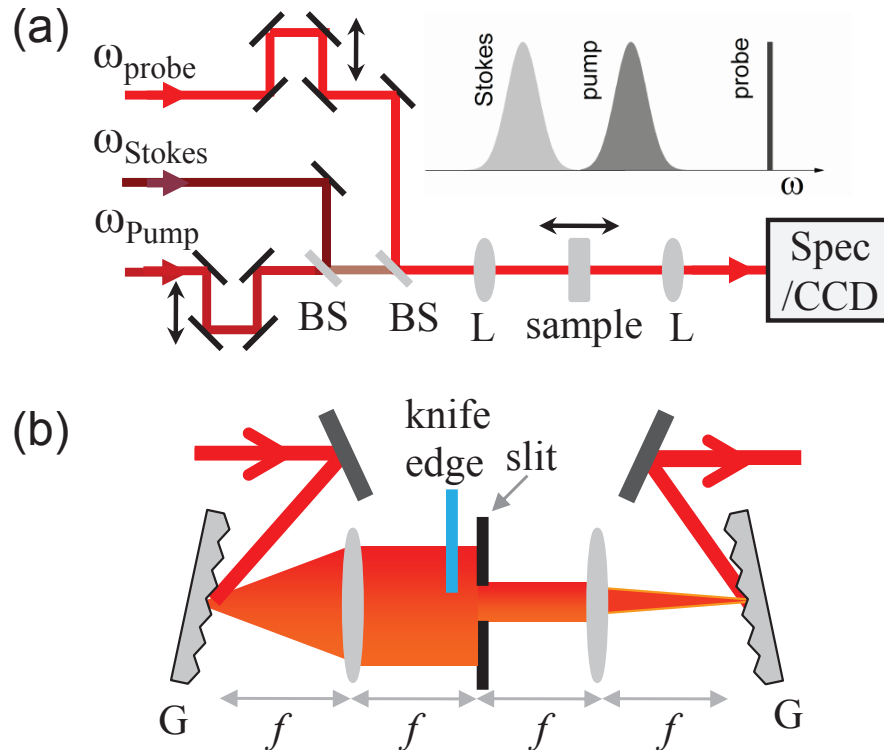


Fig. 36. Collinear hybrid CARS setup. (a) Experimental schematic; inset, the spectral ranges and profiles of the pump, Stokes and probe beams. (b) 4-f pulse shaper used to produce a top-hat-like probe spectrum; a knife edge can be placed in front of the focal plane to make the spectrum (more) asymmetric. BS, beam splitter; L, lens; Spec, spectrograph; G, grating.

The experimental setup is shown in Fig. 36. While still working in the hybrid scheme, we have the pump (1295 nm, FWHM 50 nm), Stokes (1500 nm, FWHM 70 nm) beams and probe beam (800 nm, width around 1 nm). The beams are focused with 10 cm lenses and the signal is collected with 5 cm focusing lenses then sent to a

spectrograph with a charge-coupled device (CCD) detector (Princeton Instrument, Spec-10:400BR/LN). We use a CCD exposure time of 200 ms for all spectra. The methanol aqueous solution of around 10% by volume is held in a 2 mm thick fused silica cell. Typical pulse energy in each pulse is a few hundred micro-joules. The asymmetry of the probe spectrum can be obtained by placing a knife edge off the focal plane of the 4-f system, e.g., in front of the slit which is on the focal plane (Fig. 36(b)).

E. Experimental results

1. Asymmetric probe spectra

In Fig. 37(a), we specially choose two probe pulses with opposite asymmetric spectra to verify the opposite phase changes in Fig. 33(e). The pulse without knife edge (blue, dotted curve) weighs less at shorter wavelength, which can be picked up by moving the slit to the ramp of the original broad probe spectrum. The pulse with knife edge (green, solid curve) weighs less at longer wavelength and has more asymmetry, which can be obtained by placing a knife edge in front of the slit.

Figure 37(b) shows the temporal profiles of the probe pulses, as measured through FWM on a thin glass slide with pump and Stokes pulses. These two curves are normalized to the same value at zero probe delay. There are non-zero nodes in both pulses. In particular, the spectrum with more asymmetry presents a explicitly stronger field at the nodes. The first node positions are 2.02 ps and 2.08 ps with and without knife-edge, respectively, which barely shift compared with the quite difference of the two spectra.

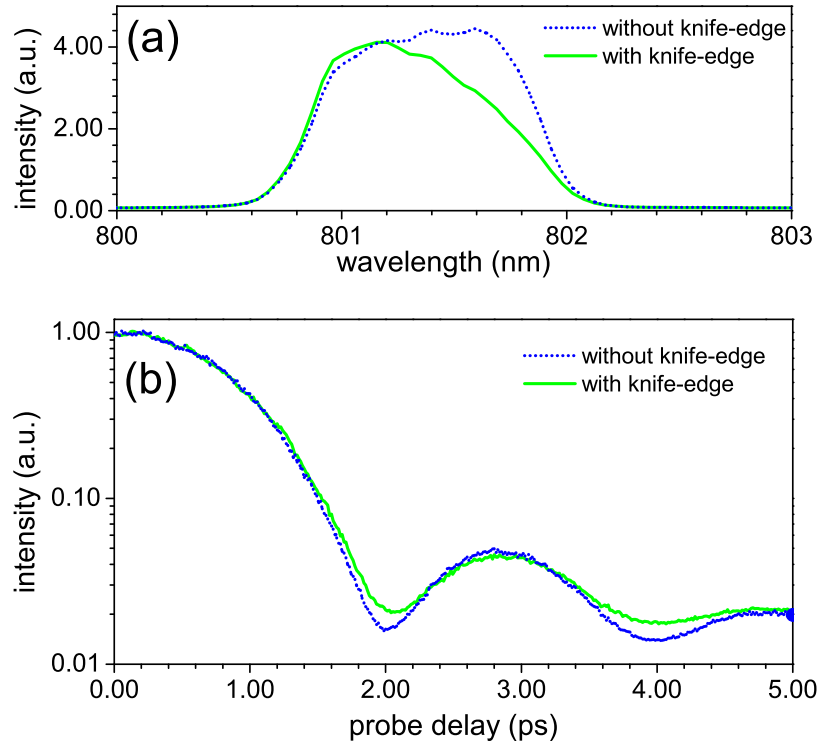


Fig. 37. Spectral (a) and temporal (b) shapes of the probe beam. Blue dotted and green solid curves are measured results without and with knife-edge in Fig. 36(b), respectively. The spectra are measured with a spectrometer, while the temporal shapes are obtained by recording the FWM of the pump, Stokes and probe beams during changing the probe delay.

2. Phase shift near the first probe node

Figure 38 shows the measured CARS spectra of methanol aqueous solution near the first probe nodes with (left column) and without knife-edge (right column). In order to highlight the feature of the Raman line, the spectra in Fig. 38 (a)-(d) are rescaled as $I_{CARS}(\omega)/I_B(\omega)$, where $I_B(\omega)$ is obtained through fitting to the FWM background. Fig. 38 (c) and (g) are the contour graphs without rescaling. In Fig. 38 (a) and (b), we expressly point out that there is a distinct phase change by π between the two spectra (insets) slightly after the first probe node (indicated by the arrows, at 2.08

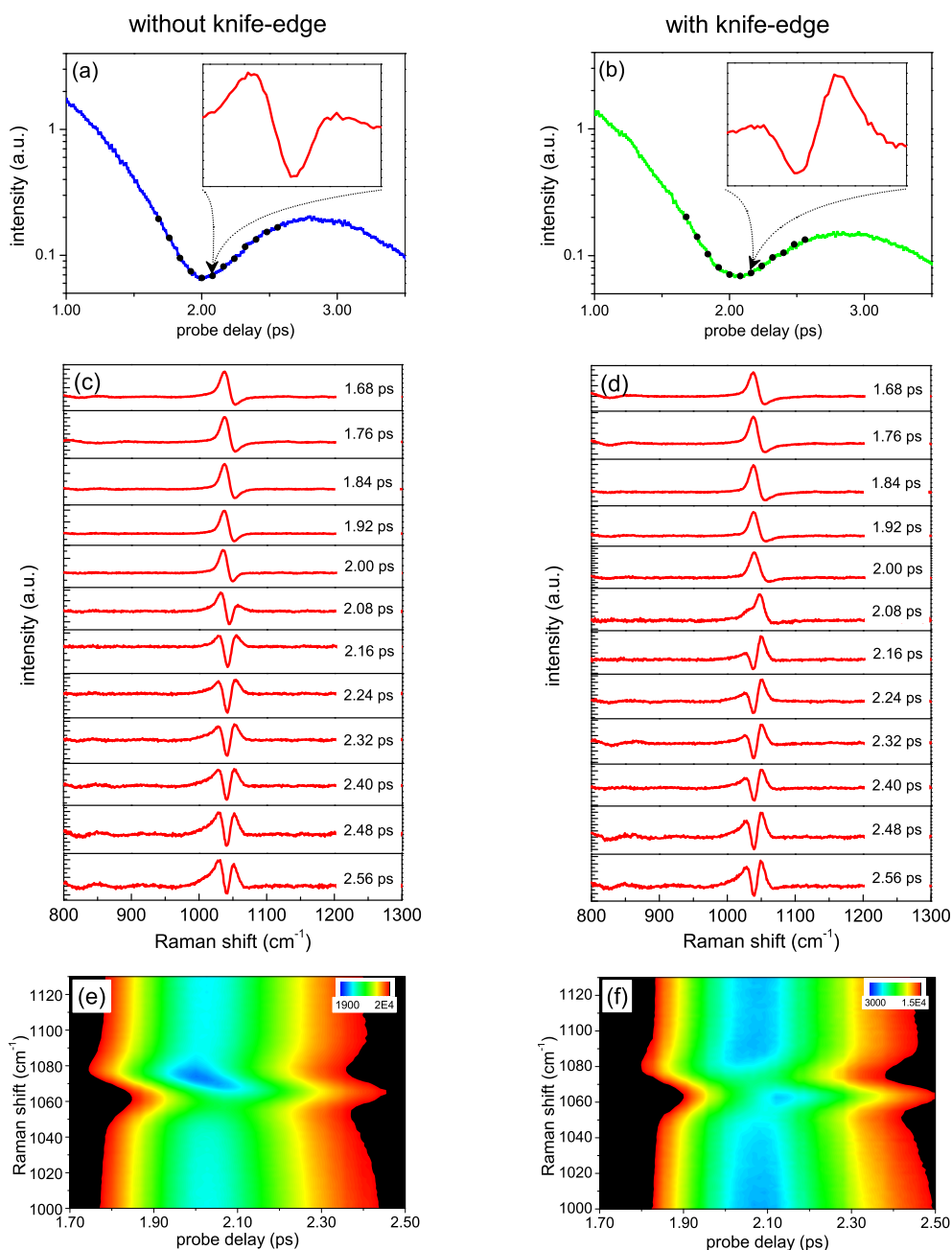


Fig. 38. Experimental CARS spectra of the methanol aqueous solution without and with a knife-edge. Insets of (a) and (b), at the nodes; (c) and (d), at different delays whose positions are marked as the black dots on the temporal shapes of the probe beam in (a) and (b), respectively; (e) and (f), the contour graphs. In (a)-(d), the spectra are rescaled as $S_{CARS}(\omega)/S_B(\omega)$ and $S_B(\omega)$ is obtained through fitting.

ps and 2.16 ps, respectively). The sine-like Raman line is the result of interference with FWM background, contrast to the Lorentz shape in absence of background.

The gradual changes of the phases are shown in Fig. 38 (c) and (d) when crossing through the first probe node. The numbers in the graphs are the probe delays, marked as the black dots on the probe temporal shapes in Fig. 38 (a) and (b). Obvious phase changes occur in both cases. However, it is not quite straightforward to estimate the phase change in Fig. 38 (c) where the resonant contribution $|P_R(\omega)|^2$ is also significant since $|P_R(\omega)|^2$ itself has complicated spectral shapes after the first node (see [92]). On the contrary, the phase change is more apparent in Fig. 38 where there is more FWM background. For example, the phase changes approximately by π from $\tau = 1.68$ ps to $\tau = 2.16$ ps and a transition phase appears at $\tau = 2.08$ ps (the node).

When we compare Fig. 38 (c) and (d), we find that the spectra are fairly similar far from the nodes and quite different near the nodes, e.g. those shown in Fig. 38 (a) and (b). This result confirm the expectation from Fig. 33 (e) that the phases difference from opposite spectral asymmetry reaches maximum (π) at the node and getting less further from the node. As a result, we can take advantage of this effect to control the phase of a signal just by moving the probe delay.

3. Extraction of the real and imaginary components of $\chi_R(\omega)$

In case of weak resonant signal so that $|P_B(\omega)| \gg |P_R(\omega)|$, the normalized CARS signal can be written as

$$S_{\text{CARS}}(\omega, \phi)/S_{\text{B}}(\omega, \phi) \approx 1 + 2 \frac{\text{Re} \left(e^{i\phi} P_R^*(\omega, \phi) \right)}{|P_B(\omega, \phi)|}, \quad (5.2)$$

where ϕ is the phase of the FWM background defined in Fig. 34, which is a function of the probe delay τ . This condition, $|P_B(\omega)| \gg |P_R(\omega)|$, is not satisfied well here.

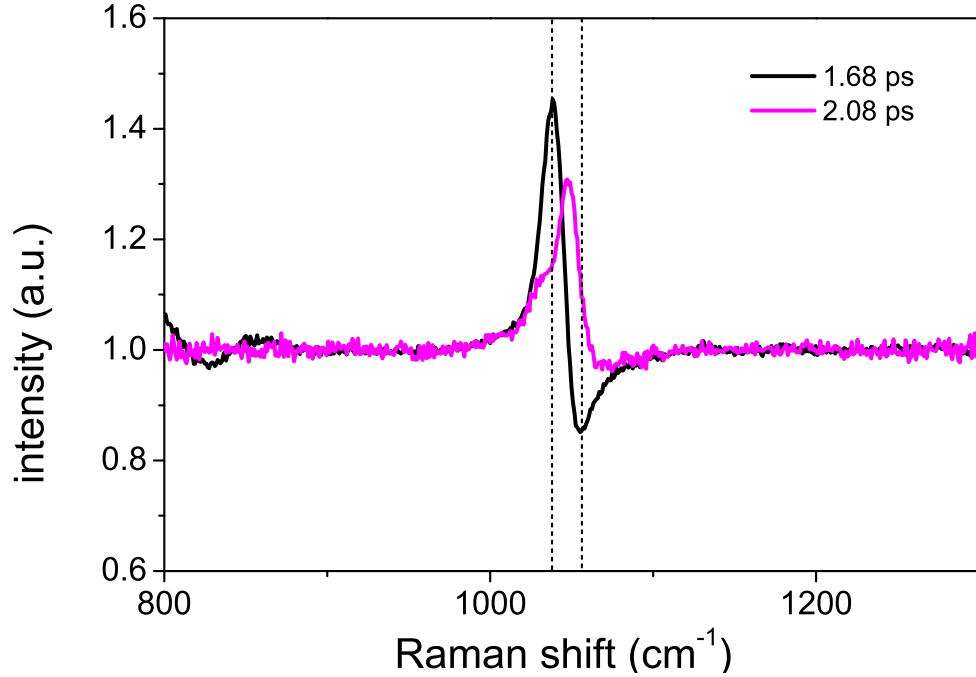


Fig. 39. CARS spectra to show the real and imaginary parts of $\chi_R^{(3)}(\omega)$. The real part (black) happens at 1.68 ps and the imaginary part (magenta) happens at 2.08 ps. They are from Fig. 38 but enlarged.

However, it is easily satisfied in many other cases, especially for the materials with small Raman cross sections and in low concentrations as we showed in our previous work [20].

When we change the probe delay, ϕ changes from 0 to π (or $-\pi$). Consequently we have

$$S_{\text{CARS}}(\omega, 0)/S_{\text{B}}(\omega, 0) \approx 1 + 2 \frac{\text{Re}(P_R^*(\omega, 0))}{|P_B(\omega, 0)|}, \quad (5.3)$$

$$S_{\text{CARS}}(\omega, \pi)/S_{\text{B}}(\omega, \pi) \approx 1 - 2 \frac{\text{Re}(P_R^*(\omega, \pi))}{|P_B(\omega, \pi)|}. \quad (5.4)$$

Since P_B is broadband and insensitive to frequency, $S_{\text{CARS}}(\omega, 0)/S_{\text{BG}}(\omega, 0)$ or $S_{\text{CARS}}(\omega, \pi)/S_{\text{BG}}(\omega, \pi)$ reflects the real part of $\chi_R(\omega)$. Similarly, the imaginary part

can be obtain through the following expression once we can find the probe delay corresponding to $\phi = \pi/2$

$$S_{\text{CARS}}(\omega, \pi/2)/S_{\text{B}}(\omega, \pi/2) \approx 1 + 2 \frac{\text{Im}(P_R^*(\omega, \pi/2))}{|P_B(\omega, \pi/2)|}. \quad (5.5)$$

The Experimental CARS spectra with knife-edge in Fig. 39 approximately reveal the real part (black, $\tau = 1.68$ ps) and imaginary part (magenta, $\tau = 2.08$ ps) of $\chi_R^{(3)}(\omega)$. The imaginary part represented by the magenta curve can be confirmed by the line shape and the peak position. However, in our case, the imaginary part does not look a perfect symmetric Lorentz shape since $|P_R(\omega, \tau)|^2 / |P_B(\omega, \pi/2)|^2$ cannot be neglected and distort the spectral shape. This can be improved by using a delay line with higher resolution ($1\mu\text{m}$ in our setup) to find the exact probe delay for $\phi = \pi/2$. Isolation of $\text{Im}(\chi_R^{(3)}(\omega))$ permits a direct comparison with spontaneous Raman spectra.

4. Controllable FWM amplitude

As we stated above that more asymmetry of the probe spectrum results in a stronger field at the node, we have the opportunity to control the relative intensity between the resonant Raman field and the FWM field. This is a based on the fact that appropriate introduction of background benefits detection sensitivity [20]. In Fig. 40, we show the CARS spectra without (black) and with (magenta) knife-edge at their nodes (2.02 and 2.08 ps, respectively), and as comparison, with knife-edge at 2.02 ps. The intensities of the Raman line with knife-edge, both at 2.02 ps (green, dashed) and 2.08 ps (magenta), is weaker than that without knife-edge due to the energy drop when the probe spectrum is cut; nevertheless, the intensities of the FWM background are stronger. The contrast ratios of the resonant signal to FWM are 0.71 (without knife-edge at 2.02 ps), 0.65 and 0.39 (with knife-edge at 2.02 and 2.08 ps, respectively).

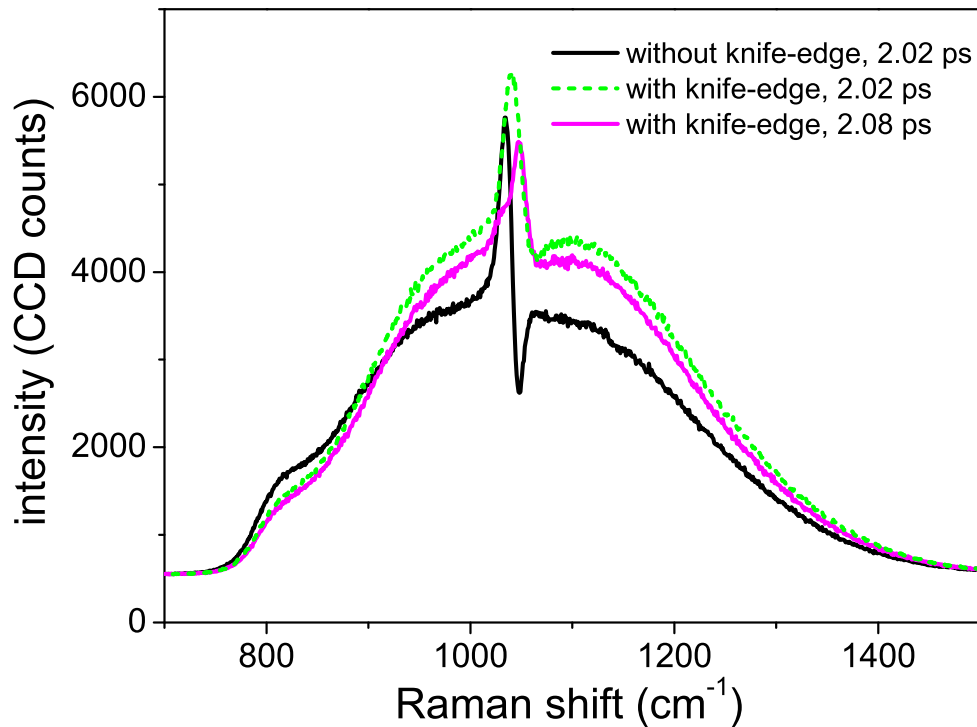


Fig. 40. CARS spectra at the first probe node without and with a knife-edge. The background level increases with the knife-edge (in both cases: magenta curve at the node 2.08 ps, green dashed curve at 2.02 ps), compared with that without the knife-edge (black curve at the node 2.02 ps). The probe node is defined to have the lowest background.

5. Asymmetry induced phase shift for CARS spectra with multiple Raman lines

Finally, we show how the spectral asymmetry of the probe affects the CARS spectra with multiple Raman lines in Fig. 41. The sample is 500 mM glucose aqueous solution and the experiment is carried out in a crossed-beam configuration. The experimental details are described in [20]. The right graph is the temporal shape of the probe, which has a non-zero first node. In the right graph, the Raman lines reverse when crossing the nodes, both the first and second ones. As a result, at the Raman shifts

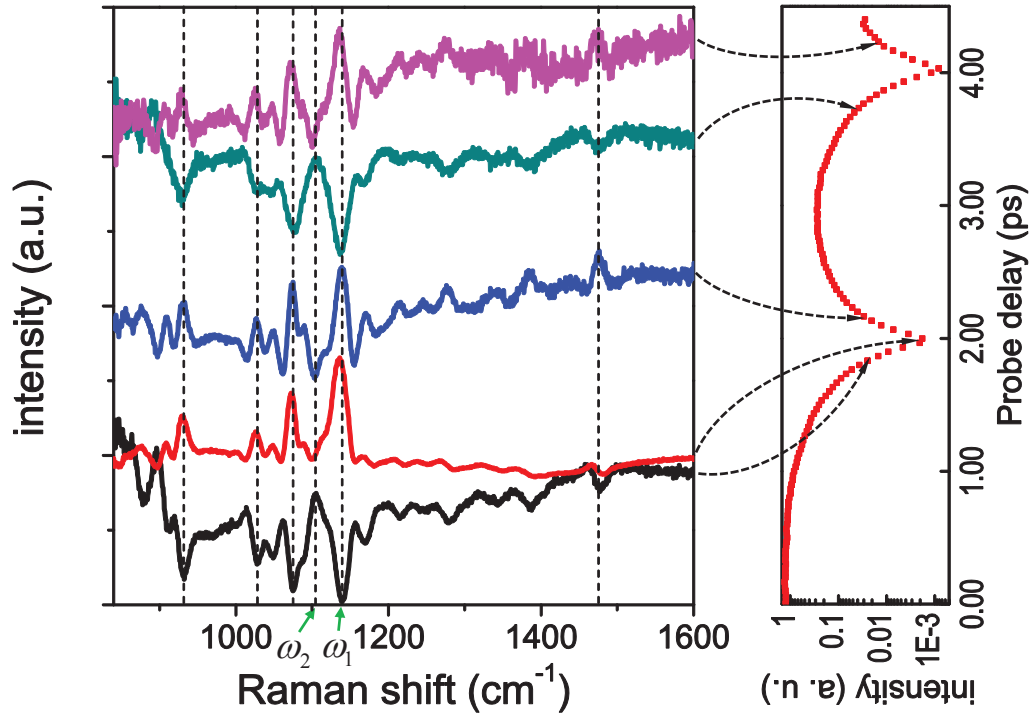


Fig. 41. Phase changes of the CARS signal from 500 mM glucose aqueous solution (left) near the probe nodes (right). The spectra are rescaled as $S_{CARS}(\omega)/S_B(\omega)$ and offset. The intensity ratios $[S(\omega_1) - S(\omega_2)]/S(\omega_2)$ are $-0.6/0.78, 2.14/0.72, 0.33/0.47, -0.21/0.76,$ and $0.18/0.67$ at probe delays 1.83, 2.0, 2.17, 3.73, and 4.23 ps, respectively. Note that the frequencies of the peaks (dips) off the node do shift relative to the one at the node but not observable in this scale.

marked by dashed vertical lines, we observe deep dips before the nodes (first and fourth curves from bottom) while sharp peaks after the nodes. For this case where the resonant signal is very strong, the CARS spectrum at the first node (second curve from bottom, red) resembles the spontaneous Raman spectrum. Therefore, it will be more precise to analyze the dips instead of peaks if we choose the spectra before the nodes, and vice versa.

F. Conclusion

In conclusion, we demonstrate a self-implemented heterodyne CARS by using its intrinsic FWM background as the local oscillator in a CARS configuration with two broadband Gaussian preparatory pulses and a time-delayed narrowband probe pulse. We introduce an imaginary component to the probe field in the time domain by inserting a knife-edge before the focal plane of a 4f pulse shaper which breaks the symmetry of the top-hat-like spectrum. Since the FWM instantaneously responds to the temporal overlap of the preparatory and the probe pulses, it undergoes a gradual phase shift by π when the preparatory pulses cross the node of the real part of the probe field. Due to vibrational coherence, the resonant Raman signal is insensitive to the overlapping position near the node. We observe the shape changes of the Raman line from aqueous methanol solution, furthermore, we can directly observe the imaginary part of $\chi_R^{(3)}$ when the phase of the FWM equals to π . We also show that more asymmetry of probe spectrum produces stronger probe field (and thus FWM) at the node by comparing the experimental results from two different probe spectra. Therefore, we have the flexibility to control both the relative phase between the resonant Raman and FWM fields by adjusting the probe delay and the relative amplitude by modifying the probe spectrum.

CHAPTER VI

CONCLUSIONS

We briefly conclude here our work on optimizing CARS by exploiting optical interference. This work is based on our time- and frequency-resolved multiplex CARS configuration, which combines instantaneous coherent excitation of multiple characteristic molecular vibrations by broadband femtosecond pump and Stokes pulses, with subsequent probing of these vibrations by an spectrally optimally shaped, time-delayed, narrowband and thus longer laser pulse in picosecond scale. The probe pulse is obtained through a home-made 4f pulse shaper with a mechanical slit to choose a desired narrow spectral band. This hybrid technique is developed to suppress the coherent FWM background which most often overwhelms the resonant Raman signal in CARS and causes distortion of the measured spectra due to the interference between them.

The hybrid technique has been proven to suppress the coherent background significantly and has been successfully applied to real-time spore detection (Chapter II) and glucose/blood detection(Chapter III). During our experiments, we find out that appropriate introduction of background benefits detection sensitivity since the signal may be amplified by the background. During the glucose measurement, We find a linear dependence of the CARS signal on the glucose concentrations due to interference between the resonant signal and the broad background from water. While the quadratic dependence of CARS signal on concentration makes efficient measurement for high concentrations, the linear dependence becomes an advantage for low concentrations. Our method is reliably capable of measuring glucose samples with concentration as low as 5 mM.

To make the fullest use of the background, we study the heterodyne CARS which,

by a phase-sensitive measurement, can extract the imaginary component of the third order susceptibility $\chi^{(3)}$ to eliminate the spectral distortion, and amplify the signal. We have carried out different experiments, where the interference either is controlled by introducing an external nonresonant field such as a FWM field from a glass slide (Chapter IV) or by controlling the phase of the intrinsic background (Chapter V).

The interferometric scheme we built in Chapter IV is simple and effective, providing most flexibility, where the relative amplitude and phase between the signal and local oscillator (LO) fields could be adjusted arbitrarily within the experimental limits. We have obtained an amplification factor around 50 or 70 depending on the intensity of the LO. We can also directly observe the real and imaginary components of the third-order nonlinear susceptibility $\chi^{(3)}$ of the sample.

However, the interferometric scheme is subject to the complexity of the setup and the stability of the interferometer itself, and thus can not be practical. In Chapter V, we then propose an improved heterodyne CARS scheme which uses the intrinsic nonresonant FWM background as the LO instead of applying an external one. The idea is to exploit time resolution to provide different effective phase for the nonresonant background and the Raman-resonant susceptibility which allows to adjust CARS spectra in a way to resemble Raman spectra. For this purpose the narrowband probe pulse is further spectrally tailored and temporarily shifted. In our experiment, we break the symmetry of the top-hat-like probe spectrum by inserting a knife-edge before the focal plane of the 4f pulse shaper and thus introduce an imaginary component to the probe field in the time domain. Since the FWM instantaneously responds to the temporal overlap of the preparatory and the probe pulses, it undergoes a gradual phase shift by π when the preparatory pulses cross the node of the real part of the probe field. Due to vibrational coherence, the resonant Raman signal is somewhat insensitive to the overlapping position near the node. We can directly observe the

imaginary part of $\chi^{(3)}$ from aqueous methanol solution when the phase of the FWM equals to $\pi/2$. In this scheme, we have the flexibility, just like the interferometric one although not arbitrarily, to control both the relative phase between the resonant Raman and FWM fields by adjusting the probe delay and the relative amplitude by modifying the probe spectrum.

REFERENCES

- [1] C. V. Raman and K. S. Krishnan, "A new type of secondary radiation," *Nature* **121**, 501-502 (1928).
- [2] N. Bloembergen, "The stimulated Raman effect," *Am. J. Phys.* **35**, 989-1023 (1967).
- [3] P.D. Maker, R.W. Terhune, "Study of optical effects due to an induced polarization third order in the electric field strength," *Phys. Rev. A* **137**, 801-818 (1965).
- [4] R. F. Begley, A. B. Harvey, and R. L. Byer, "Coherent anti-Stokes Raman spectroscopy," *Appl. Phys. Lett.* **25**, 387-390 (1974).
- [5] N. I. Koroteev, "BioCARS-a novel nonlinear optical technique to study vibrational spectra of chiral biological molecules in solution," *Biospectrosc.* **1**, 341-350 (1995).
- [6] M. Fleischmann, P.J. Hendra, and A.J. McQuillan, "Raman spectra of pyridine absorbed at a silver electrode," *Chem. Phys. Lett.* **26**, 163-166 (1974).
- [7] J.R. Lombardi and R.L. Birke, "A unified approach to surface-enhanced Raman spectroscopy," *J. Phys. Chem. C* **112**, 5605-5617 (2008).
- [8] J. R. Lombardi, and R. L. Birke, "A unified view of surface-enhanced Raman scattering," *Acc. Chem. Res.* **42**, 734-742 (2009).
- [9] J. E. Wessel, "Surface-enhanced optical microscopy," *J. Opt. Soc. A. B* **2**, 1538-1541 (1985).

- [10] R. M. Stockle, Y.D. Suh, V. Deckert, and R. Zenobi, "Nanoscale chemical analysis by tip-enhanced Raman spectroscopy," *Chem. Phys. Lett.* **318**, 131-136 (2000)
- [11] W. M. Tolles, J. W. Nibler, J. R. McDonald, and A. B. Harvey, "A review of the theory and application of coherent anti-Stokes Raman spectroscopy (CARS)," *Appl. Spectrosc.* **31**, 253-271 (1977).
- [12] G. L. Eesley, *Coherent Raman Spectroscopy* (Pergamon Press, Oxford, New York, 1981).
- [13] Y.R. Shen, *The Principles of Nonlinear Optics*(J. Wiley, New York, 1984).
- [14] A. C. Eckbreth, *Laser Diagnostics for Combustion Temperature and Species* (Gordon and Breach Publishers, Amsterdam, the Netherlands, 1996).
- [15] A. M. Zheltikov, "Coherent anti-Stokes Raman scattering: From proof-of-the-principle experiments to femtosecond CARS and higher order wave-mixing generalizations," *J. Raman Spectrosc.* **31**, 653-667 (2000).
- [16] J.-X. Cheng and X. S. Xie, "Coherent anti-Stokes Raman scattering microscopy: Instrumentation, theory and applications," *J. Phys. Chem. B* **108**, 827-840 (2004).
- [17] C. L. Evans and X. S. Xie, "Coherent anti-Stokes Raman scattering microscopy: Chemical imaging for biology and medicine," *Annu. Rev. Anal. Chem.* **1**, 883-909 (2008).
- [18] M. Schmitt, G. Knopp, A. Materny, and W. Kiefer, "The application of femtosecond time-resolved coherent anti-Stokes Raman scattering for the investigation of

- ground and excited state molecular dynamics of molecules in the gas phase,” *J. Phys. Chem. A* **102**, 4059-4065 (1998).
- [19] R. D. Hancock, F. R. Schauer, R. P. Lucht, and R. L. Farrow, “Dual-pump coherent anti-Stokes Raman scattering measurements of nitrogen and oxygen in a laminar jet diffusion flame,” *Appl. Opt.* **36**, 3217-3226 (1997).
- [20] X. Wang, A. Zhang, M. Zhi, A. V. Sokolov, and G. R. Welch, “Glucose concentration measured by the hybrid coherent anti-Stokes Raman-scattering technique,” *Phys. Rev. A* **81**, 013813 (2010).
- [21] M. Zhi, D. Pestov, X. Wang, R. K. Murawski, Y. V. Rostovtsev, Z.-E. Sariaynni, V. A. Sautenkov, N. G. Kalugin, and A. V. Sokolov, “Concentration dependence of femtosecond coherent anti-Stokes Raman scattering in the presence of strong absorption,” *J. Opt. Soc. Am. B* **24**, 1181-1186 (2007).
- [22] W. Zinth, A. Laubereau, and W. Kaiser, “Time resolved observation of resonant and non-resonant contributions to the nonlinear susceptibility $\chi^{(3)}$,” *Opt. Commun.* **26**, 457-462 (1978).
- [23] B. Dick, “Response function theory of time-resolved CARS and CSRS of rotating molecules in liquids under general polarization conditions,” *Chem. Phys.* **113**, 131-147 (1987).
- [24] R. Leonhardt, W. Holzappel, W. Zinth, and W. Kaiser, “Terahertz quantum beats in molecular liquids,” *Chem. Phys. Lett.* **133**, 373-377 (1987).
- [25] S. Meyer, and V. Engel, “Femtosecond time-resolved CARS and DFWM spectroscopy on gas-phase I_2 : A wave-packet description,” *J. Raman Spectrosc.* **31**, 33-39 (2000).

- [26] A. Materny, T. Chen, M. Schmitt, T. Siebert, A. Vierheilig, V. Engel, and W. Kiefer, "Wave packet dynamics in different electronic states investigated by femtosecond time-resolved four-wave-mixing spectroscopy," *Appl. Phys. B* **71**, 299-317 (2000).
- [27] T. Siebert, M. Schmitt, V. Engel, A. Materny, and W. Kiefer, "Population dynamics in vibrational modes during non-Born-Oppenheimer processes: CARS spectroscopy used as a mode selective filter," *J. Am. Chem. Soc.* **124**, 6242-6243 (2002).
- [28] R. P. Lucht, S. Roy, T. R. Meyer, and J. R. Gord, "Femtosecond coherent anti-Stokes Raman scattering measurement of gas temperatures from frequency-spread dephasing of the Raman coherence," *Appl. Phys. Lett.* **89**, 251112 (2006).
- [29] F. M. Kamga and M. G. Sceats, "Pulse-sequenced coherent anti-Stokes Raman scattering spectroscopy: A method for suppression of the nonresonant background," *Opt. Lett.* **5**, 126-128 (1989).
- [30] A. Volkmer, L. D. Book, and X. S. Xie, "Time-resolved coherent anti-Stokes Raman scattering microscopy: Imaging based on Raman free induction decay," *Appl. Phys. Lett.* **80**, 1505-1507 (2002).
- [31] B. D. Prince, A. Chakraborty, B. M. Prince, and H. U. Stauffer, "Development of simultaneous frequency- and time-resolved coherent anti-Stokes Raman scattering for ultrafast detection of molecular Raman spectra," *J. Chem. Phys.* **125**, 044502 (2006).
- [32] D. Pestov, X. Wang, G. O. Ariunbold, R. K. Murawski, V. A. Sautenkov, A. Dogariu, A.V. Sokolov, and M. O. Scully, "Single-shot detection of bacterial

- endospores via coherent Raman spectroscopy,” *Proc. Natl. Acad. Sci. USA* **105**, 422-427 (2008).
- [33] J.-X. Cheng, A. Volkmer, L. D. Book, and X. S. Xie, “Multiplex coherent anti-Stokes Raman scattering microspectroscopy and study of lipid vesicles,” *J. Phys. Chem. B* **106**, 8493-8498 (2002).
- [34] H. Kano and H. Hamaguchi, “Vibrationally resonant imaging of a single living cell by supercontinuum-based multiplex coherent anti-Stokes Raman scattering microspectroscopy,” *Opt. Express* **13**, 1322-1327 (2005).
- [35] D. Pestov, R. K. Murawski, G. O. Ariunbold, X. Wang, M. Zhi, A. V. Sokolov, V. A. Sautenkov, Y. V. Rostovtsev, A. Dogariu, Y. Huang, and M. O. Scully, “Optimizing the laser-pulse configuration for coherent Raman spectroscopy,” *Science* **316**, 265-268 (2007).
- [36] K. P. Knutsen, B. M. Messer, R. M. Onorato, and R. J. Saykally, “Chirped coherent anti-Stokes Raman scattering for high spectral resolution spectroscopy and chemically selective imaging,” *J. Phys. Chem. B* **110**, 5854-5864 (2006).
- [37] P. C. Chen, C. C. Joyner, and M. Burns-Kaurin, “Multiplex coherent anti-Stokes Raman spectroscopy by use of a nearly degenerate broadband optical parametric oscillator,” *Appl. Opt.* **38**, 5894-5898 (1999).
- [38] L. Ujj, B. L. Volodin, A. Popp, J. K. Delaney, and G. H. Atkinson, “Picosecond resonance coherent anti-Stokes Raman spectroscopy of bacteriorhodopsin: Spectra and quantitative third-order susceptibility analysis of the light-adapted BR-570,” *Chem. Phys.* **182**, 291-311 (1994).

- [39] A. Voroshilov, C. Otto, J. Greve, “On the coherent vibrational phase in polarization sensitive resonance CARS spectroscopy of copper tetraphenylporphyrin,” *J. Chem. Phys.* **106**, 2589-2598 (1997).
- [40] N. Dudovich, D. Oron, and Y. Silberberg, “Single-pulse coherently controlled nonlinear Raman spectroscopy and microscopy,” *Nature* **418**, 512-514 (2002).
- [41] B-C. Chen and S-H Lim, “Optimal laser pulse shaping for interferometric multiplex coherent anti-Stokes Raman scattering microscopy,” *J. Phys. Chem. B* **112**, 3653-3661 (2008).
- [42] D. Pestov, X. Wang, R. K. Murawski, G. O. Ariunbold, V. A. Sautenkov, and A. V. Sokolov, “Pulse shaping for mode-selective ultrafast coherent Raman spectroscopy of highly scattering solids,” *J. Opt. Soc. Am. B* **25**, 768-772 (2008).
- [43] D. Pestov, G. O. Ariunbold, X. Wang, R. K. Murawski, V. A. Sautenkov, A. V. Sokolov, and M. O. Scully, “Coherent versus incoherent Raman scattering: Molecular coherence excitation and measurement,” *Opt. Lett.* **32**, 1725-1727 (2007).
- [44] G. I. Petrov, R. Arora, V. V. Yakovlev, X. Wang, A. V. Sokolov, and M. O. Scully, “Comparison of coherent and spontaneous Raman microspectroscopies for noninvasive detection of single bacterial endospores,” *Proc. Natl. Acad. Sci. USA* **104**, 7776-7779 (2007).
- [45] M. O. Scully, G. W. Kattawar, R. P. Lucht, T. Opatrny, H. Pilloff, A. Rebane, A. V. Sokolov, and M. S. Zubairy, “FAST CARS: Engineering a laser spectroscopic technique for rapid identification of bacterial spores,” *Proc. Natl. Acad. Sci. U.S.A.* **99**, 10994-11001 (2002).

- [46] A. C. Eckbreth, "BOXCARS: Crossed-beam phase-matched CARS generation in gases," *Appl. Phys. Lett.* **32**, 421-423 (1978).
- [47] M. Zhi, X. Wang, and A. V. Sokolov, "Broadband coherent light generation in diamond driven by femtosecond pulses," *Opt. Express* **16**, 12139-12147 (2008).
- [48] M. Zhi, X. Wang, and A. V. Sokolov, "Broadband light generation using a relatively weak Raman mode in lead tungstate crystal," *J. Mod. Opt.* **57**, 1863-1869 (2010).
- [49] J.-X. Cheng, A. Volkmer, D. Book, and X. S. Xie, "An epi-detected coherent anti-Stokes Raman scattering (E-CARS) microscope with high spectral resolution and high sensitivity," *Phys. Chem. B* **105**, 1277-1280 (2001).
- [50] J.-X. Cheng, L. D. Book, and X. S. Xie, "Polarization coherent anti-Stokes Raman scattering microscopy," *Opt. Lett.* **26**, 1341-1343 (2001).
- [51] A. Zumbusch, G. R. Holtom, and X. S. Xie, "Three-dimensional vibrational imaging by coherent anti-Stokes Raman scattering," *Phys. Rev. Lett.* **82**, 4142-4145 (1999).
- [52] P. Kukura, D. W. McCamant, and R. A. Mathies, "Femtosecond stimulated Raman spectroscopy," *Annu. Rev. Phys. Chem.* **58**, 461-488 (2007).
- [53] B. G. Saar, C. W. Freudiger, J. Reichman, C. M. Stanley, G. R. Holtom, and X. S. Xie, "Video-rate molecular imaging in vivo with stimulated Raman scattering," *Science* **330**, 1368-1370 (2010).
- [54] T. Yajima, "Optical mixing due to third order nonlinear polarization in quartz," *J. Phys. Sot. Japan* **21**, 1583-1592 (1966).

- [55] R. T. Lynch Jr., Third-order nonlinear spectroscopy of liquids and crystals, Ph.D. thesis, pp. 1-9 (Harvard University, 1977).
- [56] J.J. Song, G. L. Eesley, and M. D. Levenson, "Background suppression in coherent Raman spectroscopy," *Appl. Phys. Lett.* **29**, 567-569 (1976).
- [57] J.-L. Oudar, R. W. Smith, and Y. R. Shen, "Polarization sensitive coherent anti-Stokes Raman spectroscopy," *Appl. Phys. Lett.* **34**, 758-760 (1979).
- [58] S. Roy, P. J. Wrzesinski, D. Pestov, M. Dantus, and J. R. Gord, "Single-beam coherent anti-Stokes Raman scattering (CARS) spectroscopy of gas-phase CO₂ via phase and polarization shaping of a broadband continuum," *J. Raman Spectrosc.* **41**, 1194-1199 (2010).
- [59] D. Oron, N. Dudovich, D. Yelin, and Y. Silberberg, "Quantum control of coherent anti-Stokes Raman processes," *Phys. Rev. A.* **65**, 043408 (2002).
- [60] D. Oron, N. Dudovich, D. Yelin, and Y. Silberberg, "Narrow-band coherent anti-Stokes Raman signals from broad-band pulses," *Phys. Rev. Lett.* **88**, 063004 (2002).
- [61] B. Yellampalle, R. D. Averitt, A. Efimov, and A. J. Taylor, "Spectral interferometric coherent Raman imaging," *Opt. Express* **13**, 7672-7682 (2005).
- [62] Y. Yacoby, R. Fitzgibbon, and B. Lax, "Coherent cancellation of background in four-wave mixing spectroscopy," *J. Appl. Phys.* **51**, 3072-3077 (1980).
- [63] E. O. Potma, C. L. Evans, and X. S. Xie, "Heterodyne coherent anti-Stokes Raman scattering (CARS) imaging," *Opt. Lett.* **31**, 241-243 (2006).

- [64] C. L. Evans, E. O. Potma, and X. S. Xie, “Coherent anti-Stokes Raman scattering interferometry: Determination of the real and imaginary components of nonlinear susceptibility $\chi^{(3)}$ for vibrational microscopy,” *Opt. Lett.* **29**, 2923-2925 (2004).
- [65] M. Jurna, J. P. Korterik, C. Otto, J. L. Herek, and H. L. Offerhaus, “Background free CARS imaging by phase sensitive heterodyne CARS,” *Opt. Express* **16**, 15863-15869(2008).
- [66] G. W. Jones, D. L. Marks, C. Vinegoni, and S. A. Boppart, “High-spectral-resolution coherent anti-Stokes Raman scattering with interferometrically detected broadband chirped pulses,” *Opt. Lett.* **31**, 1543-1545 (2006).
- [67] L. Lepetit, G. Chériaux, and M. Joffre, “Linear techniques of phase measurement by femtosecond spectral interferometry for applications in spectroscopy,” *J. Opt. Soc. Am. B.* **12**, 2467-2474 (1995).
- [68] T. W. Kee, H. Zhao, and M. T. Cicerone, “One-laser interferometric broadband coherent anti-Stokes Raman scattering,” *Opt. Express* **14**, 3631-3640 (2006).
- [69] C. Müller, T. Buckup, B. von Vacano, and M. Motzkus, “Heterodyne single-beam CARS microscopy,” *J. Raman Spectrosc.* **40**, 809-816 (2009).
- [70] S.-H. Lim, A. G. Caster, and S. R. Leone, “Single-pulse phase-control interferometric coherent anti-Stokes Raman scattering spectroscopy,” *Phys. Rev. A* **72**, 041803(R) (2005).
- [71] S.-H. Lim, A. G. Caster, and S. R. Leone, “Fourier transform spectral interferometric coherent anti-Stokes Raman scattering (FTSI-CARS) spectroscopy,” *Opt. Lett.* **32**, 1332-1334 (2007).

- [72] X. Wang, A. Zhang, M. Zhi, A. V. Sokolov, G. R. Welch, and M. O. Scully, "Heterodyne coherent anti-Stokes Raman scattering for spectral phase retrieval and signal amplification," *Opt. Lett.* **35**, 721-723 (2010).
- [73] D. Pestov, M. Zhi, Z. E. Sariyanni, N. G. Kalugin, A. A. Kolomenskii, R. K. Murawski, G. G. Paulus, V. A. Sautenkov, H. Schuessler, A. V. Sokolov, G. R. Welch, Y. V. Rostovtsev, T. Siebert, D. A. Akimov, S. Graefe, W. Kiefer, and M. O. Scully, "Visible and UV coherent Raman spectroscopy of dipicolinic acid," *Proc. Natl. Acad. Sci. U.S.A.* **102**, 14976-14981 (2005).
- [74] W. Zinth, "Transient coherent Raman scattering in the time and frequency domain," *Opt. Commun.* **34**, 479-482 (1980).
- [75] P. Carmona, "Vibrational-spectra and structure of crystalline dipicolinic acid and calcium dipicolinate trihydrate," *Spectrochimica Acta Part a-Molecular and Biomolecular Spectroscopy* **36**, 705-712 (1980).
- [76] A. Heller, "Implanted electrochemical glucose sensors for the management of diabetes," *Annu. Rev. Biomed. Eng.* **1**, 153-175 (1999).
- [77] V. V. Tuchin, *Tissue Optics: Light Scattering Methods and Instruments for Medical Diagnosis* (SPIE Press, Bellingham, WA, 2000).
- [78] J. Chaiken, W. Finney, P. E. Knudson, R. S. Weinstock, M. Khan, R. J. Bussejager, D. Hagrman, P. Hagrman, Y. W. Zhao, C. M. Peterson, and K. J. Peterson, "Effect of hemoglobin concentration variation on the accuracy and precision of glucose analysis using tissue modulated, noninvasive, in vivo Raman spectroscopy of human blood: A small clinical study," *Biomed. Opt.* **10**, 031111 (2005).
- [79] A. J. Berger, I. Itzkan, and M. S. Feld, "Feasibility of measuring blood glucose

- concentration by near-infrared Raman spectroscopy,” *Molecular and Biomolecular Spectroscopy* **53**, 287-292 (1997).
- [80] M. Akeson, C. Brackmann, L. Gustafsson, and A. Enejder, “Chemical imaging of glucose by CARS microscopy,” *J. Raman Spectrosc.* **41**, 1638-1644 (2010).
- [81] H. A. Szymanski, *Raman Spectroscopy* (Plenum, New York, 1967).
- [82] R. Petry, M. Schmitt, and J. Popp, “Raman spectroscopy – a prospective tool in the life sciences,” *ChemPhysChem* **4**, 14-30 (2003).
- [83] A. Dogariu, A. Goltsov, H. Xia, and M. O. Scully, “Concentration dependence in coherent Raman scattering,” *J. Mod. Opt.* **55**, 3255-3261 (2008).
- [84] A. Dogariu, A. Goltsov, D. Pestov, A.V. Sokolov, and M. O. Scully, “Real-time detection of bacterial spores using coherent anti-Stokes Raman spectroscopy,” *J. Appl. Phys.* **103**, 036103 (2008).
- [85] K. E. Shafer-Peltier, C. L. Haynes, M. R. Glucksberg, and R. P. Van Duyne, “Toward a glucose biosensor based on surface-enhanced Raman scattering,” *J. Am. Chem. Soc.* **125**, 588-593 (2003)
- [86] J. G. Skinner and W. G. Nilsen, “Absolute Raman scattering cross-section measurement of the 992 cm^{-1} line of benzene,” *J. Opt. Soc. A.* **58**, 113-118 (1968).
- [87] C. Molteni and M. Parrinello, “Glucose in aqueous solution by first principles molecular dynamics,” *J. Am. Chem. Soc.* **120**, 2168-2171 (1998).
- [88] Y. Tominaga, A. Fujiwara, and Y. Amo, “Dynamical structure of water by Raman spectroscopy,” *Fluid Phase Equilibria* **144**, 323-330 (1998).

- [89] S.-H. Shim and M. T. Zanni, “How to turn your pump-probe instrument into a multidimensional spectrometer: 2D IR and Vis spectroscopies via pulse shaping,” *Phys. Chem. Chem. Phys.* **11**, 748-761 (2009).
- [90] D. Abramavicius, B. Palmieri, D. V. Voronine, F. Šanda, and S. Mukamel, “Coherent multidimensional optical spectroscopy of excitons in molecular aggregates; quasiparticle versus supermolecule perspectives,” *Chem. Rev.* **109**, 2350-2408 (2009).
- [91] M. H. Brooker, G. Hancock, B. C. Rice, and J. Shapter, “Raman frequency and intensity studies of liquid H₂O, H₂¹⁸O and D₂O,” *J. Raman Spectrosc.* **20**, 683-694 (1989).
- [92] D. S. Pestov, “Detection of bacterial endospores by means of ultrafast coherent Raman spectroscopy,” Ph.D. dissertation (Texas A&M University, 2008).
- [93] A. E. Siegman, *Lasers* (University Science, Mill Valley, CA, 1986).

VITA

Name: Xi Wang

Address: Department of Physics and Astronomy, MS 4242
Texas A&M University, College Station, TX 77843-4242

Email Address: xwangphy@gmail.com

Education: Ph.D., Physics, Texas A&M University, May 2011
M.S., Physics, Peking University, China, July 2004
B.S., Physics, Nanjing University, China, July 2001

Publications:

- **X. Wang**, A. Zhang, M. Zhi, A. V. Sokolov, G. R. Welch, and M. O. Scully, *Opt. Lett.* **35**, 721-723 (2010).
- **X. Wang**, A. Zhang, M. Zhi, A. V. Sokolov, and G. R. Welch, *Phys. Rev. A* **81**, 013813 (2010).
- L. Yuan, G. O. Ariunbold, R. K. Murawski, D. Pestov, **X. Wang**, A. K. Patnaik, V. A. Sautenkov, A. V. Sokolov, Y. V. Rostovtsev, and M. O. Scully, *Phys. Rev. A* **81**, 053405 (2010).
- M. Zhi, **X. Wang**, and A. V. Sokolov, *J. Mod. Opt.* **57**, 1863-1866 (2010).
- M. Zhi, **X. Wang**, and A. V. Sokolov, *Opt. Express* **16**, 12139-12147 (2008).
- D. Pestov, **X. Wang**, R. K. Murawski, G. O. Ariunbold, V. A. Sautenkov, and A. V. Sokolov, *J. Opt. Soc. Am. B* **25**, 768-772 (2008).
- D. Pestov, **X. Wang**, G. O. Ariunbold, R. K. Murawski, V. A. Sautenkov, A. Dogariu, A. V. Sokolov, and M. O. Scully, *Proc. Natl. Acad. Sci.* **105**, 422-427 (2007).
- D. Pestov, G. O. Ariunbold, **X. Wang**, R. K. Murawski, V. A. Sautenkov, A. V. Sokolov, and M. O. Scully, *Opt. Letters* **32**, 1725-1727 (2007). [selected for the August 2007 issue of *Virt. J. Ultrafast Science*]
- M. Zhi, D. Pestov, **X. Wang**, R. K. Murawski, Y. V. Rostovtsev, Z.-E. Sariaynni, V. A. Sautenkov, N. G. Kalugin, and A. V. Sokolov, *J. Opt. Soc. Am. B* **24**, 1181-1186 (2007). [selected for May 1, 2007 issue of *Virt. J. Biological Physics Research*]
- D. Pestov, R. K. Murawski, G. O. Ariunbold, **X. Wang**, M. Zhi, A. V. Sokolov, V. A. Sautenkov, Y. V. Rostovtsev, A. Dogariu, Y. Huang, and M. O. Scully, *Science* **316**, 265-268 (2007). [highlighted in *Photonics Spectra*, p. 22 (June 2007)]
- G. I. Petrov, R. Arora, V. V. Yakovlev, **X. Wang**, A. V. Sokolov, and M. O. Scully, *Proc. Natl. Acad. Sci.* **104**, 7776-7779 (2007).

Professional Achievements/Honors/Affiliations:

- Ethel Ashworth-Tsutsui Memorial Awards in Research (2010)
- DAMOP Travel Award (2010)
- TSAPS Travel Award (2009)
- ASSP Travel Grant (2009)
- AUF Fellowship (2004-2005)
- Founding member of the Texas A&M University student chapter of OSA